UNIVERSITY OF CALIFORNIA SAN DIEGO

Observations of ocean transport and mixing across scales in the subpolar North Atlantic and Greenland

A dissertation submitted in partial satisfaction of the
requirements for the degree Doctor of Philosophy

in

Oceanography

by

Monica Nelson

Committee in charge:

Fiammetta Straneo, Co-Chair
Sarah Purkey, Co-Chair
Fonna Forman
Amy Waterhouse

2025

The Dissertation of Monica Nelson is approved, and it is acceptable in quality and form for publication on microfilm and electronically.

University of California San Diego

2025

DEDICATION

I dedicate this to my grandparents, Jean and Mike Nelson, who loved learning, dogs, and mountains; who taught our family to love the same; and who provided financial support for me to pursue my education. No descendants of theirs have yet to escape the allure of higher education - for better or for worse.

EPIGRAPH

The birds have vanished down the sky.
Now the last cloud drains away.
We sit together, the mountain and me,
until only the mountain remains.

Li Bai

TABLE OF CONTENTS

LIST OF FIGURES

LIST OF TABLES

ACKNOWLEDGEMENTS

First and foremost, thank you to my co-advisors, Fiamma Straneo and Sarah Purkey, who were so patient and helpful as I bumbled my way through this PhD process. Thank you for the countless meetings, listening to me babble about the analysis I was trying to do and making sense of it with me. Thank you for the writing support, earning us compliments on our paper that wouldn't have been received without your constructive comments and edits. Thank you for receiving me as a whole person and giving me space to navigate the climate crisis, COVID-19 pandemic, UAW strikes, and federal government attacks on science and education. So many external factors rocked the boat of my time getting my PhD and you rode out the waves with me. Thank you to Fiamma, for the incredible fieldwork opportunities. Before coming to Scripps I was infatuated with Antarctica and had barely thought about Greenland. Thank you for trusting me to do fieldwork with you in this incredible corner of the world - I am so, so grateful. Thank you Sarah, for patiently seeing me through this PhD on the North Atlantic, with the promise that I'd one day shift to studying the Southern Ocean. Apologies I didn't make it happen during my PhD; "the other pole" is up next!

Thanks to my Straneo lab-mates who have made PhD life all the more enjoyable over the years. Special thanks to Margaret Lindeman, Bobby Sanchez, Aurora Roth, Kylie Kinne, Marta Faulkner, Ken Zhao and Tiago Biló for the science lessons, laughs, and sanity checks. Thank you to Fiamma Straneo for bringing such a wonderful group of scientists together to make the magic happen and thanks to Jamie Holte for keeping the lab on two sturdy feet and keeping us well-fed with delicious baked goods. The splitting of our lab between San Diego and Boston has made me treasure our time together all the more, but I wish we were still all in the same place!

Thanks to my COAP cohort who helped me through first year classes and become fast friends. In particular, Hayden Johnson, Matt Kehrli, Matt Luongo, Devon Northcott, and Ryan Saenger. Thanks to all the SIO folks who had lunch on the MESOM balcony with me, got me out surfing, went on swims around the pier with me, went on long bike rides with me, and tromped about in the mountains with me. I needed all of that to get this PhD done.

Thank you to Susheel Adusumilli, who stood in as a mentor when I needed one, helped me through the anxiety of submitting my first paper, brought me joy and pastries, and got me doing cartwheels during compass calibrations.

Many, many thanks to my fellow climate action advocates in the UCSD Green New Deal and UC Green New Deal Coalition. I continue to be amazed by what we accomplished together and am so grateful for the community of organizers who provided space for me to do something tangible when PhD research felt slow and esoteric.

Thank you to Inga Smith, who believed in me as an undergraduate student and set me on track to coming to Scripps Institution of Oceanography. Without your encouragement, your incredible support writing and publishing my first oceanography paper, and your contacts at Scripps, I never would've made it here and had the incredible opportunities I've had.

Finally, thank you to my co-authors Fiamma Straneo, Sarah Purkey, Marieke Femke de Jong, Amy Waterhouse, Kristen Fogaren and Daniel Torres for your contributions to my work, without which I wouldn't have gotten any of my papers over the line.

Chapter 1, in full, is a reprint of the material as it appears in Geophysical Research Letter, 2024. DOI: 10.1029/2023GL106501. Nelson, M, Straneo, F, Purkey, S, de Jong. The dissertation author was the primary investigator and author of this paper.

Chapter 2, excluding the box-budget in the appendix, is a reprint of the material as it appears in the Journal of Geophysical Research: Oceans, 2025. DOI: 10.1029/2024JC022246. Nelson, M, Straneo, F, Purkey, S, Waterhouse, A, Fogaren, K, Torres D. The dissertation author was the primary investigator and author of this material.

Chapter 3 is currently in preparation to be submitted for publication by Nelson, M, Straneo, F, and Purkey, S. The dissertation author was the primary investigator and author of this paper.

VITA

2017	Bachelor of Science, University of Otago
2020	Master of Science, University of California San Diego
2025	Doctor of Philosophy, University of California San Diego

PUBLICATIONS

Nelson, M., Queste, B., Smith, I., Leonard, G., Webber, B., Hughes, K. 2017. Measurements of Ice Shelf Water beneath the front of the Ross Ice Shelf using gliders. Journal, 58(74): 41-50. doi:10.1017/aog.2017.34

Nelson, M., Straneo, F., Purkey, S., de Jong, M. F. 2024. Delayed Recovery of the Irminger Interior From Cooling in 2015 Due To Widespread Buoyancy Loss and Suppressed Restratification. Geophysical Research Letters, 51. doi.org/10.1029/2023GL106501

Lindeman, M., Straneo, F., Adams, H., **Nelson, M.**, Schartup, A. 2024. Low mercury concentrations in a Greenland glacial fjord attributed to oceanic sources. Communications Earth & Environment 5, 320. doi.org/10.1038/s43247-024-01474-9

Nelson, M., Gere, C., Cooper, A., Thackray, V., Aron, A. 2025. The Wins of the Grassroots Climate Movement in the University of California. Frontiers in Education. 10:1491439. doi:10.3389/feduc.2025.1491439

Nelson, M., Straneo, F., Purkey, S. G., Waterhouse, A. F., Fogaren, K. E., Torres, D. J. (2025). Observations of water mass modification and cross-shelf exchange at Narsaq Trough, Greenland. Journal of Geophysical Research: Oceans, 130, e2024JC022246. https://doi.org/10.1029/2024JC022246

ABSTRACT OF THE DISSERTATION

Observations of ocean transport and mixing across scales in the subpolar North Atlantic and Greenland

by

Monica Nelson

Doctor of Philosophy in Oceanography

University of California San Diego, 2025

Fiammetta Straneo, Co-Chair
Sarah Purkey, Co-Chair

Ocean dynamics in the subpolar North Atlantic play an important role in the global climate system: Deep convection in the open ocean drives a large-scale overturning circulation that redistributes heat around the globe and cold currents circulating around Greenland protect marine-terminating glaciers from warmer water offshore that drives ice-melt and sea level rise. However, the drivers of natural variability within this complex system, and how the region will respond to anthropogenic forcing, are not fully understood. This thesis sheds light on two regions of the subpolar North Atlantic: the Irminger Sea and the Greenland continental shelf, where the mesoscale dynamics that deliver heat to these otherwise cold regions are studied.

The Irminger Sea is a region of deep convection, contributing to the water mass transformation and large-scale circulation. In Chapter 1, observations from profiling Argo floats and repeat hydrography are used to track buoyancy changes in the Irminger interior and study the region's recovery from wintertime convection. This work shows that the slow recovery of the Irminger interior after a year of particularly strong deep convection can be attributed to reduced transport of warm, buoyant eddies from the Irminger Current.

On Greenland's continental shelf, cold, fresh waters insulate the Greenland Ice Sheet. Here, cross-shelf exchange that delivers heat on-shelf is studied. In Chapter 2, observations from a two-week ship-based survey of Narsaq Trough are used to investigate how troughs (glacially carved depressions in the continental shelf) modify the local continental shelf environment. This snapshot suggests that the trough drives a subsurface exchange flow that produces mid-depth waters in the trough that are a mixture of on-shelf and off-shelf waters. Chapter 3 contextualises the findings from Chapter 2 with two decades of repeat observations over Narsaq Trough by voluntary observing ships. This extensive time-series shows a bathymetrically-steered exchange flow is a persistent feature at the trough, both above and below the shelf, driving cross-shelf exchange of heat and salt.

Cumulatively, the studies described here show how eddies and bathymetrically-steered flows at the boundaries of the sub-polar North Atlantic basins supply heat to regions which are unreachable by large-scale ocean processes.

Introduction

The subpolar North Atlantic is a region of climatic importance due to its role in transforming water masses and driving large-scale ocean circulation that regulates global temperature, as well as containing meters of sea level rise potential stored in the Greenland Ice Sheet (Broecker, 1987; Lozier, 2010; J. L. Bamber, Westaway, Marzeion, & Wouters, 2018; Vaughan et al., 2013). Broadly speaking, in the upper ocean, there are two water main masses of note: warm, salty Atlantic Water (AW), of subtropical Atlantic origin; and cold, fresh Polar Water (PW), of Arctic origin. AW comes from the south and is transported around the subpolar North Atlantic by the North Atlantic and Irminger Currents, following the bathymetric boundaries of the deep ocean basins (Figure I.1, red-to-yellow arrows). Whereas PW comes from the north and flows clock-wise around Greenland's coast then southward along Canada's Labrador coast in a system of currents (Figure I.1, blue arrows). This thesis tracks the mechanisms by which AW delivers heat to the regions not reached by the main advective pathways of the warm currents, namely through eddies and bathymetric steering.

During the transit of AW and PW around the subpolar North Atlantic, some water is shed from the fast flowing currents into the Labrador and Irminger Sea basins (i.e. the interior of the subpolar gyre) where cold wintertime air temperatures and strong winds drive heat loss from the ocean to the atmosphere (Gelderloos, Katsman, & Drijfhout, 2011; Katsman, Spall, & Pickart, 2004; Knutsen, Svendsen, Østerhus, Rossby, & Hansen, 2005; Le Bras et al., 2022; Spall, 2004; Straneo, 2006b). This heat loss results in reduced buoyancy (i.e. increased density) of the surface waters, causing them to sink, mixing with waters below (Straneo, 2006a). Over the course of a winter season this heat and buoyancy loss can act to mix the water column down to over 1000

m in a process known as deep convection (Pickart, Spall, Ribergaard, Moore, & Milliff, 2003). The conversion of warm, light waters from the sub-tropical Atlantic into cold, dense waters is known as water mass transformation and forms the link between the upper and lower limbs of the Atlantic Meridional Overturning Circulation (AMOC; Broecker, 1987; Lozier, 2010). The upper limb being the northward flowing North Atlantic Current at the surface, and the lower limb being the newly formed deep water that slowly flows south. Critically, this large-scale overturning circulation transports excess heat from the tropics northwards to the high latitudes and transports cool waters south; helping to balance the imbalance in solar radiation incident on the Earth's surface (Broecker, 1991; Trenberth & Caron, 2001).

The subpolar North Atlantic is expected to experience significant changes as the planet warms due to anthropogenic climate change. In addition to global ocean warming, the region is expected to freshen due to increased meltwater export from the Arctic and Greenland (J. Bamber, van den Broeke, Ettema, Lenaerts, & Rignot, 2012; Dukhovskoy et al., 2016). Surface freshening and warming will lead to increased stratification, inhibiting wintertime convection, and possibly causing in a slowdown of the AMOC (Bakker et al., 2016; Böning, Behrens, Biastoch, Getzlaff, & Bamber, 2016; Frajka-Williams, Bamber, & Våge, 2016; Keil et al., 2020; Le Bras, Straneo, Holte, de Jong, & Holliday, 2020). The AMOC transports heat northward such that an AMOC slowdown may result in increased cold spells in the United States (Yin & Zhao, 2021) and increased summer heat waves in Europe (Mecking, Drijfhout, Hirschi, & Blaker, 2019). Given the role the region plays in regulating climate and the changes it is expected to undergo, there is interest in better understanding the dynamics governing the subpolar North Atlantic (Swingedouw et al., 2022).

Beyond the physical processes in the subpolar North Atlantic, the region is also important in terms of ocean biogeochemistry. Currently, the ocean absorbs $\sim$30% of the excess carbon that is accumulating in the atmosphere, sheltering us from a more rapid accumulation of greenhouse gases, leading to less atmospheric warming (Gruber et al., 2019; Sabine, 2004). The subpolar North Atlantic is particularly effective at taking up carbon and oxygen from the atmosphere

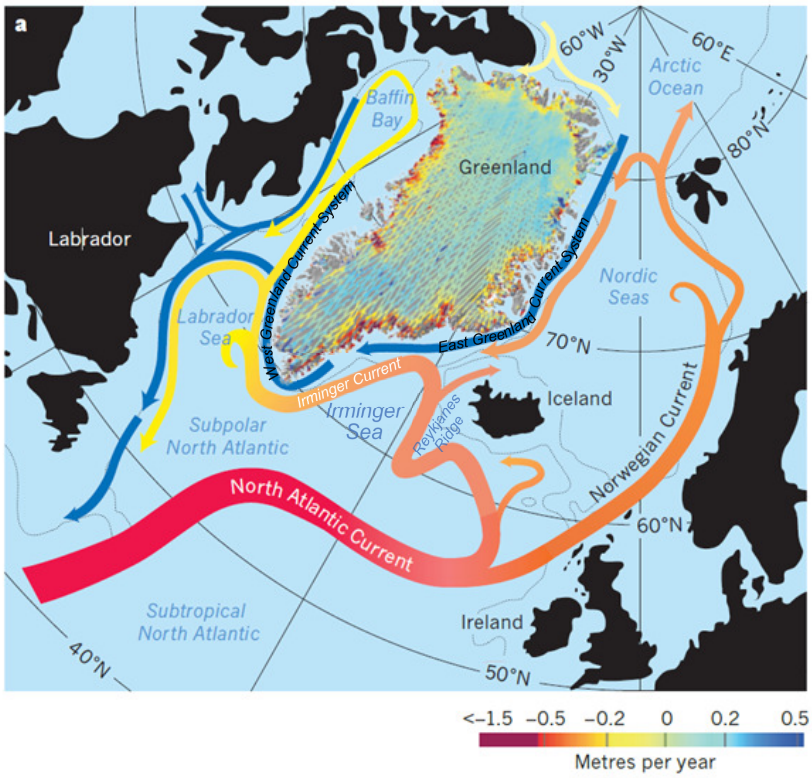

Figure I.1. Schematic of the subpolar North Atlantic showing the pathways of the major surface currents around Greenland with colors indicating origin. Atlantic Waters (AW) are shown in red to yellow; Polar Waters (PW) are shown in blue. The dynamic thinning of the Greenland Ice Sheet is overlain. Adapted from Straneo and Heimbach (2013), Figure 3a.

as these gases are more soluble in colder, fresher water (Sabine, 2004; Landschützer, Gruber, Bakker, & Schuster, 2014; Takahashi et al., 2014). Further, when waters in the subpolar North Atlantic convect and undergo water mass transformation, carbon- and oxygen-rich waters are exported to depth (Palevsky & Nicholson, 2018; Fröb et al., 2016). For carbon, this is a means of sequestering carbon for 100s to 1000s of years. For oxygen, this replenishes the deep oxygen reservoir to support subsurface ecosystems. In addition, deep convection mixes nutrient-rich waters at depth up to the surface, where waters are depleted in nutrients, enabling increased primary productivity (Tesdal, Ducklow, Goes, & Yashayaev, 2022).

The climatically important open ocean dynamics and biogeochemical processes in the subpolar North Atlantic are influenced by exchange of properties at the margins of the ocean

basins (Spall, 2004; Straneo, 2006b; Le Bras et al., 2022; Fried, 2024). Of particular interest in this thesis is exchange between the Imringer Sea and Reykjanes Ridge (the portion of the mid-Atlantic ridge that extends south of Iceland; Figure I.1) and exchange across the continental shelf around the coast of Greenland.

The Irminger Sea, bounded by Greenland to the west and the Reykjanes Ridge to the east (Figure I.1), is a region of wintertime deep convection, water mass transformation, and overturning (de Jong, Oltmanns, Karstensen, & de Steur, 2018; Fu, Lozier, Majumder, & Petit, 2024; Pickart et al., 2003). While the restratification dynamics following deep convection are well-studied in the Labrador Sea, there has been little focus on these dynamics in the Irminger Sea, on the other side of Greenland, until recently. Extending findings from the Labrador Sea to the Irminger Sea, it is assumed that a portion of the AW traveling northwards in the Irminger Current along the Reykjanes Ridge is shed from the current through eddies and enters the Irminger Sea interior, replacing the outflowing, recently formed dense water (Sterl & de Jong, 2022; Gelderloos et al., 2011; Katsman et al., 2004; Straneo, 2006b). This input of AW thus restratifies the water column, setting the sea up for another season of wintertime convection. In Chapter 1, I assess whether the Irminger Sea in fact follows these dynamics. Using observations from ship-based surveys and profiling floats I analyse the slow restratification of the Irminger Sea after a season of especially strong convection and buoyancy loss in 2015. As suspected, the restratification of the interior is found to be driven by exchange with the currents circulating around the boundary. Specifically, the delayed recovery from strong convection in 2015 is attributed to a reduction in transport of AW from the Irminger Current into the Irminger interior by eddies generated through baroclinic instability.

At the edge of the Greenland continental shelf warm, salty AW abuts cold, fresh PW (Figure I.1). Cross-shelf exchange occurs around the margin of Greenland that results in the mixing of AW and PW, export of PW offshore (Duyck & De Jong, 2021; Duyck, Gelderloos, & de Jong, 2022; Pacini et al., 2021), and import of AW onshore (Le Bras et al., 2022; Snow et al., 2021, 2023). The export of fresh PW offshore affects vertical stratification in the convective

basins of the subpolar North Atlantic and is projected to contribute to the slowdown of the AMOC in a warming climate (Schiller-Weiss, Martin, & Schwarzkopf, 2024; Rahmstorf et al., 2015; Swingedouw et al., 2022; Bakker et al., 2016). Meanwhile, the import of AW onshore drives submarine melting of marine-terminating glaciers in the fjords that riddle Greenland's coastline (Straneo & Heimbach, 2013; Sutherland et al., 2013; Slater & Straneo, 2022).

While exchange across Greenland's continental shelf due to wind-forcing and eddies has been moderately well studied, the affects of bathymetry are relatively understudied. In particular, the degree to which troughs (deep grooves that cut across the continental shelf from the mouths of fjords to the shelf-break) drive cross-shelf exchange has only been the focus of a handful of studies (e.g. Sutherland & Cenedese, 2009; Snow et al., 2023). In Chapter 2 and 3 I address this knowledge gap. In Chapter 2, I present a process study of a trough in southwest Greenland using data from a 2 week hydrographic survey. The trough is shown to divert the surface flow around the trough and drive an exchange flow in the subsurface layer within the trough. Further, a unique mixture of AW and PW is found inside the trough, indicative of cross-shelf exchange of AW and PW. In Chapter 3, I contextualise the findings from the 2 week survey using two decades of observations from voluntary observing ships that regularly transit over the trough. The long time-series shows that the trough drives a persistent cross-shelf exchange both above and below the continental shelf, indicating that some of the observations during the 2 week survey were anomalous conditions.

Chapter 1

Delayed recovery of the Irminger interior from cooling in 2015 due to widespread buoyancy loss and suppressed restratification

Abstract

Watermass transformation in the Irminger Sea, a key region for the Atlantic Meridional Overturning Circulation, is influenced by atmospheric and oceanic variability. Strong wintertime atmospheric forcing in 2015 resulted in enhanced convection and the densification of the Irminger Sea. Deep convection persisted until 2018, even though winters following 2015 were mild. We show that this behavior can be attributed to an initially slow convergence of buoyancy, followed by more rapid convergence of buoyancy. This two-stage recovery, in turn, is consistent with restratification driven by baroclinic instability of the Irminger Current, that flows around the basin. The initial, slow restratification resulted from the weak horizontal density gradients, resulting from the widespread 2015 atmospheric heat loss. Faster restratification occurred once the Irminger Current recovered. This mechanism explains the delayed recovery of the Irminger Sea following a single extreme winter and has implications for the ventilation and overturning that occurs in the basin.

1.1 Introduction

The Irminger Sea plays a key role in climate due to the unique local ocean-atmosphere conditions that allow for deep convection and water mass transformation, feeding the Atlantic Meridional Overturning Circulation (AMOC) and ventilating the deep ocean (Pickart et al., 2003; de Jong, van Aken, Våge, & Pickart, 2012; Katsman, Drijfhout, Dijkstra, & Spall, 2018; Le Bras et al., 2020). The rate of intermediate water formation regulates AMOC strength and oxygen and carbon dioxide concentrations at intermediate depths (Petit, Lozier, Josey, & Cunningham, 2020; Palevsky & Nicholson, 2018). As such, variability in local stratification, which affects intermediate water formation, is of interest for understanding global climate (Lozier et al., 2019; Chafik, Holliday, Bacon, & Rossby, 2022; Takahashi et al., 2009; Pérez et al., 2013; Rhein, Steinfeldt, Kieke, Stendardo, & Yashayaev, 2017; Tjiputra et al., 2018).

In 2015, strong winter atmospheric forcing resulted in anomalously deep mixed layer

depths ($>$ 1400 m) and the expansion of the intermediate water layer and thinning of the light water layer within the Irminger Sea (de Jong & de Steur, 2016; de Jong et al., 2018). While 2015 was the first year of deep convection in the region since the early 1990s (Våge et al., 2011), deep convection persisted to depths of $>$ 1300 m through 2018, despite a return to normal atmospheric forcing (Zunino, Mercier, & Thierry, 2020; Fox et al., 2022). The persistence of relatively deep convection in the Irminger Sea, even under moderate atmospheric forcing, is indicative of a slow recovery of the Irminger Sea to pre-2015 conditions. Because of this slow recovery, the injection of oxygen and carbon to intermediate depths likely persisted with potential implications for carbon sequestration (Fröb et al., 2016).

The recovery of the Irminger Sea is dictated by the restratification processes which converge warm, buoyant water on the interior, thickening the light water layer. Models and observations show that restratifying waters are advected from the boundary currents by eddies (Spall, 2004; Katsman et al., 2004; Straneo, 2006a, 2006b; Gelderloos et al., 2011; Fan, Send, Testor, Karstensen, & Lherminier, 2013; Sterl & de Jong, 2022). In the Labrador Sea, these eddies are known to be produced by baroclinic instabilities in the boundary current (Visbeck, Marshall, & Jones, 1996; Spall, 2004; Straneo, 2006a; de Jong, Bower, & Furey, 2016). In the Irminger Sea, Sterl and de Jong (2022) show that interannual variations in the seasonal restratification are strongly correlated with eddy kinetic energy (EKE) but do not explain what drives EKE variability.

The anomalous densification of the Irminger Sea in 2015 provided a unique opportunity to study restratification processes in the basin. We use repeat hydrography, an Argo product, and EKE from a satellite product to observe changes in both the Irminger interior and Irminger Current (IC) and investigate the dynamics that converge buoyancy on the interior. We show that while the 2015 wintertime buoyancy loss affected both the interior and the IC, the IC regains buoyancy much more quickly than the interior. The slow timescale for the recovery of the interior is primarily set by the time needed for the development of a large horizontal buoyancy gradient between the interior and IC. We show that the multi-year recovery processes and timescales in

the Irminger Sea are a consistent extension of the seasonal restratification dynamics that have been described in the Labrador Sea.

1.2 Data

Conductivity, Temperature, Depth (CTD) profiles collected along repeat occupations of the AR07-E hydrographic section (Figure 1.1a, bold black line) are used to observe full-depth changes in basin-wide potential density structure over the study period (Figure 1.1b-1.1d). Eight occupations between 2010-2022 are used: biennial occupations between 2010 and 2018 by the Observatoire de la variabilité interannuelle et décennale en Atlantique Nord (OVIDE) project, and occupations in 2015, 2020 and 2022 by the Overturning in the Subpolar North Atlantic Program (OSNAP). All sections were conducted in either June or July, except the 2014 section which was conducted in May and the 2022 section which was conducted in August. No additional data quality control was carried out.

Temperature and salinity from the Roemmich and Gilson Argo gridded climatology and anomalies (RG product) from January 2011 to December 2022 within the Irminger Sea are used to estimate the temporal variability in horizontal and vertical density structure. The RG product uses only adjusted, delay mode quality controlled Argo profiles with additional screening to exclude any floats with salinity drift to give monthly objective maps of temperature and salinity on 58 pressure levels between 0 and 2000 dbar on a 1°x1° grid (Roemmich & Gilson, 2009).

Eddy activity is quantified using the AVISO Eddy Kinetic Energy (EKE) product (AVISO+Altimetry, 2021). The product is derived from satellite altimetry and has a spatial resolution of $1/4°$ on a monthly time-step.

1.3 Methods

The study period, January 2011 to December 2022, is split into three periods: pre-strong convection (Jan 2011 to Mar 2015), during strong convection (Apr 2015 to Mar 2018), and

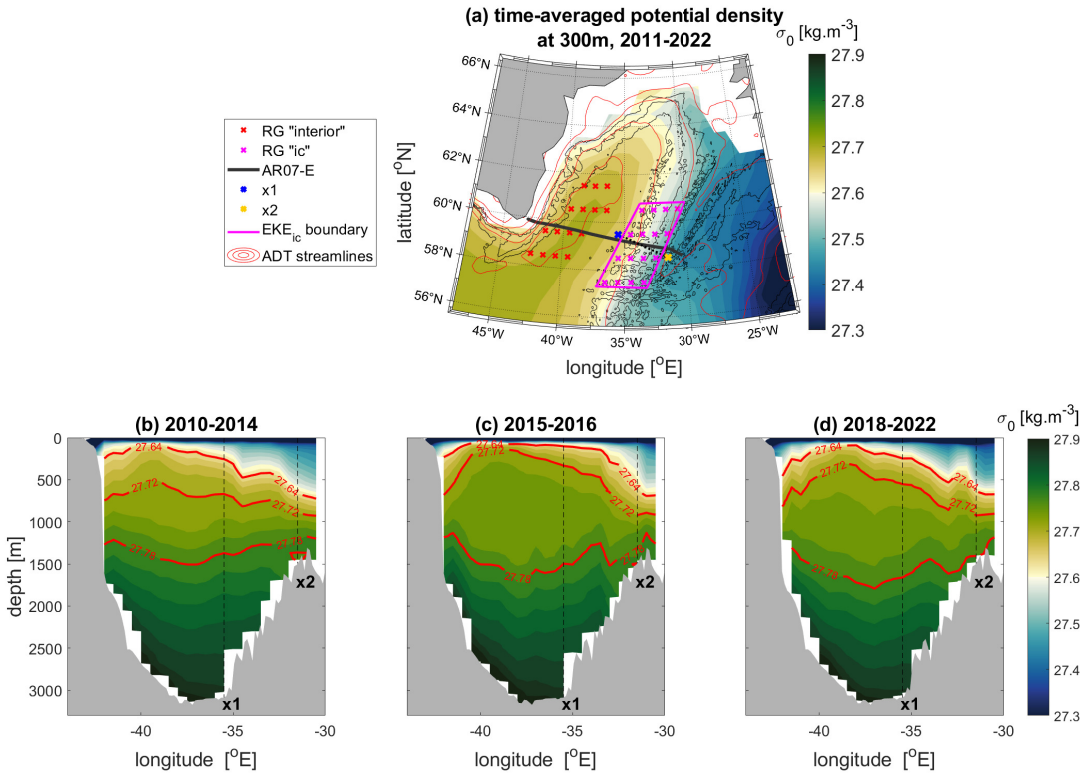

Figure 1.1. (a) Potential density at 300 m in the Irminger Sea with 1500 m, 2000 m, and 2500 m isobaths (thin black lines) and Absolute Dynamic Topography streamlines (red) overlain to illustrate the mean circulation. Locations of data used in this paper are also shown: RG grid-points used in the interior area average (red crosses); RG grid-points used in the IC area average (magenta crosses); AR07-E hydrographic section (bold black line); x1 (blue cross) and x2 (yellow cross) between which ΔB_x is calculated; and the region over which the area-averaged EKE$_{ic}$ is calculated (magenta box). Mean potential density AR07-E hydrographic sections across the Irminger Sea averaged over the (b) pre-strong convection period, (2010, 2012, 2014); (c) during strong convection period (2015 and 2016); and (d) post-strong convection period (2018, 2020 and 2022), with the 27.64, 27.72, and 27.78 kg.m^{-3} isopycnals (red) and the locations of x1 and x2 for the ΔB_x calculation (black dashed) overlain.

post-strong convection (Apr 2018 to Dec 2022). Temperature and salinity profiles from each AR07-E occupation are interpolated onto a regular 2D grid and averaged over each period to create composite summertime potential density sections across the Irminger Sea (Figure 1.1b-1.1d).

Within the Irminger Sea the study focuses on two regions: the interior and the IC on the eastern boundary (Figure 1.1a, red and magenta crosses respectively). While exchange of waters

is also known to occur on the western boundary, through eddies (Fan et al., 2013; Le Bras et al., 2020) and slantwise convection (Le Bras et al., 2022), the western boundary is notably less buoyant than the eastern boundary (Figure 1.1; Våge et al., 2011) with less available potential energy for the development of baroclinic instabilities (Pedlosky, 1979). As such, it is expected that exchange with the eastern boundary dominates the convergence of buoyant water on the interior. This is consistent with idealised and observational studies in both the Labrador and Irminger Seas (Spall, 2004; Straneo, 2006b; Våge et al., 2011; Sterl & de Jong, 2022) with Fan et al. (2013) showing that the most buoyant eddies found in the Irminger interior are from the eastern boundary. Thus, we create spatially-averaged time-series of potential density for only the interior and IC on the eastern boundary using the RG product (Figure 1.2a and 1.2b). Potential density referenced to the surface is calculated at each grid-point then an area-averaged potential density profile is calculated for the interior and IC.

Similarly, a time-series of the depth-integrated buoyancy content in the 100-1000 m layer is calculated for the interior and IC using the RG product (Figure 1.2c). First, area-averaged in situ density profiles are calculated for the interior and the IC as above. Second, the buoyancy content within the interior, B_{int}, and IC, B_{ic}, is calculated as

$$B = -g \int_{-1000}^{-100} \left(\frac{\rho(z) - \rho_0}{\rho_0} \right) \, dz \tag{1.1}$$

where $\rho(z)$ is the average in situ density profile in each region, ρ_0 is defined to be 1037 kg m^{-3} representing the densest water in the upper 2000 m, and g is the gravitational constant.

The rates of recovery of the interior and IC are defined as the rate at which buoyancy is gained in each region. The rates are estimated by using a Least Squares fit of a linear trend with a seasonal cycle to the time-series of B_{int} and B_{ic}:

$$\hat{B} = a + mt + c\sin(\omega t) + d\cos(\omega t) \tag{1.2}$$

where coefficients, a, m, c, and d are optimized for the fit. m is the linear trend, c and d determine the amplitude of the seasonal cycle, and ω is the period of the seasonal cycle (Wunsch, 1996).

The seasonal restratification of the interior is quantified by the buoyancy gained in the interior over the restratification period. The restratification period is defined as the time from minimum B_{int} to maximum B_{int} each year such that the buoyancy gain during restratification is $B_{int}^{gain} = \max(B_{int}) - \min(B_{int})$ (Figure 1.3b and 1.3c).

Lastly, the horizontal density gradient across the IC is approximated by differencing the buoyancy content between an inner point (x1) and an outer point (x2) of the IC (Figure 1.1a) using Eq. (1.1) at each time step, $\Delta B_x = B_{x2} - B_{x1}$ (Figure 1.3a). Following Spall (2004) and Straneo (2006a), we square ΔB_x at the start of the restratification period each year (Figure 1.3b). ΔB_x^2 is used as the horizontal buoyancy difference sets both the number of eddies and the additional buoyancy content the eddies can transport to the interior (Spall, 2004). Additionally, EKE is quantified by spatially averaging all AVISO grid-points in the IC region (EKE_{ic}, Figure 1.1a) and taking the time-mean over the restratification period each year (EKE_R, Figure 1.3c). We then calculate linear correlations between ΔB_x^2 and B_{int}^{gain} (r_{Bx}) and EKE_R and B_{int}^{gain} (r_{eke}), as in Straneo (2006a) and Sterl and de Jong (2022) respectively.

See Appendices 1.A for a more detailed description of these methods.

1.4 Results

The anomalous water mass transformation that occurred in 2015 notably changed the density structure of the whole Irminger Sea (Figure 1.1b-1.1d). Following the 2014/2015 winter there is thinning of the light water layer (27.64-27.72 kg.m^{-3}) and a thickening of intermediate water layer (27.72-27.78 kg.m^{-3}) across the Irminger interior, consistent with de Jong and de Steur (2016) and de Jong et al. (2018). Thickening of the intermediate water layer is also seen on both the eastern (between x1 and x2) and western (between -44 °E and -42 °E) boundaries, resulting in a steepening of the horizontal density gradients (Figure 1.1c). Between 1000-1500 m,

in the interior isopycnals deepen due to the convergence of anomalously fresh intermediate water recirculating from the Labrador Sea (Zunino et al., 2020; Fox et al., 2022); whereas there is little change at depth on the boundaries. In the post-strong convection period the density structure is returning to the pre-strong convection state, with a deepening of the 27.64 and 27.72 kg.m^{-3} isopycnals in the interior and a flattening of the isopycnal slope across the boundaries (Figure 1.1d).

As discussed in Section 2.3 we now focus on the interior and the IC on the eastern boundary and find that the two regions recover from the density anomaly differently (Figure 1.2, Table 1.1). In the interior, the density anomaly persists from 2015 through 2018, after which isopycnals above 1000 m begin to deepen (Figure 1.2a). This is reflected in the slow rate of buoyancy gain in the interior in the first three years after 2015, followed by more rapid gain in subsequent five years (Figure 1.2c, red). In contrast, in the IC, the density anomaly is quickly exported, with the 27.64 kg.m^{-3} isopycnal deepening rapidly in 2015 and 2016, then stabilising after 2018 (Figure 1.2b). This is seen in the rapid gain of buoyancy in the IC in the first three years after 2015, followed by slower gain in the subsequent five years (Figure 1.2c, pink). Estimates of the rates of recovery for the interior and IC are shown in Table 1.1.

Table 1.1. Rates of recovery in the Irminger interior compared to those in the Irminger Current for the during-strong convection period (Apr 2015 - Mar 2018) and the post-strong convection period (Apr 2018 - Dec 2022).

	Recovery rate 2015-2018 ($\times 10^{-3}$ m^2 s^{-2} mo^{-1})	Recovery rate 2018-2022 ($\times 10^{-3}$ m^2 s^{-2} mo^{-1})	Percent recovered by Mar 2018 (3 years)	Percent recovered by Dec 2022 (8 years)
Irminger interior	0.9 ± 0.5	2.7 ± 0.6	12 %	79 %
Irminger Current	9.3 ± 1.0	2.2 ± 0.3	70 %	94 %

The difference in the evolution of the buoyancy content in the interior and the IC results in a change in the horizontal buoyancy gradient across the IC, ΔB_x (Figure 1.3a). Before the onset of strong convection ΔB_x oscillates around 1 m^2 s^{-2}. In 2015 there is little change in the mean of ΔB_x as both the buoyancy content on the inner and outer edge of the IC decrease similarly. However, from 2016 to 2018, there is a steady increase in ΔB_x due to the more rapid

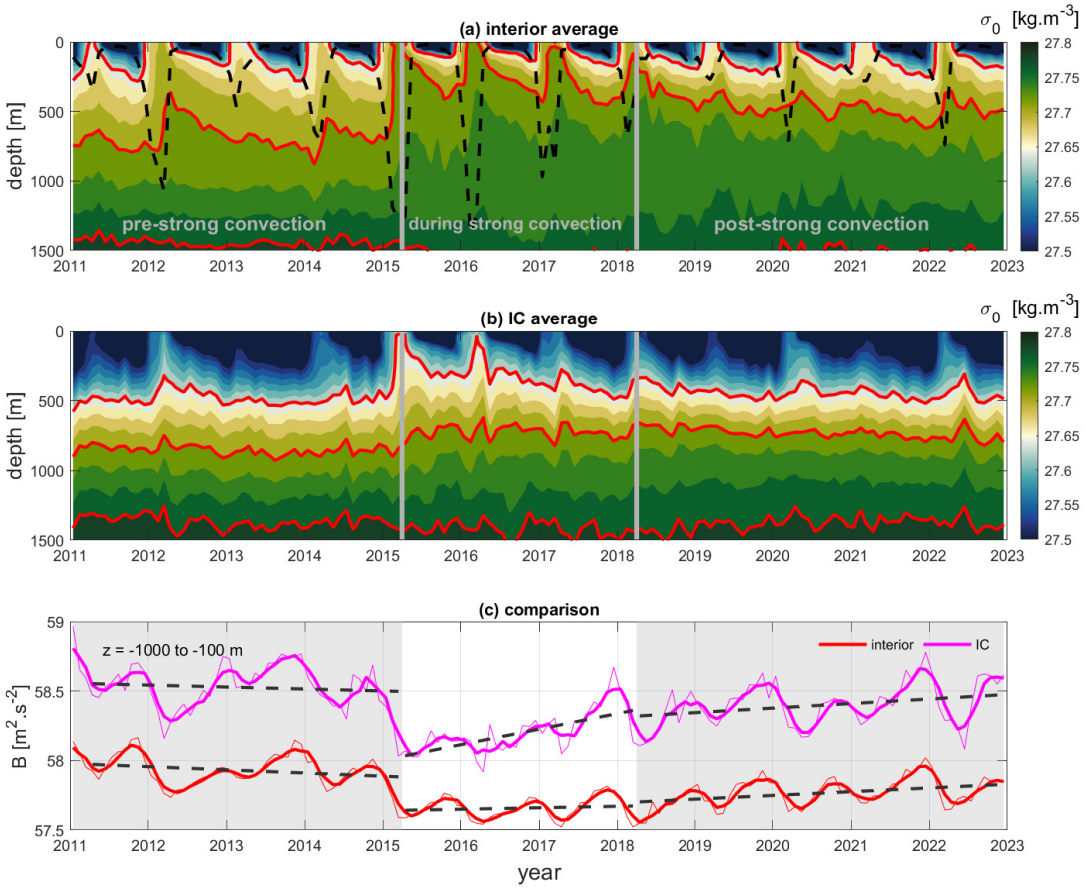

Figure 1.2. Time-series of the area-averaged potential density in the (a) interior and (b) IC (see Figure 1.1a for locations), in the upper 1500 m with the 27.64, 27.72, and 27.78 kg.m^{-3} isopycnals overlain (red). The mixed layer depth (black dashed) is shown in (a). (c) Depth-integrated buoyancy content over the 100-1000 m layer for the interior (red) and IC (pink); thin lines show the raw monthly time-series, thick lines show the smoothed time-series after applying a 4-month moving mean. Thick black dashed line shows linear trend from Least Squares fit for each period.

increase in buoyancy on the outer edge of the IC (at x2) than on the inner edge (at x1). In the years after 2018 ΔB_x appears to decrease slightly, consistent with eddy flux from the IC to the interior working to flatten the isopycnal gradient.

Lastly, the buoyancy gain during restratification is compared to the horizontal buoyancy gradient and the EKE. Changes in the horizontal buoyancy difference are correlated with changes in the buoyancy gain in the interior over the restratification period, with $r_{Bx} = 0.57$ ($p = 0.06$)

(Figure 1.3b). The correlation between EKE and buoyancy gain is even higher, with $r_{eke} = 0.82$ ($p = 0.002$) (Figure 1.3c). While these correlations are calculated at zero lag, each data point is an average over the 8-month restratification period such that any lag on shorter timescales, i.e. due to the duration of eddy advection, is lost. This high correlation at zero lag is consistent with Fan et al. (2013) who show that eddies with lifetimes of around 4 months travel from the IC to the interior. The improved correlation between EKE and buoyancy gain during restratification indicates that while baroclinic instabilities are likely a major source of buoyancy they are not the only eddy mechanism transporting buoyancy into the interior.

1.5 Discussion

These results show that restratification dynamics govern the differing rates of recovery of the interior and IC from an anomalously dense and weakly stratified state. Due to the widespread nature of the density anomaly (Josey, de Jong, Oltmanns, Moore, & Weller, 2019; de Jong, de Steur, Fried, Bol, & Kritsotalakis, 2020), the IC becomes noticeably denser in 2015 such that there is initially very little change in the horizontal buoyancy gradient between the interior and IC (Figure 1.3a and 1.3b). As the IC is a fast-flowing current (Våge et al., 2011), the anomalously cold waters are flushed from the region relatively rapidly and replenished by lighter, warmer waters from upstream. The recovery of the IC results in an increase in the horizontal buoyancy gradient between the interior and IC from 2016 to 2018, driving faster flow in the IC from 2018-2020 (Fried & Jong, 2022) coincident with a peak in the seasonal buoyancy gain in the interior. This is consistent with baroclinic instabilities resulting in an eddy flux of buoyancy into the interior, as proposed by Spall (2004), Straneo (2006a), and de Jong et al. (2016).

The recovery of each region can be roughly quantified by comparing the deficit in buoyancy content at a given time, relative to the buoyancy content in March 2015 and with the seasonal cycle removed, to the deficit in April 2015 (Table 1.1). While it is expected that the recovery of the interior will take longer than that of the IC given its isolated nature, the interior

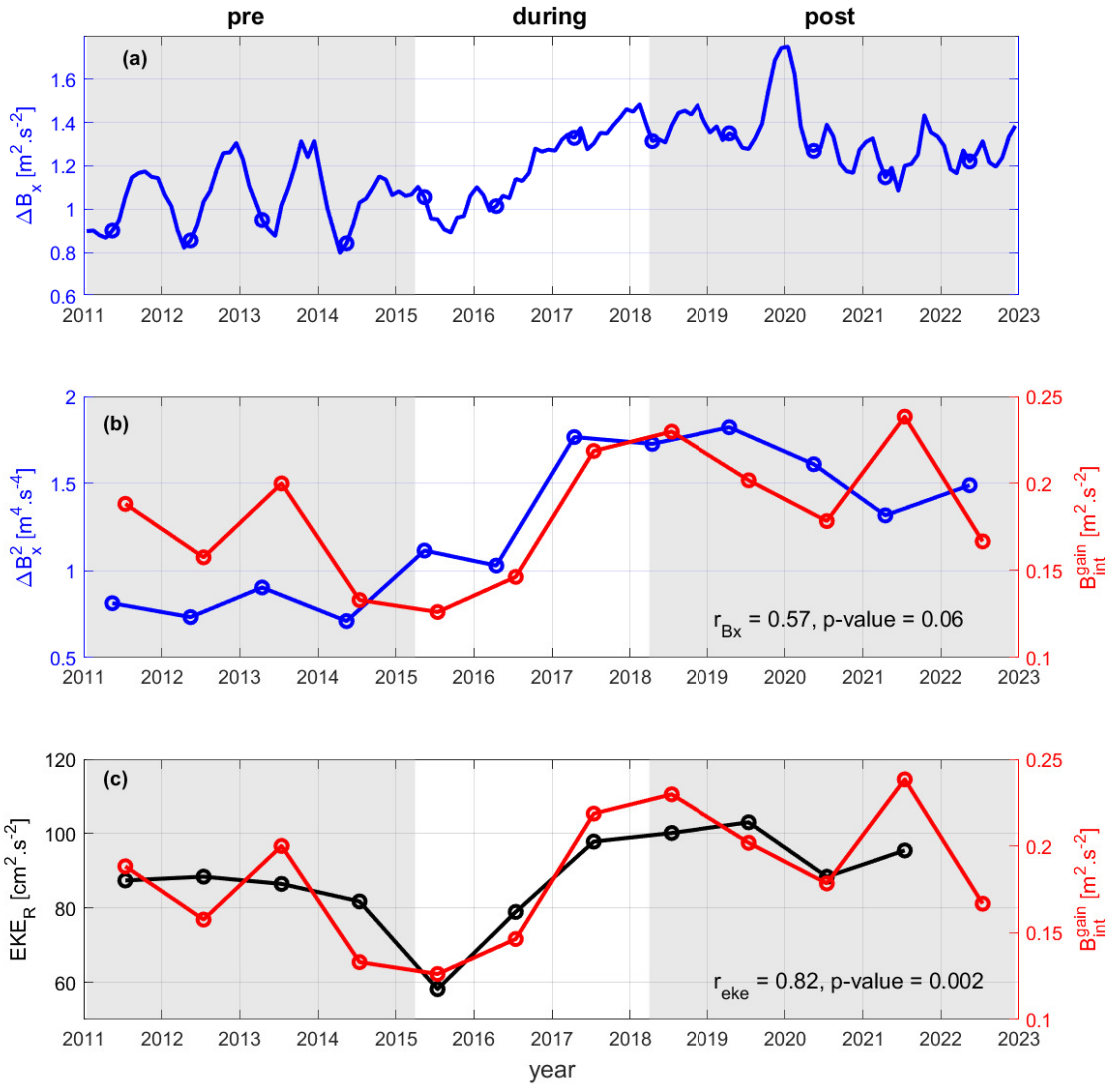

Figure 1.3. (a) Monthly time-series of the horizontal difference in buoyancy content (integrated over the 100-1000 m layer) across the IC, from x1 to x2 (see Figure 1.1a), circles show the ΔB_x value at the start of the restratification period. (b) Comparison of the interannual variability in the square of the horizontal difference in buoyancy content over the IC at the start of the restratification period, ΔB_x^2 (blue) and the buoyancy content gain in the interior over the restratification period in the 100-1000 m layer, B_{int}^{gain} (red). (c) Comparison of the interannual variability in the average EKE in the IC region during the restratification period, EKE_R (black) and B_{int}^{gain} (red).

only recovers 12 % of the lost buoyancy in the first three years - recovering far slower than the typical restratification timescale of a single season (Straneo, 2006a). We propose this is due to

buoyancy loss in the IC resulting in, initially, little change in the horizontal buoyancy gradient, limiting convergence of buoyancy by baroclinic instabilities and delaying the recovery. Notably, the eight years it takes the interior to recover 79 % of the buoyancy deficit is much longer than the single season the buoyancy was lost over and is similar to the 10 years that typically separate strong convective events in the Irminger and Labrador Seas (de Jong & de Steur, 2016; van Aken, de Jong, & Yashayaev, 2011).

While many processes drive exchange between the boundary current and the interior, only a few processes converge buoyancy (ie. light waters) into the interior. In addition to baroclinic instabilities, baroclinic Rossby waves and other eddy generating mechanisms (e.g. barotropic instabilities) on the eastern boundary may provide an additional buoyancy flux to the interior (Våge et al., 2011). These processes could explain the stronger correlation of buoyancy gain at the interior with EKE than with the horizontal buoyancy gradient. Additional processes may contribute to exchange of intermediate and dense water, such as export on the western boundary (Le Bras et al., 2020, 2022) and recirculation in the Irminger gyre (Våge et al., 2011). Here we assume that the effect of these processes on the rate of convergence of light water on the interior is small compared to the baroclinic instability process described above.

The delayed recovery of the interior has implications for wintertime convection. Zunino et al. (2020) found that deep convection was able to persist for three years following the strong winter of 2015 due to pre-conditioning of the water column. We posit that the pre-conditioning lasted multiple years due to the lack of increased seasonal eddy-flux of buoyancy from the IC. Additionally, Biló, Straneo, Holte, and Le Bras (2022) show that a surface salinity anomaly propagated around the Irminger Sea during the late 2010s, suggesting that freshwater accumulation in the interior caused strong convection to cease after 2018. Our results suggest that the freshening of the boundary current may have contributed to the buoyancy gain in the IC that led to the recovery of the interior and ended pre-conditioning.

There are a couple limitations of the analysis presented here. Firstly, the AVISO EKE product only resolves large eddies, with a resolution of $\sim$40 km (Chelton, Schlax, & Samelson,

2011), so smaller-scale turbulence and mixing resulting in exchange between the IC and the interior are not captured here. Secondly, the parameterisation developed by Spall (2004) to describe the eddy flux of buoyancy is based on a model of the Labrador basin, but the Irminger basin has notably different bathymetry: on its eastern boundary the Irminger Sea is bounded by the relatively shallowly sloping Reykjanes Ridge (in a large-scale sense when averaging over very rough small-scale bathymetry). The parameterisation given by Spall (2004) is expected to hold when the bottom slope is less than 1.5 times the isopycnal slope, which is not the case at any point in the time-period studied here. However, the relatively high correlation between the buoyancy gain during restratification and the square of the horizontal buoyancy gradient suggests that the parameterisation holds moderately well. Additionally, the steeper bottom slope on the western boundary still supports the assumption that the eastern boundary is the main source of waters that converge buoyancy to restratify the interior.

In addition to clarifying the restratification process, these results also have important implications for ocean biogeochemistry. Feucher, Portela, Kolodziejczyk, and Thierry (2022) found that the main drivers of the oxygen variability in the region were changes in vertical mixing and horizontal advection, but do not specifically explore eddy-advection from the IC. Given that oxygen concentrations are known to be low over the Reykjanes Ridge (Petit, Mercier, & Thierry, 2019) we suggest that changes in the eddy-flux of water from the IC may contribute to variability in oxygen concentrations in the interior, in addition to the delayed recovery allowing for reventilation of waters not yet exported from the interior (Feucher et al., 2022). Further work is needed to determine whether variability in eddy-flux from the IC significantly affects the oxygen budget of the Irminger interior.

1.6 Conclusion

The densification of the Irminger Sea in 2015 provided an opportunity to study the dynamics of the subsequent restratification and recovery. We find that the recovery of the

Irminger interior was two-stage: an initial slow buoyancy gain while the IC recovered, which set up the necessary conditions to drive a more rapid second-stage recovery of the interior. The restratification of the subsurface water column is shown to be due to eddy-shedding from the IC along the Reykjanes Ridge, primarily as a result of baroclinic instabilities. This result is consistent with findings in the Labrador Sea (Spall, 2004; Straneo, 2006a; de Jong et al., 2016) and speculations about the Irminger Sea (Fan et al., 2013; Sterl & de Jong, 2022). The delayed recovery of the interior is a direct outcome of the changing horizontal density gradient that drives growth of baroclinic instabilities. Because of the two-stage recovery, deep convection in the interior persisted for multiple years in a row, with implications for local biogeochemistry (Feucher et al., 2022). This work shows it is important to consider changes in the IC when considering drivers of variability in stratification, water mass transformation, ventilation and AMOC.

1.7 Acknowledgments

I gratefully acknowledge my coauthors on this work: Fiamma Straneo, Sarah Purkey, and Marieke Femke de Jong. Additionally, I acknowledge the U.S. National Science Foundation: this work was supported by grants OCE-1756272 and OCE-1948482. S.G.P. was supported by NOAA grant NA20OAR4320278. M.F.J. was financially supported by the Innovational Research Incentives Scheme of the Netherlands Organisation for Scientific Research (NWO) under grant 016.Vidi.189.130. I thank all the field teams (scientists, technical staff and crew) that made the hydrographic data collection possible. I thank Tiago Biló for providing the streamlines for the average circulation in the Irminger Sea in from 2006 to 2020 (Figure 1.1a). I thank the reviewers for their time and comments which helped to improve the manuscript for publication with Geophysical Research Letters.

This chapter is a full reprint of the material as it appears in AGU's *Geophysical Research Letters* as "Delayed recovery of the Irminger interior from cooling in 2015 due to widespread

buoyancy loss and suppressed restratification" by M. Nelson, F. Straneo, S. Purkey, and M.F. de Jong (2024). The dissertation author was the primary investigator and author of this paper.

1.A Appendix for Chapter 1

1.A.1 Mean Hydrographic Sections

Three composite summertime potential density sections along AR07-E in the Irminger Sea are created from the hydrographic data to show the change in structure over the study period (Figure 1.1b-1.1d). First, for each cruise, temperature and salinity profiles are interpolated onto a regular 2D grid (0.5 °E horizontal spacing, 10 m vertical spacing) and used to calculate potential density referenced to the surface using the Thermodynamic Equation of State - 2010 (TEOS-10). Cruises are then grouped by year, based on whether strong convection occurred during the following winter season (pre-strong convection: 2010, 2012, 2014; during strong convection: 2015 and 2016; and post-strong convection: 2018, 2020, 2022) and averaged in time. Note that a 2010 occupation was used in the pre-strong convection average as the data from the 2011 occupation of the AR07-E section is unmerged on the CCHDO database and the authors only recently became aware that the line had been occupied that year.

1.A.2 Definitions for regional averages

Regional averages are used to track changes in the Irminger interior and the Irminger Current (IC). The interior is defined as the region where the time-mean mixed layer depth (MLD) is deeper than 650 m during months when the MLD was at least 1000 m somewhere in the Irminger Sea, with a cutoff at 59 °N to the south, similar to Sterl and de Jong (2022) (Figure 1.1a, red crosses). At each grid-point, the MLD is defined as the depth at which the potential density referenced to the surface is 0.03 kg.m^{-3} greater than mean potential density in the upper 30 m. The IC is defined as the region on the eastern boundary where the horizontal density gradient at 300 m is steepest and the EKE is highest (Volkov, 2005; Fan et al., 2013; Sterl & de Jong, 2022)

(Figure 1.1a, magenta crosses).

1.A.3 Density time-series

A time-series of potential density is produced for the interior and IC using the Roemmich and Gilson product (RG product; Figure 1.2a and 1.2b). First, vertical profiles of temperature and salinity at each RG product grid-point are linearly interpolated onto a standard 10 m vertical grid and potential density referenced to the surface is calculated using TEOS-10. Second, a time-series of area-averaged potential density profiles is calculated for the interior (Figure 1.1a, red crosses) and IC (Figure 1.1a, magenta crosses) by averaging all the grid-points in each defined region on all depth-levels for each time-step. Additionally, a time-series of the MLD in the interior is estimated using the time-series of area-averaged potential density profiles (Figure 1.2a, black dashed line). For each profile, the MLD is the depth at which the potential density is 0.03 kg.m^{-3} greater than mean potential density in the upper 30 m.

Similarly, a time-series of the depth-integrated buoyancy content in the 100-1000 m layer is calculated for the interior gyre and IC using the RG product (Figure 1.2c). Vertically interpolated profiles of temperature and salinity at each RG product grid-point are used to calculate in situ density using TEOS-10. A time-series of area-averaged in situ density profiles is then calculated for the interior and IC by averaging all RG grid-points in each defined region on all depth-levels for each time-step. Finally, the buoyancy content within the interior, B_{int}, and IC, B_{ic}, is calculated using Eq. (1.1).

1.A.4 Quantifying gyre recovery

To determine the rates of recovery of the interior and IC the linear trend in B_{int} and B_{ic} is calculated during three distinct time periods from January 2011 to December 2022. The three periods are: pre-strong convection, from January 2011 to March 2015; during strong convection, from April 2015 to March 2018; and post-strong convection, from April 2018 to December 2022. The rate of recovery for each time period is estimated for each region using a Least Squares

regression of a linear trend with a seasonal cycle of B_{int} and B_{ic}; see Eq. (1.2). The standard error in the slope, m, is given by the square root of the variance about the mean (Wunsch, 1996), assuming Eq. (1.2) is the correct model to fit the data and that there is no correlation between the noise in the different model-fitting equations.

1.A.5 Identifying dynamics driving gyre recovery

The seasonal restratification of the interior is quantified by the buoyancy gained in the interior over the restratification period. The restratification period is defined as the time from minimum B_{int} to maximum B_{int} each year such that the buoyancy gain during restratification is $B_{int}^{gain} = \max(B_{int}) - \min(B_{int})$ (Figure 1.3b and 1.3c). This allows the starting and ending months of the restratification period to vary from year to year. We note that alternatively defining the restratification period to be between specified months, eg. April to November, would only change the magnitude of B_{int}^{gain} each year and not the signal of interannual variability. B_{int}^{gain} used here is similar to the difference in Stratification Index used by Sterl and de Jong (2022) or Convective Resistance used by Frajka-Williams, Rhines, and Eriksen (2014), differing by a factor of $\frac{g}{\rho_0}$ and using in situ density rather than potential density.

The relationship between the seasonal dynamics and the multi-year recovery of the gyre is investigated by comparing the buoyancy gain during restratification to the horizontal buoyancy gradient and the EKE. First, the horizontal density gradient across the IC is approximated by differencing the buoyancy content between an inner point (x1, 59.5 °N, -35.5 °E) and an outer point (x2, 58.5 °N, -31.5 °E) of the IC (Figure 1.1a). Using Eq. (1.1), B_{x1} and B_{x2} are calculated using the single grid-point in situ density profiles and differenced at each time-step, $\Delta B_x = B_{x2} - B_{x1}$ (Figure 1.3a). Following Spall (2004) and Straneo (2006a), we take ΔB_x at the start of the restratification period each year (Figure 1.3a, circles) and square it, ΔB_x^2 (Figure 1.3b). The square is taken as the eddy-flux of buoyancy to the interior is set both by the amount of eddies generated (which, in the case of baroclinic instabilities, depends on the horizontal buoyancy gradient) and the buoyancy content of the eddies relative to that of the interior (Spall,

2004; Straneo, 2006b).

Second, we quantify the regional EKE by spatially averaging all AVISO EKE grid points within the IC region (EKE_{ic}, Figure 1.1a). The time-mean of EKE_{ic} is then taken over the restratification period each year (EKE_R, Figure 1.3c). We note that this spatially-averaged EKE is different to that used by Sterl and de Jong (2022), which averages EKE from the Reykjanes Ridge to the edge of the deep convection region to ensure that eddies being considered made it into the interior, but only along the AR07-E line. The area used in our study has a much greater north-south extent but a narrower east-west extent to focus on what is assumed to be the eddy-generation region. Both spatial-averages of EKE produce the same pattern of variability despite the differing definitions.

Finally, we quantify the relationship between ΔB_x^2 and B_{int}^{gain} and EKE_R and B_{int}^{gain} by the linear correlation, r_{Bx} and r_{eke} respectively. r_{Bx} is indicative of how much buoyancy gain in the interior is provided by eddies resulting from baroclinic instabilities, following Straneo (2006a). r_{eke} is indicative of how much buoyancy gain is provided by any mesoscale eddies, following Sterl and de Jong (2022). Any difference between r_{Bx} and r_{eke} is indicative of how much eddy-activity is due to processes other than baroclinic instabilities, as well as the error in the estimates.

Chapter 2

Observations of water mass modification and cross-shelf exchange at Narsaq Trough, Greenland

Abstract

Cross-shelf exchange at Greenland's continental margins transports warm waters towards the glacier margins and freshwater offshore into the convective basins of the North Atlantic and Nordic Seas. Several studies have suggested that the exchange is enhanced by the presence of deep, glacial troughs, but observations from Greenland's troughs are scarce. This work presents data from a ship-based survey at Narsaq Trough, a wide, branched trough in southwest Greenland, during the summer of 2022. We use Conductivity-Temperature-Depth-Oxygen profiles, water samples for nutrient analysis, and underway current profiles to compare the water mass properties and distribution inside and outside the trough, describe the flow-field in and around the trough, and estimate mixing in the trough. Narsaq Trough is found to provide a pathway for warm, salty Atlantic Water to intrude onto the continental shelf where these waters are mixed with the overlying cold, fresh Polar Water. As a result, waters in the trough are fresher, oxygen-enriched, macronutrient-depleted, and at times colder, relative to the unmodified Atlantic Water offshore. This trough-modified water has the potential to freshen and oxygenate the flow on the shelf-break and/or reduce the thermal forcing of waters in the adjacent fjord, limiting ice melt.

2.1 Introduction

At the Greenland continental shelf-break warm, salty Atlantic Water abuts cold, fresh Polar Water. The Atlantic Water is found offshore, largely separated from the Polar Water by the dynamic boundary of the current system and topography of the shelf-break. The rate of cross-shelf exchange in the region controls the net exchange of freshwater offshore and heat onshore, with climatically important impacts. First, freshwater transport offshore affects vertical stratification in the convective basins of the subpolar North Atlantic and is projected to contribute to the slowdown of the Atlantic Meridional Overturning Circulation in a warming climate (Schiller-Weiss et al., 2024; Rahmstorf et al., 2015; Swingedouw et al., 2022; Bakker et al., 2016). Second, heat transport onshore determines the ocean thermal forcing experienced

by marine-terminating glaciers that drain the Greenland Ice Sheet and thus affects sea level rise (Wood et al., 2021; Straneo & Heimbach, 2013; Sutherland et al., 2013; Slater & Straneo, 2022). While cross-shelf exchange is known to be driven by eddies and wind stress (Castelao et al., 2019; Snow et al., 2023), the rate may be enhanced by the presence of numerous troughs on Greenland's continental shelf (Sutherland & Cenedese, 2009; Snow et al., 2021, 2023).

Troughs of different sizes, orientations, and geometries incise the continental shelf all around Greenland (Figure 2.1a). These troughs are deep gouges, carved by glaciers during past glacial periods, extending from the mouths of fjords towards the shelf-break (Arndt et al., 2015; Evans, Ó Cofaigh, Dowdeswell, & Wadhams, 2009). These bathymetric features provide a pathway for deeper waters to access the inner-shelf (Morlighem et al., 2017).

Additionally, a number of prior studies, mostly in Antarctica, have shown that troughs modify their local environment and contribute to cross-shelf exchange. When flow encounters a trough, bathymetric steering can deflect the current, both above and below the shelf, and set up eddies within the trough (St-Laurent, Klinck, & Dinniman, 2013; Sutherland & Cenedese, 2009; Beardsley, Limeburner, & Brechner Owens, 2004; Silvano et al., 2022). Eddies, wind-reversals, and breaking Rossby waves drive episodic injections of warm water onshore at troughs (Moffat, Owens, & Beardsley, 2009; Brearley, Moffat, Venables, Meredith, & Dinniman, 2019; Snow et al., 2023; St-Laurent et al., 2013). Inside Antarctic troughs, mixing is known to drive an upward flux of heat and salt, which cools and freshens the intruded water (Klinck, 1998). This mixing can result from velocity shear created by wind-driven currents and flow encountering topography (S. L. Howard, Hyatt, & Padman, 2004; Venables, Meredith, & Brearley, 2017; Brearley, Meredith, Naveira Garabato, Venables, & Inall, 2017; Scott, Brearley, Naveira Garabato, Venables, & Meredith, 2021). As such, troughs in Antarctica are known to be an effective pathway for moving warm water towards the coast and across the pycnocline (Moffat & Meredith, 2018; Couto, Martinson, Kohut, & Schofield, 2017). In Greenland, the shallower continental shelves generally contain a single cold, fresh layer (Pacini et al., 2021; Le Bras, Straneo, Holte, & Holliday, 2018); whereas the deeper continental shelves in Antarctica can support a two-layer

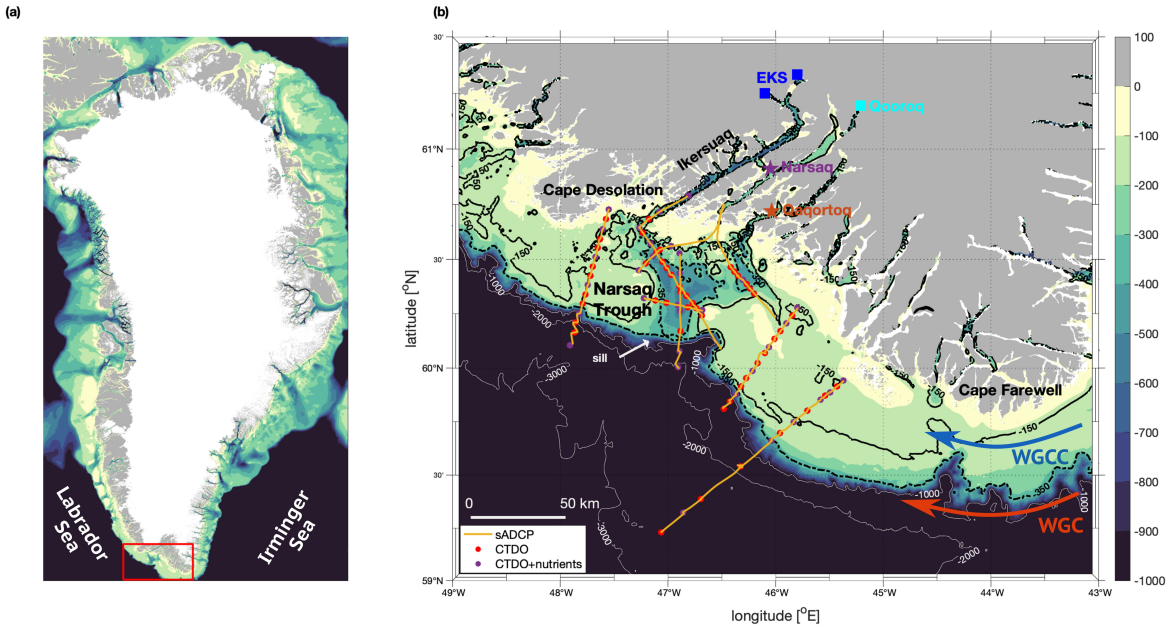

Figure 2.1. Study region. (a) Bathymetry of the Greenland continental shelf, with the location of Narsaq Trough indicated (red box). (b) Close up of Narsaq Trough bathymetry with observations overlain: sADCP (yellow lines), CTD stations (red circles), and CTD stations with nutrient samples (purple circles). The location of two towns, Qaqortoq (orange star) and Narsaq (purple star), are shown; along with with two outlet glaciers, Eqalorutsit Kangigdlit Sermiat (EKS, two tongues; blue squares) and Qooroq (cyan square). Cape Farewell, Cape Desolation, and Ikersuaq fjord are labeled. Isobaths indicating the trough rim depth (-150 m, solid black), sill depth (-350 m, dashed black), and -1000 m increments (white) are shown. The directions of the West Greenland Current (WGC; red arrow) and West Greenland Coastal Current (WGCC; blue arrow) are marked.

system with warmer off-shelf waters underlying the cold shelf waters, even outside of troughs (Moffat & Meredith, 2018). As such, troughs in Greenland may play a greater role in enabling warm, salty waters to access the shelf region than Antarctic troughs.

Hypotheses about the role of troughs on the Greenland shelf can be further developed based on knowledge of submarine canyons. Here, we consider troughs to be bathymetric features carved by glaciers, stretching from the coast across the shelf; whereas canyons are formed through erosion at the shelf-break, cutting down and back from the shelf-break (Harris & Whiteway, 2011; Shepard, 1981). Like canyons, we expect dynamically wide troughs (trough width greater than the radius of deformation), such as Narsaq Trough (30 km$>\sim$ 10 km), to steer the flow to follow bathymetry and drive vertical velocities inside the trough (Klinck, 1996; Allen & Hickey, 2010; Freeland & Denman, 1982; Spurgin & Allen, 2014). For the Greenland case, where the troughs are right-bounded (incident flow has the coast to the right) and the pressure gradient is offshore, canyon theory suggests the flow will be steered into the trough along the upstream wall, decelerate, and be pushed deeper by the reduced Coriolis acceleration. On the downstream wall, the flow is steered back out of the trough and accelerated by the pressure gradient, increasing the Coriolis acceleration and lifting the flow back up. However, unlike canyons which are typically deepest at the mouth, troughs often have a shallow sill-type feature at the mouth which impedes the exchange between off-shelf waters and the deepest waters in the trough (Moffat & Meredith, 2018).

A handful of studies (e.g. Sutherland & Cenedese, 2009; Snow et al., 2021, 2023) suggest that Greenland troughs enhance cross-shelf exchange and modify water properties on the shelf. However, limited observations from Greenland's continental margins have made it difficult to confirm their role and understand the local trough dynamics. Here we present novel physical and biogeochemical data from a ship-based survey of Narsaq Trough, in southwest Greenland, to describe how the bathymetric feature steers flow, drives cross-shelf exchange, and modifies Atlantic Water through enhanced mixing.

2.1.1 Study Region: Narsaq Trough

Narsaq Trough is a wide, branched trough in southwest Greenland, located near the city of Qaqortoq (formerly Julianehåb) and bracketed by Cape Farewell and Cape Desolation (Figure 2.1b). The trough is 30 km wide at its mouth, narrowing to 25 km before splitting into two branches. It spans the width of the continental shelf, approximately 50 km. The trough is noticeably deeper than the 150 m average shelf depth (i.e. rim depth), reaching 600 m deep at its deepest point (Figure 2.1b). However, there is a 350 m deep sill at the mouth of the trough which blocks exchange of the deep trough waters with waters offshore (Figure 2.1b, dashed black line). The sill depth is defined as the deepest isobath connecting the trough to off-shelf waters. The southeastern branch is isolated from the main trunk of the trough by a second 300 m deep sill; whereas the northwestern branch is contiguous with the main trunk until it meets a series of progressively shallower sills ($\sim$200 m deep) at the mouth of Ikersuaq fjord (Bredefjord). Two large marine-terminating glaciers drain into the fjords that open onto Narsaq Trough: Eqalorutsit Kangigdlit Sermiat (two tongues) and Qooroq (Figure 2.1b, blue and cyan squares); in addition to several smaller marine- and land-terminating glaciers.

Two currents flowing along the coast in this region are likely to be affected by Narsaq Trough: the West Greenland Current (WGC) and the West Greenland Coastal Current (WGCC) (Figure 2.1b). The WGC is a coherent full-depth, surface-intensified flow located on the shelf-break that carries warm, salty, oxygen-poor Atlantic Water (AW) (Pacini et al., 2020). The WGCC, on the other hand, is less coherent; at times identifiable as a unique, shallow core on the continental shelf carrying cold, fresh, oxygen-rich Polar Water (PW), at times merged with the WGC, and at times not present at all (Foukal & Pickart, 2023; Gou, Feucher, Pennelly, & Myers, 2021; Lin, Pickart, Torres, & Pacini, 2018). The strength and location of both the WGC and WGCC are influenced by local winds (predominantly upwelling favourable) and remote winds (predominantly downwelling favourable), such that the flow structure is highly variable in time (Foukal & Pickart, 2023; Moore & Renfrew, 2005).

2.2 Data

2.2.1 Shipboard Observational Survey

An observational survey of Narsaq Trough was carried out from 5-21 September 2022 on the *R/V Neil Armstrong*. The survey was part of the Overturning in the Subpolar North Atlantic Program (OSNAP) cruise AR69-03, which took place from 19 August to 24 September 2022. 8 transects in and around Narsaq Trough were conducted: 4 cross-shelf transects (far upstream, upstream, midstream, and downstream); 3 cross-trough transects (cross-trunk, northwest branch, southeast branch); and a final transect along the northwestern branch and into the fjord (inner midstream) (Table 2.1). 82 conductivity-temperature-depth (CTD) stations were occupied over these 8 transects where a SBE911plus system was used to measure temperature and salinity with depth (Figure 2.1b). An auxiliary SBE 43 oxygen sensor, calibrated with Winklers, was also used. The CTD analysis presented here uses data binned onto 2 dbar pressure levels, except for the Thorpe scale analysis, which uses the 24 Hz data. At 49 stations, discrete water samples were collected for nutrient analysis (nitrate, nitrite, silicate, and phosphate). Ocean current velocities were measured along each transect using a Teledyne RDI 150 kHz Ocean Surveyor shipboard acoustic Doppler current profiler (sADCP). The measured velocities were detided using the Greenland 1 km barotropic tidal model (Gr1kmTM) from Earth and Space Research institute (S. L. Howard & Padman, 2021). High resolution bathymetry was measured under the ship-track using the center beam from two shipboard multibeam sonars (Kongsberg EM 122 and EM710). Further details about each of these observational datasets are given in the 2.A.1-2.A.4 along with a map of the transects as labeled in Table 2.1 (Figure 2.9).

2.2.2 Drifter Trajectories

During the AR69-03 cruise, 12 surface drifters were deployed while on the East Greenland shelf between 60-62.3 °N, all on the inner-shelf (Figure 2.10a). The drifters were drogued at 15 m and record position hourly. The eight drifters that traveled past Narsaq Trough are used in this

Table 2.1. Survey transect timing, number of stations, angle of rotation of ocean velocity coordinates (θ_{rot}), and mean along-shelf wind stress during transect, τ^{along} (positive for downwelling-favourable and negative for upwelling-favourable).

Transect[a]	Timeframe (2022, UTC)	stations	θ_{rot}[b]	τ^{along} (N.m^{-2})[c]
(A) Far upstream	22:36 5 Sept - 02:37 7 Sept	13	39°	-0.02
(B) Midstream	20:04 7 Sept - 05:19 8 Sept	7	87°	-0.03
(C) Cross-trunk	22:08 14 Sept - 03:45 15 Sept	6	78°	0.04
(D) Northwest branch	05:03 15 Sept - 09:31 15 Sept	5	-	0.13
(E) Southeast branch	20:33 16 Sept - 02:03 17 Sept	7	-	0.09
(F) Upstream	16:53 17 Sept - 04:42 18 Sept	14	53°	-0.00
(G) Inner midstream	01:05 20 Sept - 16:38 20 Sept	15	-	-0.14
(H) Downstream	19:59 20 Sept - 12:29 21 Sept	15	74°	-0.36

[a]See Figure 2.9 for a map of labeled transects.
[b]Angles of rotation are counter-clockwise from the North-East reference frame.
[c]Local winds over the trough during transit occupation (see 2.A.5, Figure 2.11).

study (Figure 3.3a). The other four drifters ran aground (two prior to rounding Cape Farewell, a third on the islands just upstream of the trough, and the fourth on the coast near the southeast branch of the trough; Figure 2.10a). Trajectories presented here are unsmoothed. The positional accuracy of the GPS is 2-7 m.

2.2.3 Bathymetry Maps

For maps presented here, a blended bathymetry product is used which combines BedMachine Greenland (Morlighem et al., 2017) and Etopo1 (NOAA National Geophysical Data Center, 2009; Amante & Eakins, 2009). As BedMachine only extends to the edge of the continental shelf at the southern tip of Greenland, Etopo1 is used to fill in outside of the BedMachine coverage. The resulting product is a 1/200° latitude and longitude grid. The exception is Figure 2.1a, which uses the original BedMachine product.

2.3 Methods

2.3.1 Velocity Rotations

The sADCP velocity sections presented here are rotated into components referenced to the local bathymetry. For the cross-shelf transects (e.g. Figure 2.3), the velocity is decomposed into along- and cross-shelf components, approximately following the local 1000 m isobath. Positive along-shelf velocity is towards the northwest (with the mean flow) and positive cross-shelf velocity is onshore. For the cross-trough section (Figure 2.6e), the velocity is decomposed into in- and cross-trough components, approximately following the local 150 m isobath. Positive in-trough velocity is onshore. The angles of rotation, θ_{rot}, where rotation angles are counter-clockwise from the North-East reference frame, are given in Table 2.1.

2.3.2 Section Gridding

The temperature, salinity, oxygen, nutrient, and velocity profile data were gridded along the far upstream, midstream, cross-trunk, and inner-midstream sections (Figures 2.3, 2.4, 2.6, and 2.7) using the `gridfit` function written for MATLAB. This gridding interpolates over any data gaps and extrapolates out to the bathymetric boundaries. `gridfit` uses a modified ridge estimator to generate 2D surfaces from scattered data, with a bias towards smoothness (D'Errico, 2006). The triangle interpolation scheme was used, which splits each cell into a triangle and linearly interpolates inside each triangle. For the long transects (far upstream, midstream, downstream, and inner-midstream) a horizontal smoothing scale of 10 and a vertical smoothing scale of 0.5 was used. For the cross-trunk transect a smaller horizontal smoothing scale of 7 (stations are closer together) and a longer vertical smoothing scale of 0.9 (overall range of depths is smaller) were used. The smoothing scales control the tradeoff between data fitting and smoothness of the surface and cannot be converted into metres. The nutrient data were linearly interpolated onto 2 dbar pressure levels to match the vertical resolution of the temperature, salinity, and oxygen data prior to gridding.

2.3.3 Profile Averaging

To investigate whether unique water properties are found in Narsaq Trough, composite profiles were created to characterise the in-trough, far upstream on-shelf, and far upstream off-shelf environments (Figure 2.5). The 150 m isobath was used to separate the on- and off-shelf stations along the far upstream transect. The in-trough region composite was made from stations deeper than 350 m inside the main trunk of the trough. For each region, the mean and standard deviation of the conservative temperature, absolute salinity, and dissolved oxygen profiles was calculate at each pressure level across all profiles. Data from depths where only one profile exists are excluded.

2.3.4 Volume, Heat, Freshwater and Oxygen Transports

The volume, heat, freshwater and oxygen exchanges across the trough's trunk were estimated by calculating the inflow and outflow at the cross-trunk transect, between the trough rim and sill (i.e 150-350 m; Table. 2.2, see Figure 2.6 for transect location). Transports were calculated using the gridded temperature, salinity, oxygen and in-trough velocity fields. The zero-crossing of the depth-integrated velocity over the sill-to-rim layer was used to divide the inflow from the outflow, which was found to be at $x_0 = 15.9$ km. Transport fields were then vertically integrated over the sill-to-rim layer and horizontally integrated over the inflow ($x1 = 0, x2 = x_0$ km) and outflow ($x1 = x_0, x2 = 30$ km). Volume transport is thus calculated as

$$\text{Volume transport} = \int_{x1}^{x2} \int_{-350}^{-150} u_{in-trough}(x,z)\, dz\, dx\ , \tag{2.1}$$

where $u_{in-trough}(x,z)$ is the gridded along-trough velocity field. Heat transport is calculated as

$$\text{Heat transport} = \rho_0 c_p \int_{x1}^{x2} \int_{-350}^{-150} u_{in-trough}(x,z)\, T(x,z)\, dz\, dx\ , \tag{2.2}$$

where $\rho_0 = 1027$ kg.m^{-3}, $c_p = 3850$ J.kg^{-1}.K^{-1}, and $T(x,z)$ is the gridded conservative temperature field in Kelvin. Freshwater transport is calculated with respect to a reference salinity of $S_{ref} = 35.1$ g.kg^{-1} (which is the depth-averaged salinity over the 150-350 m layer of the far upstream composite profile, see Section 2.3.3),

$$\text{Freshwater transport} = \int_{x1}^{x2} \int_{-350}^{-150} u_{in-trough}(x,z) \frac{S_{ref} - S(x,z)}{S(x,z)} \, dz \, dx \, , \tag{2.3}$$

where $S(x,z)$ is the gridded absolute salinity field in g.kg $^{-1}$. Finally, the oxygen transport is calculated as

$$\text{Oxygen transport} = \rho_0 \int_{x1}^{x2} \int_{-350}^{-150} u_{in-trough}(x,z) \, DO(x,z) \, dz \, dx \, , \tag{2.4}$$

where $DO(x,z)$ is the gridded dissolved oxygen field in μmol.kg^{-1}.

2.3.5 Mixing Analysis

Estimating Turbulent Dissipation Rate and Vertical Diffusivity

To quantify turbulent fluxes of heat or other tracers across isopycnals in the vicinity of the trough, an estimate of the turbulent mixing is needed. This can be estimated through the turbulent dissipation rate, ε, the key variable that drives overturning and mixing in a stratified water column (Osborn, 1978). Here, we estimate ε from vertical density overturns using estimates of the Thorpe scale, L_T (Thorpe, 1997; Galbraith & Kelley, 1996), and the Ozmidov scale, L_O (Ozmidov, 1965):

$$\varepsilon = (cL_T)^2 N^3, \tag{2.5}$$

where $c = L_O/L_T = 0.8$ (Dillon, 1982) and N is the buoyancy frequency.

We quantify the turbulent dissipation rate using the 24 Hz CTD data. These data were corrected for the lag between the temperature and conductivity cell, pressure and temperature were despiked and delooped, and finally salinity was despiked. Following Fer, Skogseth, and

Haugan (2004), each observed potential density profile was used to create an artificial density profile by re-ordering it to be gravitationally stable. Then, we estimate the vertical displacements needed to move fluid parcels from their depths in the observed profile to the reordered profile, within the depth span of a given overturn. The Thorpe scale is defined as the root-mean-square of all non-zero displacements. We use a minimum run length criteria of 6 m (Fer et al., 2004) and a minimum overturn size of 2 m to distinguish overturns from noise and error. The orders of magnitude of the ε estimates presented here are not sensitive to changes in the run length and overturn size criteria between 1 and 10 m. Finally, the ε estimates are averaged over 10 m bins (Figure 2.5c and 2.7f). Note that during the cross-trough transect (Figure 2.6) the CTD heave due to the ship motion was too big to make reliable estimates of dissipation using this method.

The vertical diffusivity in the trough, κ_z, can then be estimated from ε following Osborn (1980): $\kappa_z = \gamma\varepsilon/N^2$, where γ is the mixing efficiency and we assume $\gamma = 0.2$.

Advection-Diffusion Model

A simplified advection-diffusion model, described by Voet et al. (2015), is used to provide an upper bound estimate of the local vertical dissipation needed to create the observed sub-surface cross-trough salinity and oxygen gradient. While this advection-diffusion model does not include the effects of convergences of meltwater with the oceanic water, it provides an order of magnitude estimate of one of the mechanisms resulting in the observed gradients in the trough. The model estimates the magnitude of vertical diffusivity needed to modify the inflowing waters to match the outflow properties. Briefly, following Hautala, Reid, and Bray (1996), the vertical mixing of tracer concentration C can be modeled as

$$\frac{DC}{Dt} = \kappa_z \frac{\partial C}{\partial z} \,. \tag{2.6}$$

The observed change in the tracer is dependent on κ_z and the time scale, t_c, over which the change occurs. These two parameters can be combined into a vertical spreading scale, $\lambda = (\kappa_z t_c)^{1/2}$.

Here, we apply the advection-diffusion model to the T-S profile in the core of the inflow in the cross-trunk section (Figure 2.6, second profile from the right) and determine the vertical spreading scale needed to match the T-S properties of the core of the outflow (Figure 2.6, fourth profile from the left). The tracer concentrations (T and S in this case) are held constant at 100 m and a no flux boundary condition is imposed at the bottom.

2.4 Results

Below we describe findings from the observational survey. First, we describe how the flow-field and water mass distribution over the continental shelf differs at the trough compared to up- and down-stream. Second, we show that the trough creates a unique in-trough environment that supports a sub-surface circulation. Third, we present estimates of the turbulent dissipation rate and diffusivity to evaluate the water mass transformation and mixing occurring in the trough.

2.4.1 Cross-Shelf Structure of Flow-Field and Water Mass Distribution

The flow-field at Narsaq Trough was observed to have a different structure than upstream or downstream of the trough, with no clear WGCC core over the trough and with notable cross-shelf flow in and over the trough (Figure 3.3 and 2.3). For this analysis, we define the WGC as the velocity core located at or off the shelf-break, with salinities greater than 34 $g.kg^{-1}$ (Pacini et al., 2020; Foukal & Pickart, 2023). The WGCC is identified as a separate core if there is a velocity peak inshore of the WGC core, typically with salinities less than 33 $g.kg^{-1}$ (Foukal & Pickart, 2023).

At the surface, there are two main pathways for flow passing the trough: the trough deflects the WGCC onshore while the WGC continues to follow the shelf-break (Figures 3.3a and 3.3b). The salty WGC core follows the large-scale bathymetry of the shelf-break at all cross-shelf transects, although the width of the current varies and is not always fully captured. Whereas the fresher WGCC is directed towards the coast upstream and back out towards the shelf-break downstream. While a clear WGCC core was not observed at the midstream transect

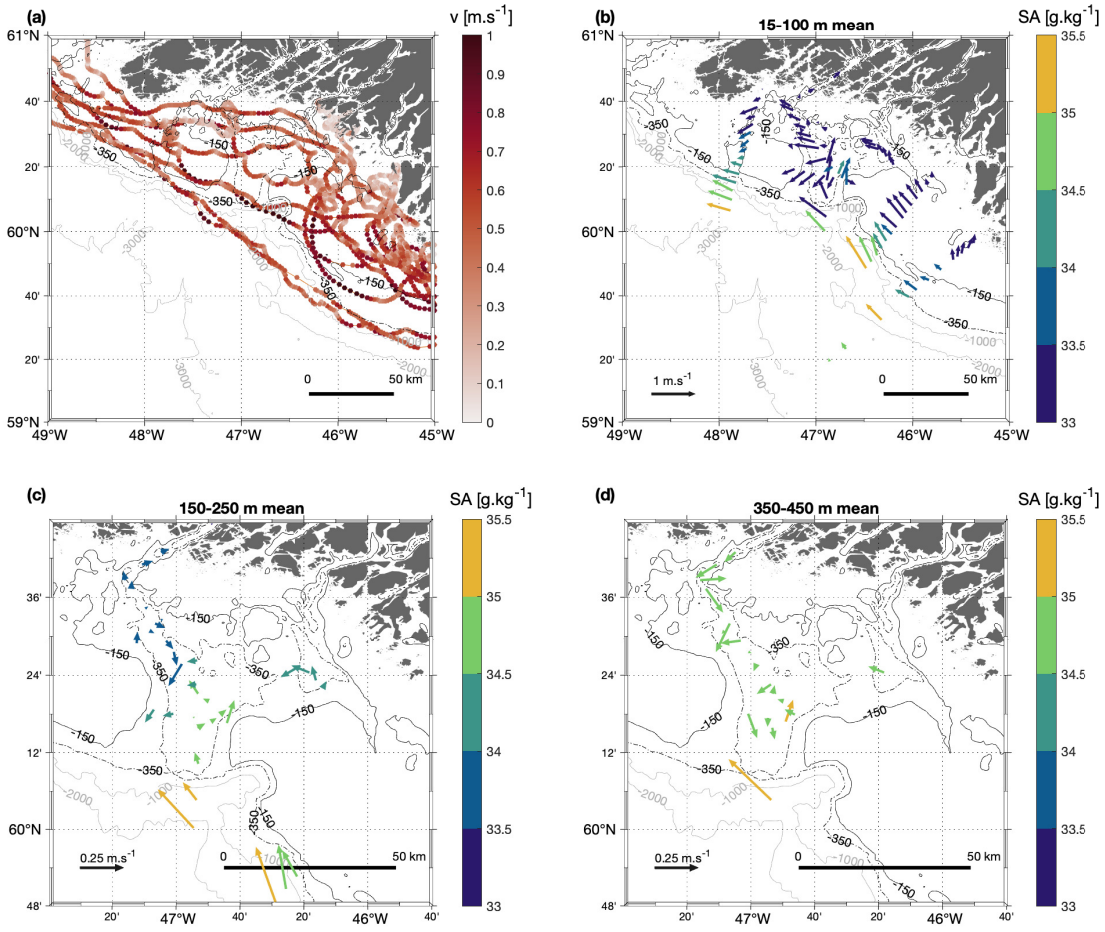

Figure 2.2. Flow-field at Narsaq Trough. (a) Surface drifter trajectories coloured by drifter speed. Depth-averaged velocities in the (b) 15-100 m layer, (c) 150-250 m layer (rim-depth), and (d) 350-450 m layer (below the sill). In (b-d) velocity vectors are coloured by layer-averaged salinity at the corresponding CTD stations. Note that the differing vector scales.

it may have been located in the gap between the end of the transect and the coast. In sum, these observations are illustrative of the WGCC following isobaths and being deflected around the head of the trough.

Surface drifter trajectories past the trough in August to October 2022 are consistent with the two identified pathways (Figure 3.3a). Each drifter took 2-7 days to cross the trough (from -46 °E to -48 °E), except one which took 15 days (Figure 2.10b). Drifters in the WGC (between the 150 m and 2000 m isobath) upstream of the trough have relatively fast, well-organized trajectories and follow the shelf-break past the trough undeflected. On the other hand, drifters

on the shelf have slow, eddying, poorly-organized trajectories upstream of the trough and are mostly deflected around the head of the trough. The drifters on the shelf emerge downstream of the trough in a more coherent, faster WGCC pathway. One drifter passed slowly over the trunk of the trough, while two drifters that start on the shelf exit the shelf and join the WGC while passing the trough.

Consistent with past studies, upstream of the trough the continental shelf separates the warm, salty, oxygen-poor Atlantic Water (AW) in the WGC (peak along-shelf velocity of 0.6 $m.s^{-1}$, 75 km offshore) from the cold, fresh, oxygen-rich Polar Water (PW) in the WGCC (Figures 2.3b-2.3e; peak along-shelf velocity of 0.3 $m.s^{-1}$, 25 km offshore). There is very little cross-shelf velocity far upstream, consistent with weak wind forcing during the transect (Figure 2.3f, Table 2.1). In contrast, at the trough, AW is observed inshore of the shelf-break, under the PW (Figures 2.3g-2.3i), consistent with strong onshore cross-shelf velocity at the mouth of the trough (Figure 2.3k, 0-400 m deep, 60-75 km offshore). The onshore velocity cannot simply be explained by the local wind forcing during the transect (weak winds; Table 2.1). The WGC core remains intact past the trough mouth (Figure 2.3j; peak along-shelf velocity of 0.4 $m.s^{-1}$, 75 km offshore, with a stronger surface core peaking at 0.7 $m.s^{-1}$, 65 km offshore), whereas there is no evidence of the WGCC passing over the trough. Additionally, an eddy-like pulse of AW was observed 20 km inshore of the shelf-break at the depth of the rim of the trough (Figures 2.3g-2.3i, circled in white), discussed further in Section 2.5.1.

The cross-shelf distribution of nutrients in the trough is also notably different than far upstream (Figure 2.4). Far upstream, the on-shelf waters are depleted in macro-nutrients (nitrate, phosphate, and silicate), whereas off-shelf macro-nutrient concentrations are higher in the surface waters and increase further with depth (Figures 2.4b-2.4d). Over the trough, low macro-nutrient surface waters extend past the shelf-break and waters below the shelf depth are depleted in nutrients relative to waters at the same depth off-shelf (Figures 2.4f-2.4h). Nitrite concentrations are high in the upper 200 m both on- and off-shelf far upstream, with no nitrite at depth (Figure 2.4e). In the trough, however, high nitrite waters are only found below 200 m (Figure 2.4i).

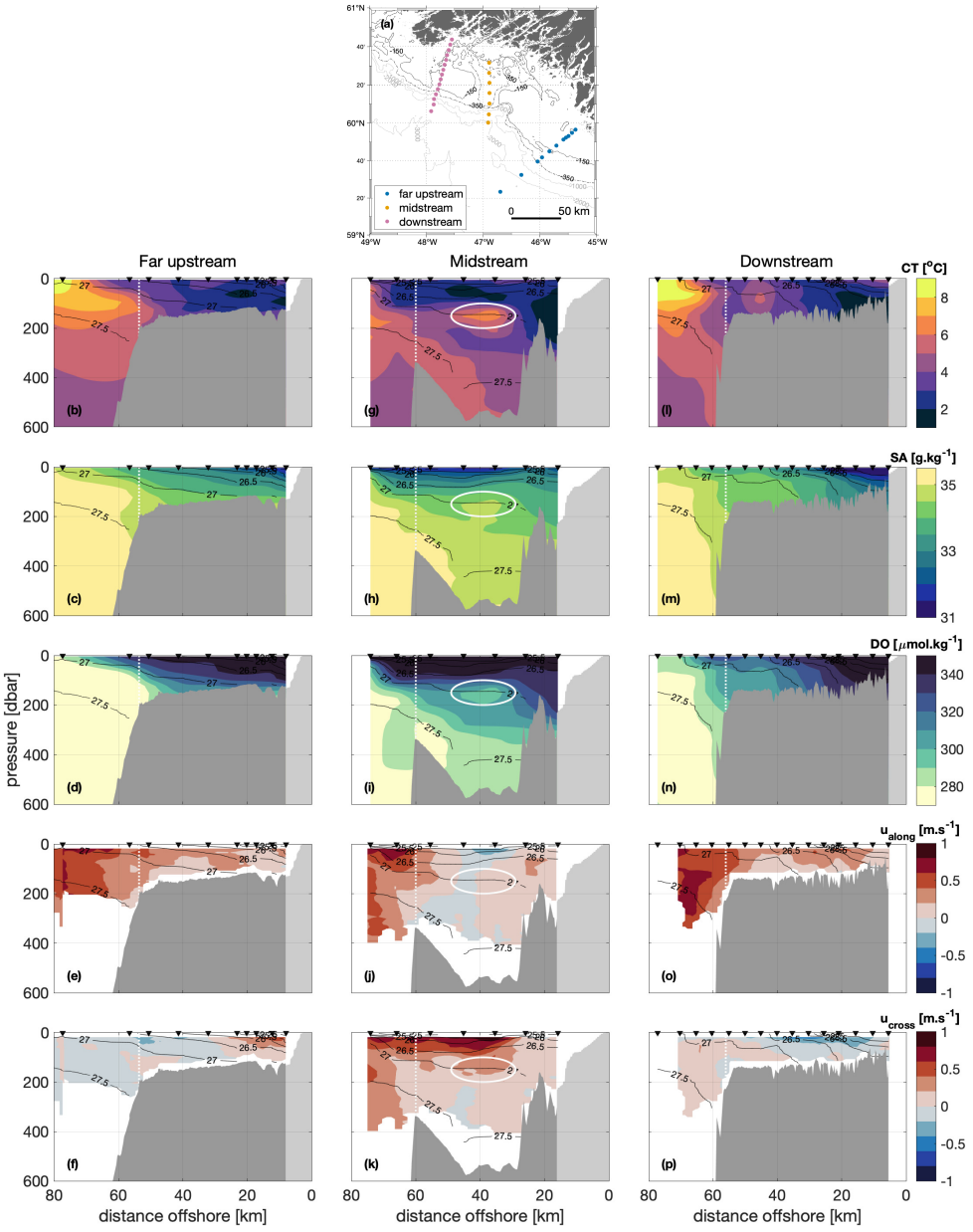

Figure 2.3. Water properties and flow-field along three cross-shelf transects at Narsaq Trough: (b-f) far upstream, (g-k) midstream (in-trough), and (l-p) downstream; transect locations are shown in (a). (b, g, l) Conservative temperature, (c, h, m) absolute salinity, (d, i, n) dissolved oxygen, (e, j, o) along-shelf velocity (positive to the northwest), and (f, k, p) cross-shelf velocity (positive onshore). In (b-p) isopycnals of potential density (black lines) and CTD stations (black triangles) are overlain. Along-track bathymetry is from the shipboard multibeam sonar (dark grey), extended to the coast using the BedMachine-Etopo product (light grey). The shelf-break is denoted by the white dotted line and an eddy-like feature in the midstream sections is circled in white.

Downstream of the trough properties and velocities generally resemble the upstream distribution, with several relevant changes: Firstly, a warm anomaly is observed inshore of the shelf-break (5 °C, 45 km offshore; Figure 2.3l). Secondly, the PW is more tightly banked up against the coast, driving a more coherent WGCC (Figures 2.3l-2.3o). Thirdly, waters above the sill depth, offshore of the shelf-break, are lighter, fresher, and more oxygen-rich downstream than far upstream (Figures 2.3m and 2.3o; 150-350 m, 60-70 km offshore). Finally, waters with lower macro-nutrient concentrations are found on the continental slope downstream (Figures 2.4j-2.4l; 400-600 m, 60-70 km offshore), where there are none upstream (Figures 2.4b-2.4d). These differences cannot be explained by the upwelling winds during the transect.

2.4.2 Unique In-Trough Environment

By comparing composite profiles of waters in and upstream of Narsaq Trough the differences in water properties are evident. Far upstream, the off-shelf waters have typical AW properties: warm, salty, dense, and oxygen-poor (Figures 2.5d-2.5g, pink); and the on-shelf waters have typical PW properties: cold, fresh, light, oxygen-rich (Figures 2.5d-2.5g, blue). At the trough, waters above the rim of the trough have properties that are indistinguishable from the on-shelf waters far upstream; while waters below the rim of the trough are fresher, lighter, more oxygen-rich, and, at times, colder than the off-shelf waters far upstream (Figures 2.5d-2.5g, orange). These differences are largest between the rim and sill depth (150-350 m). The unique in-trough waters appear to be a mixture of AW and PW, spanning the gap between AW and PW in T-S space. Specifically, the distribution of points in T-S space is suggestive of mixing occurring both along (27 $kg.m^{-3}$) and across (between 27-27.5 $kg.m^{-3}$) isopycnals (Figure 2.5b). This mixing is analysed in Section 2.4.3.

Below the sill depth, waters in the trough are on average warmer than waters at the same depth off-shelf (Figure 5d), consistent with the sill setting the depth of exchange between deep waters in the trough and off-shelf waters. As such, we expect the water properties below the sill depth in the trough to have similar properties at sill depth off-shelf. Additionally, a small vertical

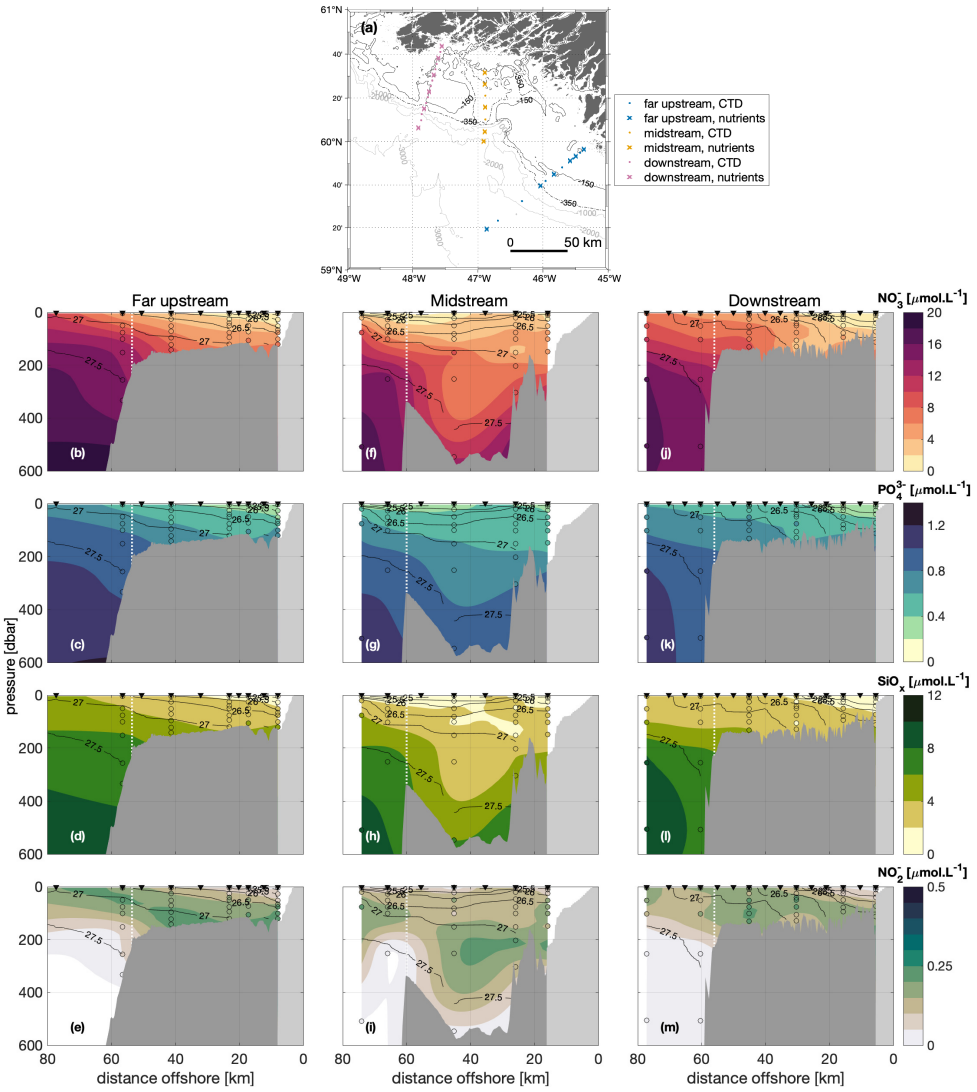

Figure 2.4. As in Figure 2.3, but for nutrient concentrations: (b, f, j) nitrate, (c, g, k) phosphate, (d, h, l) silicate, and (e, i, m) nitrite, with discrete nutrient concentrations used in interpolation overlain (circles). In (a) stations with nutrients samples (crosses) are distinguished from those without (dots).

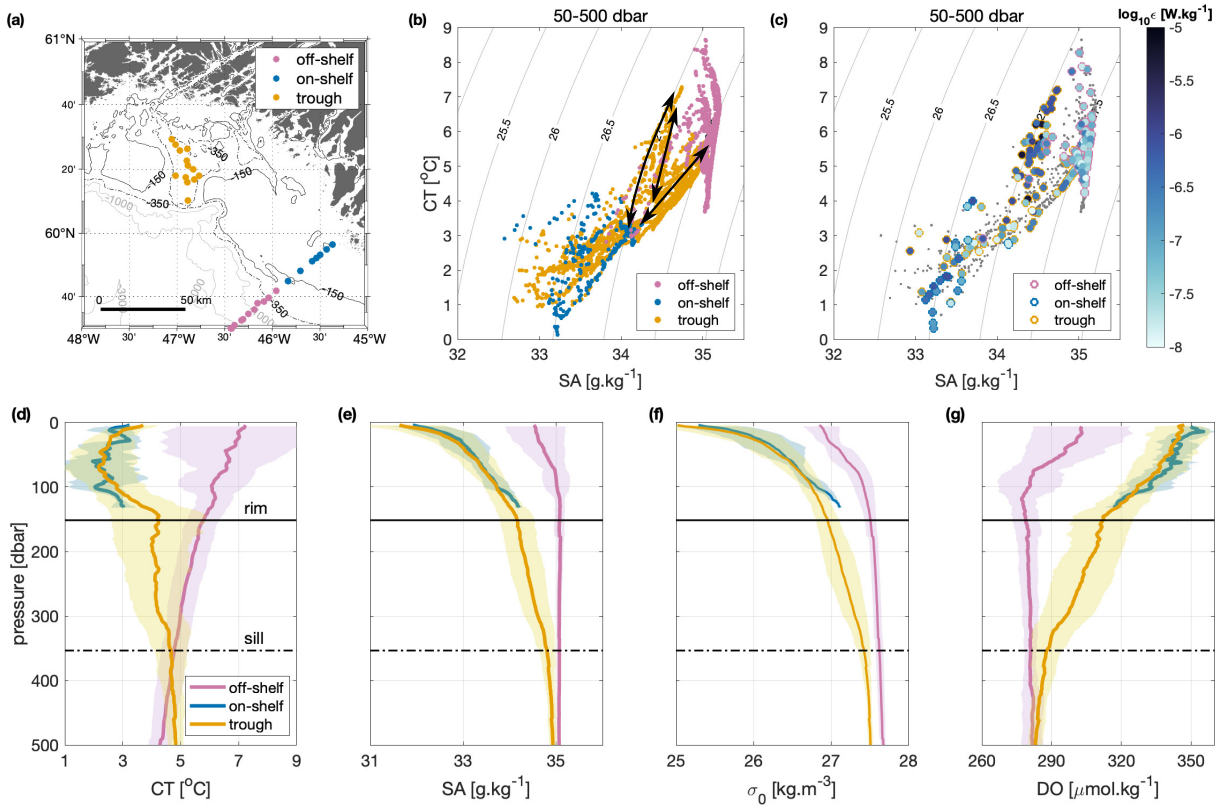

Figure 2.5. Comparison of water properties far upstream to inside the trough. (a) Map showing stations used in regional averages and subsequent panels; off-shelf (pink), on-shelf (blue), trough (orange). (b) T-S diagram comparing water properties by regions for the 50-500 dbar layer. (c) T-S diagram of all points in (b) coloured by dissipation rate for points with $\varepsilon > 10^{-8}$ W.kg^{-1}. Mean (d) conservative temperature, (e) absolute salinity, (f) potential density and (g) dissolved oxygen profiles; shading shows one standard deviation about the mean. Black arrows in (b) indicate mixing pathways.

property gradient below the sill depth is observed in the trough profiles (Figures 2.5d-2.5g), indicative of vertical mixing between the overlying layer and the deep waters trapped in the trough. This mixing could be explained by turbulence as waters spill over the sill (Venables et al., 2017) and velocity-shear from the secondary circulation at sill depth (Figure 2.6e).

Further, cross-trough asymmetry in sub-surface waters was observed in the trough, 18 km inshore of the mouth. A salty, oxygen-poor inflow on the upstream wall of the trough and a fresher, oxygen-enriched outflow on the downstream wall supports a cyclonic circulation between 150-250 m (Figures 3.3c and 2.6). Specifically, inflowing waters have oxygen concentrations

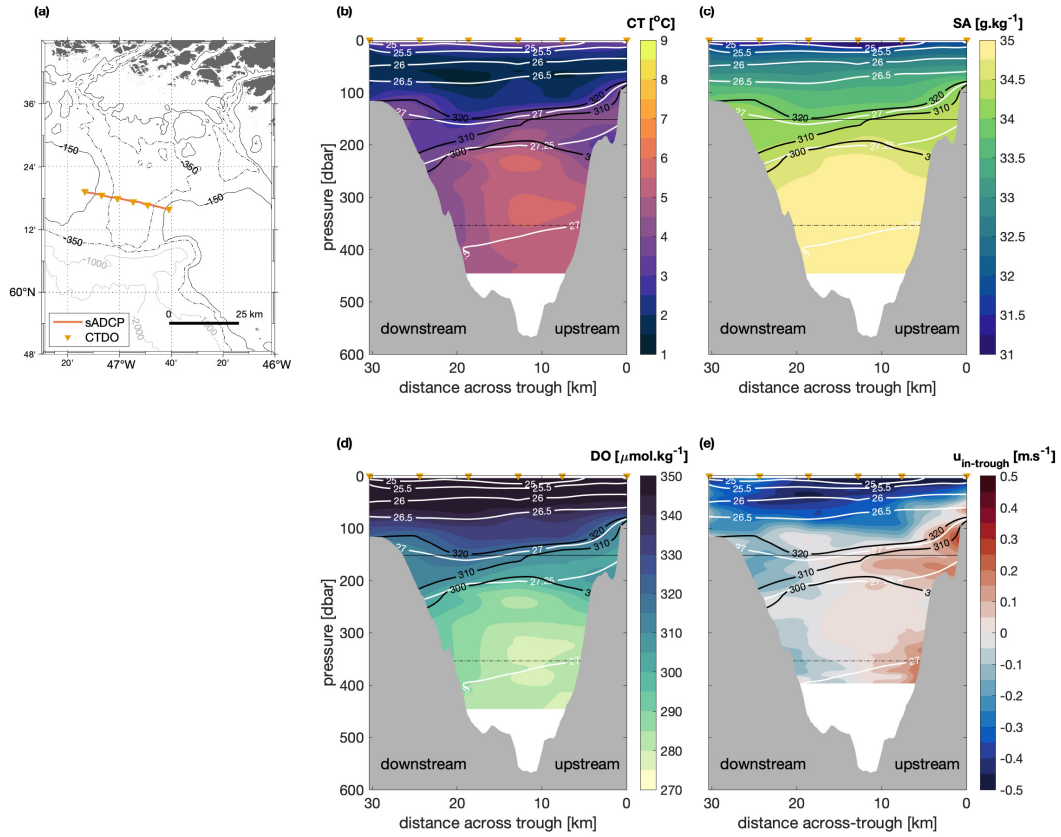

Figure 2.6. Cross-trough transect sections. (a) Map showing location of sADCP transect (orange line) and CTD stations (orange triangles). Cross-trough (b) conservative temperature, (c) absolute salinity, (d) dissolved oxygen, and (e) in-trough velocity (positive towards the coast) fields. In (b-e) isopycnals (white lines), rim depth (150 m, black line), sill depth (350 m, black dashed line), CTD stations (orange triangles), and the 300, 310, and 320 μmol.kg^{-1} oxygen contours (thick black lines) are overlain. Bathymetry in (b-e) is from the shipboard multibeam sonar.

of between 300-310 μmol.kg^{-1}, compared to concentrations of 310-320 μmol.kg^{-1} in the outflowing waters (Figures 2.6d and 2.6e). While a similar cross-trough gradient is seen in salinity, the asymmetry is not as evident in temperature as the system is salinity-stratified with considerable temperature interleaving (Figures 2.6b and 2.6c). Even at depth in the trough, below the depth of the sill (350-450 m), a cyclonic circulation supports a small cross-trough salinity gradient (Figures 3.3d and 2.6e), which is striking given the sill blocks free exchange with off-shelf waters.

Table 2.2. Column-integrated volume, heat, freshwater, and oxygen transport in the 150-350 m layer (between the trough rim and sill) as calculated from the cross-trunk transect.

	Inflow	Outflow
Volume transport [mSv]	97	96
Heat transport [PW]	0.106	0.105
Fresh water transport [mSv]	1.3	1.8
Oxygen transport [$\times 10^4$ mol.s^{-1}]	2.95	2.99

The sub-surface cyclonic circulation can be described as a horizontal exchange flow, with a volume transport of 97 mSv, symmetric about the axis of the trough (Table 2.2, Figure 2.6). Despite the symmetric volume transport, the cross-trough gradient in salinity and oxygen results in greater freshwater and oxygen transports out of the trough than in; indicative of AW mixing with PW in the trough (Table 2.2, Figure 2.6). The residence time for waters in the trough between the rim and sill is given by $t_R = \frac{Vol}{T_{ex}}$. Vol is the volume of interest within the trough, assumed to be the area of the main trunk of the trough over the 150-350 m layer, such that $Vol = 2.4 \times 10^{11}$ m^3. Using the exchange flow as the volume transport, T_{ex}, the residence time for waters between the rim and sill is estimated to be 30 days.

The unique in-trough environment is connected to Ikersuaq fjord via the northwest branch of Narsaq Trough. In general, surface waters become colder, fresher, and more oxygen-rich towards the fjord, although surface waters in the fjord are warmer than in the northwest branch (Figure 2.7c-2.7e, 0-100 dbar). A similar general signal is seen at mid-depth, with a stronger horizontal gradient in water properties between the trunk of the trough and the northwest branch than between the northwest branch and the fjord (Figure 2.7c-2.7e, 150-350 dbar). This is in part due to the pocket of warm, salty, oxygen-poor water on the upstream wall, associated with inflowing waters from the shelf-break (Figure 2.7c-2.7e, x $>$ 40 km). Below 350 dbar, AW was observed along the length of the northwest branch and inside the fjord with little horizontal gradient in water properties. We note, however, that the transect track does not trace the expected pathway of waters entering the northwest branch. The trough-fjord connectivity is discussed in Section 2.5.2.

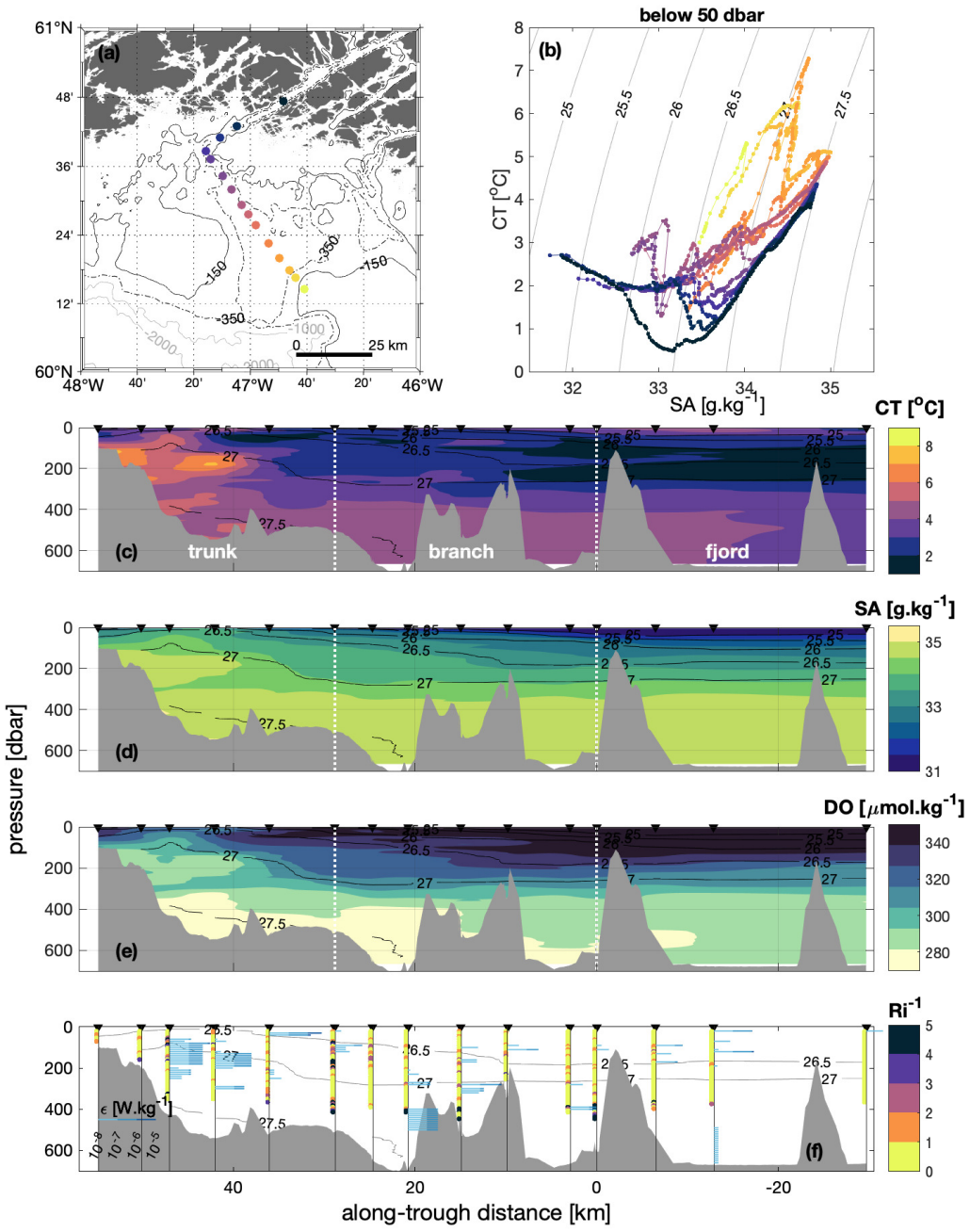

Figure 2.7. Inner-midstream transect entering Ikersuaq fjord. (a) Map of CTD stations, coloured by location. (b) T-S diagram, coloured by location as in (a). (c-e) As in Figure 2.3, but for the inner-midstream transect; dashed white lines indicate the CTD stations used to delineate the trunk of the trough, northwest branch, and fjord. (f) Estimated dissipation rates (ε, blue bars) with inverse Richardson number estimates (Ri^{-1}, coloured dots) overlain.

2.4.3 Estimates of Turbulent Dissipation Rate and Diapycnal Mixing

Using the Thorpe scale analysis described in Section 2.3.5, we find that turbulent dissipation rates, ε, (and subsequently diffusivities, κ_z) are elevated in the trough (Figure 2.5c and 2.7f). Notably, ε values of up to 10^{-5} W.kg^{-1} are observed in the trough, which is three orders of magnitude higher than in an Antarctic trough (Scott et al., 2021) and two orders of magnitude higher than on the continental shelf in Svalbard (Fer, 2006) or mixing hot spots on the United States continental slope (Nash, Alford, Kunze, Martini, & Kelly, 2007). Dissipation rates upstream of the trough are also high (10^{-6} W.kg^{-1}; Figure 2.5c). In particular, elevated dissipation is seen where pockets of warm, salty, oxygen-rich AW exist in the trough, likely mixing the AW with PW (e.g. Figure 2.7 at 100-300 m depth, 40-50 km along-trough). We note that high ε values are also observed at depth in the trough near steep topography, but there is no PW at this depth to create the modified-AW. Estimating the vertical diffusivity in the trough over the 150-350 dbar layer using $\kappa_z = \gamma\varepsilon/N^2$ (Section 2.3.5), we find $10^{-5} < \kappa_z < 10^{-1}$ m^2.s^{-1}, with $\bar{\kappa}_z = 10^{-3}$ m^2.s^{-1}. This mean diffusivity is an order of magnitude higher than typically reported for Antarctic troughs (Klinck (1998); diffusivity estimated from a semi-spectral primitive equation model), or in Arctic fjords and on the Greenland shelf (Fer (2006); Bendtsen, Rysgaard, Carlson, Meire, and Sejr (2021); diffusivities estimated from microstructure measurements).

One way for vertical dissipation to be enhanced is through shear-driven mixing which can be identified using the Richardson number. The Richardson number is defined as $\mathrm{Ri} = \frac{N^2}{Sh^2}$, where *Sh* is the vertical shear in the two-dimensional velocity field (L. Howard, 1961; Miles, 1961). Typically, vertical velocity shear is deemed strong enough to overcome vertical stratification and drive mixing at Ri$<$1/4, however, due to the 8 m resolution of the sADCP data, we use a more relaxed threshold of $\mathrm{Ri} < 1$ ($\mathrm{Ri}^{-1} > 1$; MacKinnon et al., 2021). In several sections, sub-critical Ri values are observed between 100-200 dbar, i.e. at the rim depth (e.g. Figure 2.7f), co-located with where the surface PW meets the subsurface AW circulation (Figure 2.6). This indicates that the mixing creating the modified AW in the trough is due, at least in part, to shear-driven

instabilities.

To assess whether it is possible for the sub-surface cross-trough salinity and oxygen gradient to be created through turbulent vertical mixing processes within the trough, rather than variability in the properties of the inflowing water, we use a simple advection-diffusion model (Section 2.3.5). A vertical spreading scale of $\lambda = 150$ m is found to be sufficient to modify the inflow properties to the match outflow properties. Taking t_c as the 30 day residence time calculated in Section 2.4.2, the vertical diffusivity needed to drive this modification is estimated to be 10^{-2} m^2.s^{-1}. While this κ_z is within the range of values measured in the trough, it is above the mean ($\bar{\kappa_z} = 10^{-3}$ m^2.s^{-1}), such that advection may play a role. Additionally, we note that any cold, fresh, oxygen-rich sub-surface waters exiting the fjord may contribute additional source water to the modified layer, reducing the vertical mixing needed as estimated using this model. However, we expect the submarine meltwater (or meteoric water) transport to the shelf from local glaciers will be orders of magnitude smaller than the transport of the WGCC (< 5 mSv, (Beaird, Straneo, Le Bras, Pickart, & Jenkins, 2023) versus $\sim$800 mSv, (Foukal & Pickart, 2023)).

2.5 Discussion

2.5.1 Cross-Shelf Exchange and Water Mass Modification

Transport of AW into Narsaq Trough is likely due to bathymetric steering of mean flow and eddies - indications of which were observed during the survey and which are illustrated in Figure 2.8. We propose that AW transported into the trough is then mixed with the overlying PW and any water escaping the fjord below the surface, primarily through shear-driven mixing and likely supported by trough-induced downwelling and vortex stretching. These processes are discussed below.

The exchange flow in the trunk of the trough (Figure 2.6e) can be characterised as a bathymetrically-steered leakage from the WGC (Figure 2.8b). Based on canyon theory, we

expect that when the leakage is steered into the trough along the upstream wall it is downwelled, with upwelling occurring on the downstream wall (Klinck, 1996; Freeland & Denman, 1982). Klinck (1996) suggested that when dissipation is strong, as is the case here (Figure 2.5c and 2.7f), upwelling on the downstream wall is reduced (assuming diapycnal mixing), resulting in net downwelling in the trough.

A low Rossby number, *Ro*, indicates that sub-surface flow is likely to follow isobaths and circulate around the canyon (Allen & Hickey, 2010; Spurgin & Allen, 2014). The *Ro* is defined as $Ro = U/fr$, where U is the upstream flow speed at the depth of the trough rim, f is the Coriolis frequency, and r is the radius of curvature of the upstream isobaths as they bend into the trough (Allen & Hickey, 2010). For Narsaq Trough, *Ro* is estimated to be 0.12 ($U = 0.3$ m.s^{-1}, Figure 2.3e, at 150 m depth, 60 km offshore; $r = 20$ km following the large-scale bathymetry), which is low ($Ro < 0.2$, Spurgin & Allen, 2014). The sub-surface circulation observed at Narsaq Trough (Figure 2.6e) is therefore consistent with theory. Since the strength and location of the WGC core is variable (Foukal & Pickart, 2023), the flow upstream of the trough may at times be too fast to follow isobaths, such that the exchange flow within the trough is likely episodic. Further, the bathymetry just upstream of the trough makes a sharp bend, which exacerbates the likelihood that flow will separate from the bathymetry.

The warm, salty, oxygen-rich pulse of water observed at the head of the trough has the appearance of an eddy (Figures 2.3g-2.3i, circled in white; illustrated in Figure 2.8b). These anomalous water properties are co-located with a reversal in the along-shelf velocity, further supporting the eddy hypothesis (Figure 2.3j). Based on the along-shelf velocity, the eddy-like feature can be characterised as cyclonic, with a radius of 5 km. Studies in Antarctica have shown that eddies preferentially cross the shelf-break at troughs and account for up to 50% of on-shelf heat transport at troughs (Couto et al., 2017; Martinson & McKee, 2012). As such, eddies entering troughs are likely also a major source of heat and AW to the Greenland shelf. These eddies could be generated by Rossby waves propagating along the shelf-break (St-Laurent et al., 2013).

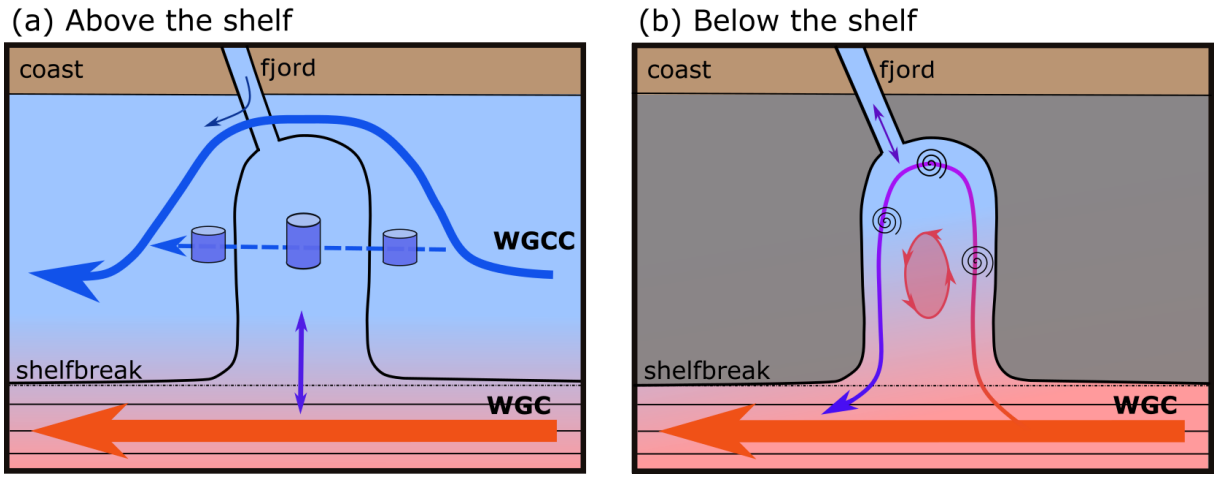

Figure 2.8. Schematic illustrating flow-field, cross-shelf exchange mechanisms, and modification of AW (a) above the shelf (0-150 m) and (b) below the shelf, between the trough rim and sill (150-350 m). Blue shading indicates PW, red shading indicates AW. Arrows show the two main currents (WGC, red; WGCC, blue), surface flow reversals over the trough ((a) purple), fjord outflow ((a) dark blue), exchange flow ((b) red-to-purple), sub-surface fjord exchange ((b) purple), and an eddy ((b) pink). In (a) cylinders represent vortex tubes and in (b) spirals indicate mixing and modification of AW.

Once the AW is advected on-shelf, either by bathymetric steering of the mean flow or by eddies, it is proposed that the AW is modified by shear-driven mixing in the trough (Figure 2.8b). Strong vertical shear in the velocity field is observed in the trough, in part due to a reversal of the surface flow between the two transects (Figures 2.7f and 2.6e, 100-200 m, and illustrated in Figure 2.8b). The high shear is co-located with depths of high dissipation (Figure 2.7f), suggesting velocity shear is likely driving vertical fluxes. Brearley et al. (2017) show that velocity shear resulting from wind-driven currents is a key source of vertical mixing between overlying water masses on the Antarctic Peninsula, however, the surface flow reversal observed here cannot easily be explained by local wind forcing as the local wind forcing was weak during both transects (Table 2.1, Figure 2.11). In addition to shear-driven mixing, any PW not able to follow isobaths upon encountering the trough will experience vortex stretching as water parcels transit into deeper water, bringing PW into contact with AW and supporting mixing (Figure 2.8a).

While we have presented some evidence of trough modified waters exported downstream

(Section 2.4.1, Figures 2.3 and 2.4), we cannot rule out that some of the upstream/downstream differences are due to WGC variability (Foukal & Pickart, 2023). A comparison of freshwater and oxygen transport differences from upstream to downstream did not lead to conclusive results, which we attribute, in part, to differing wind conditions (weak vs. strong upwelling; Table 2.1; Figure 2.11). Understanding the impact of Greenland's troughs to transporting the freshwater and oxygen offshore will require further studies that can estimate long-term means (Luo et al., 2016; Hendry et al., 2021; Schiller-Weiss et al., 2024).

2.5.2 Implications for Fjords and Marine-Terminating Glaciers

Previous studies in Antarctica have shown that troughs drive an onshore heat flux, contributing to the melting of ice shelves (Silvano et al., 2022; Moffat & Meredith, 2018; Couto et al., 2017). Here we show that AW is modified in the trough (Figure 2.5), such that any AW that makes it into the adjoining Ikersuaq fjord is colder than unmodified AW (and has higher oxygen), consistent with Klinck (1998). The deepest isobath connecting the fjord and trough sets the level at which waters can be freely exchanged between the two. For Narsaq Trough and Ikersuaq fjord, existing estimates of this depth vary: 185 m (BedMachine, Morlighem et al., 2017), 330 m (Mortensen et al., 2020), 200-400 m (Nørgaard-Pedersen & Mikkelsen, 2009), or more than 400 m (Ribergaard, 2007). Our multibeam survey showed a series of sills, reaching 100 m at the shallowest point (Figures 2.7c-2.7f), but we could not determine the deepest connected isobath from our survey. However, the water properties inside the trough and fjord between the 150-350 dbar are very similar (Figures 2.7 and 2.12), consistent with a deep connection. It is likely that additional mixing occurs as waters spill over the series of sills into the fjord, which will further reduce the temperature of the water mass where the sills are shallow enough to drive mixing between PW and AW (Venables et al., 2017).

2.5.3 Implications for Biological Productivity

The Greenland continental shelves are known to be biologically productive, especially in the south (Vernet et al., 2021; Krawczyk et al., 2021), but the effect of troughs on this productivity has not been studied. In the summer, productivity on the shelf is thought to be nitrate-limited (Hopwood et al., 2018), which would be alleviated if troughs delivered nutrient-rich water to the euphotic zone. However, Narsaq Trough likely supports net downwelling and elevated nutrient concentrations are not seen over the trough.

Observations in Narsaq Trough do, however, show that macronutrients are depleted at depth, relative to waters at the same depth off-shelf and far upstream (Figures 2.4b-2.4d, 2.4g-2.4i). These observations are consistent with the dynamical explanation that vertical mixing, likely through velocity shear and supported by downwelling and vortex stretching, results in exchange between the nutrient-poor PW and nutrient-rich AW. The absence of a signal of nutrients mixed up into the surface waters can be explained by the rapid replenishment of surface waters over the trough, whereas waters in the trough have a longer residence time, allowing for depletion/dilution.

We note that our observations of lower sub-surface nutrient concentrations in the trough than off-shelf differ from previous findings in Greenland. Hendry et al. (2019) show elevated sub-surface nutrient concentrations in Nuuk Trough compared with off-shelf, which they attribute to contributions from glacial discharge. Their observations were taken at a similar time of year (July-Aug, 2017), suggesting that the difference is not due to seasonal variability. One difference of note is that Nuuk Trough has a shallow retrograde slope along the length of the trough, whereas Narsaq Trough has a steep retrograde slope at the mouth before leveling out and rising again towards the head. The steeper sill at Narsaq Trough may be more conducive to driving mixing between AW and the overlying, nutrient-poor PW, thus reducing sub-surface nutrient concentrations.

2.6 Conclusions

Narsaq Trough, in southwest Greenland, is found to provide a pathway for AW to intrude onto the continental shelf where these waters are mixed with the overlying PW. As a result, subsurface waters in the trough are fresher, oxygen-enriched, macronutrient-depleted, and at times colder, relative to the unmodified AW offshore. For the AW that is transported into the connected fjord, mixing within the trough reduces the heat content of the waters that can access the outlet glaciers in Ikersuaq fjord. Additionally, the cyclonic circulation in the trough may export the modified AW back out onto the shelf-break and into the WGC. Export of the trough-modified waters could act to cool, freshen, and oxygenate the WGC, potentially increasing stratification and decreasing deep water formation in the adjacent convective basin. While there is a substantial body of literature documenting troughs driving heat and salt import onto continental shelves, particularly in Antarctica, few studies have considered the degree to which troughs modify inflowing water or drive export of shelf waters (although Venables et al., 2017 and Brearley et al., 2019 are two notable examples). As such, this work provides novel insights about the role of troughs in Greenland and shows that considering the cumulative effects of the numerous troughs around Greenland's margin warrants further investigation.

2.7 Acknowledgments

I gratefully acknowledge the U.S. National Science Foundation: this work was primarily supported by NSF OCE-1948482 (MN, FS, and DT) with further support by NSF OCE-2023289 (SP), NSF OPP-2042692 (AW), and NSF OCE-1947970 (KF). We thank all the field teams (scientists, technicians and crew) that conducted the survey, with special thanks to Meg Yoder for the oxygen titrations. We thank Nick Foukal for providing the drifter trajectories, Gunnar Voet for the advection-diffusion model, and Ken Zhao for the Ikersuaq fjord sill estimate from BedMachine. Finally, we thank our two reviewers for their constructive, thoughtful, and prompt feedback.

This chapter is a full reprint of the material as it appears in AGU's Journal of Geophysical Research: Oceans as "Observations of water mass modification and cross-shelf exchange at Narsaq Trough, Greenland" by M. Nelson, F. Straneo, S. Purkey, A. Waterhouse, K. Fogaren, and D. Torres (2025). The dissertation author was the primary investigator and author of this paper.

2.A Appendix for Chapter 2

2.A.1 CTD Data Description

All CTD casts were initiated with a 10 m soak. The CTD package was then lowered at 1 m.s^{-1}, except for the first and last 100 m of each profile, when it was lowered at 0.5 m.s^{-1} (a Valeport 500 altimeter was used for bottom approaches). Data from CTD casts were cut to just the downcast, removing the initial soak and upcast. Salinity, calculated from temperature and conductivity as measured by the CTD, was despiked and calibrated against water samples collected on each cast and analysed at sea on an Autosal. The 24 Hz data was then binned onto a 2 dbar vertical pressure grid. The temperature sensor accuracy is $\pm$ 0.001 °C and the conductivity sensor accuracy is $\pm$ 0.0003 S/m. These data are available at Straneo (2023).

To produce the highest-quality CTD dissolved oxygen (DO) measurements, post-processing procedures were modeled after methods described in Uchida, Johnson, and McTaggart (2010). Briefly, over the entire AR69-03 cruise, of which the Narsaq Trough survey was a subset, 462 discrete water samples, commonly referred to as Winklers, were measured for DO. The discrete water sample dataset was provided by Palevsky, Yoder, Nicholson, and Fogaren (2024). The Winklers were used to optimize calibration coefficients in the Seabird-provided oxygen calibration equation (SBE Application Note 64-2) using a non-linear least square fit between CTD-DO values and Winklers. Residuals between Winklers and CTD-DO as a function of pressure, station number, temperature, and concentration were minimized after arranging casts into seven groups before determining optimized calibration coefficients. Final oxygen

concentrations were then determined using Winkler-optimized calibration coefficients, CTD-DO data processed using the default Sea-Bird hysteresis correction (Edwards, Murphy, Janzen, & Larson, 2010), a oxygen sensor time lag correction of 5 seconds, and bottle-calibrated salinity values. Additional details of processing and calibration procedures along with the calibrated DO data are available at Fogaren and Palevsky (2024).

2.A.2 Nutrient Data Description

Water samples for nutrient analysis (nitrate, nitrite, silicate, and phosphate) were collected at roughly every second station (49 stations in total). Sampling depths were chosen based on the downcast at each station targeting the surface, fluorescence maximum, local oxygen maxima and minima, distinct water masses, and bottom. Samples were filtered into 20mL plastic scintillation vials using Whatman .45 μm pp filters as soon as possible after collection from the rosette (within 30 minutes) before being frozen in a -80 °C freezer until processing. Duplicate samples were taken from the same Niskin at 17 locations, at a variety of depths, to assess the measurement error.

Samples were analyzed by the Ocean Data Facility at Scripps Institution of Oceanography on a Seal Analytical continuous-flow AutoAnalyzer 3 (AA3). After each run, the charts are reviewed for any problems and final concentrations are calculated using SEAL Analytical AACE 6.07 software. The analytical methods used are described by Gordon, Jennings, Ross, and Krest (1993); Atlas, Hager, Gordon, and Park (1971). These data are published by Straneo (2023).

Note that ammonium concentrations where also measured using these samples, but these data were unreliable and so are not presented here.

2.A.3 Shipboard ADCP Data Description

Shipboard ADCP (sADCP) data were collected with a Teledyne RDI 150 kHz Ocean Surveyor ADCP (OS150). The OS150 was setup as follows: narrowband mode, 55 bins, 8.0 m bin-size, 6.0 m blank, 8.0 m pulse. Data were acquired using the University of Hawaii Data

Acquisition System (UHDAS). The data acquisition system provides communication with the ADCPs to set parameters and to start pinging and acquiring data. UHDAS collects binary ADCP records, NMEA GPS data, gyro heading data, and POSMV heading correction data, properly parses and timestamps each, and stages data for further processing using Common Ocean Data Access System (CODAS) database modules (Firing & Gordon, 1990; Firing & Hummon, 2010). CODAS processing is a suite of programs which convert raw single ping, ship referenced ADCP data into averaged absolute velocity profiles on a 5 minute sample interval. A series of steps were performed to eliminate bad values (mostly from acoustic interference), calculate and apply a calibration to correct for transducer misalignment, and rotate data into earth coordinates. The velocity profiles were then detided using the Greenland 1 km barotropic tidal model (Gr1kmTM) from Earth and Space Research institute (S. L. Howard & Padman, 2021). Oregon State University Tidal Prediction Software (OTPS) was used to extract tidal information from the model (Egbert & Erofeeva, 2002). Bathymetry used in the model comes from GEBCO 2020 Grid which is a global terrain model with 15 arc-second resolution (GEBCO Compilation Group, 2020). The resulting uncertainty in the velocity data, due to instrument and tidal model errors, is estimated to be 0.02–0.03 $m.s^{-1}$. These data are published by Straneo (2022).

2.A.4 Along-Track Bathymetry Data Description

An along-track bottom depth product was created from the shipboard multibeam echo sounder (Kongsberg EM122 and Kongsberg EM710). The center beam depths from the two multibeams were combined (EM710 in shallow water, EM122 in deeper water) using the Qimera software to give a single product with 50 m horizontal resolution. Noisy data were then manually removed by identifying points when the difference between one data point and the next was unreasonably large. For cases where many data points had to be removed, the bottom depth is estimated by linearly interpolating between the gap.

Additionally, for the cross-shelf sections, the bottom depth between the coastal end of the transect and the coastline was estimated from BedMachine (Morlighem et al., 2017). Bottom

depths were extracted from the bathymetry product by querying depths at locations determined by extending each transect to the coast.

2.A.5 Wind Reanalysis Data

Surface wind stress, in the month leading up to and during the survey, is used to determine the local and remote wind forcing on waters near Narsaq Trough. We use the 10 meter winds and pre-calculated and corrected wind stress from the Global Ocean Hourly Reprocessed Sea Surface Wind and Stress from Scatterometer and Model dataset, which has 1/8° resolution (Copernicus Marine Service, 2024). The reprocessed dataset is used over the more common ERA5 dataset as the wind stress is pre-calculated, avoiding complications around what drag coefficients to use. This is especially consequential in the study region as the winds are known to reach the highest wind stresses.

A time-series of local wind stress is produced by averaging wind stress over Narsaq Trough (defined by 60.5 °N, -48.75°E; 60.75°N, -47.75°E; 60 °N, -45 °E; 59.5 °N, -46 °E; Figure S3 dark blue). A time-series of remote wind stress is produced by averaging wind stress over the southeast Greenland continental shelf (defined by 60 °N, -43.25 °E; 62 °N, -42 °E; 62 °N, -40.75 °E; 60 °N, -42 °E; Figure 2.11 light blue). Wind stress in each region is rotated into along-shelf and cross-shelf components (positive along-shelf is 138° counter-clockwise from East for local winds, and 255° counter-clockwise from East for remote winds), such that positive along-shelf wind stress is downwelling-favorable in both locations.

2.A.6 Trough budget calculations

Using the exchange flow transports in Table 1 and the vertical diffusion estimates in Section 2.4.3, an attempt is made to close heat, freshwater, and oxygen budgets over the 150-350 m layer (trough rim to sill) inside Narsaq Trough. Couto et al. (2017) give the volume-averaged

heat budget for a trough as

$$\Phi_H - \rho_0 c_p \left(\frac{\kappa_z}{H} \frac{\partial T}{\partial z} + \frac{\kappa_x}{L} \frac{\partial T}{\partial x} \right) = \rho c_p \frac{dT}{dt} \tag{2.7}$$

where Φ_H is the lateral heat transport across the mouth of the trough, the second term is the vertical diapycnal diffusion up out of the trough, the third term is the lateral diffusion across the head of the trough, and the final term is the warming the water in the trough experiences.

At Narsaq Trough there is an exchange flow across the mouth, such that there is a lateral transport in, Φ_{in}, and out, Φ_{out} (Figure 2.13). It is assumed that there is no lateral diffusion across the head of the trough as the 150-350 m layer is confined within the trough, such that the head is a solid boundary. Instead of considering the fourth term as the warming or cooling, here it is assumed that the residual is the error in the budget. Additionally, I assume there is no vertical diapycnal diffusion into the box on the bottom boundary (at 350 m) as $\partial T/\partial z \approx 0$. Finally, multiplying by volume to get the total budget, I am left with

$$\Phi_{H,in} - \Phi_{H,out} - \rho_0 c_p A \kappa_z \frac{\partial T}{\partial z} = R_H \tag{2.8}$$

where $\rho_0 = 1027$ kg.m^{-3}, $c_p = 3850$ J.K^{-1}.kg^{-1}, A is the area of the 150-350 m layer inside the trough (960 km^2), κ_z is the vertical diffusivity, $\partial T/\partial z$ is the vertical temperature gradient, and R_H is the residual. A bulk κ_z value is used that is the average κ_z over the 100-200 m layer for all profiles in the main trunk of the trough (see Figure 2.5a, orange dots). The 100-200 m layer is chosen as that depth-range spans the interface between the in-trough box and the PW layer at the surface (Figure 2.13). Similarly, I calculate the vertical diapycnal diffusion using the vertical temperature gradient each 2 dbar level over the 100-200 m layer at each profile in the trunk of the trough. Averaging these diffusion estimates over all depths and profiles gives a mean and standard deviation for the vertical flux ("flux up") term.

Similar equations to Eq. (2.8) can be written for the freshwater and oxygen budgets.

Table 2.3. Heat, freshwater, and oxygen budget terms for box budget over the 150-350 m layer (i.e. between the trough rim and the depth of the sill at the mouth).

	Flux in	Flux out	Flux up (Thorpe[a])	Residual (Thorpe[a])	Flux up (Voet[b])	Residual (Voet[b])
Heat [PW]	0.106	0.105	$(2\pm8)\times10^{-4}$	0.01	$(5\pm20)\times10^{-4}$	0.01
Fresh water [mSv]	1.3	1.8	-0.7 ± 0.9	0.2	-1.6 ± 2.3	1.1
Oxygen [$\times10^4$ mol.s^{-1}]	2.95	2.99	-0.07 ± 0.2	0.03	-0.2 ± 0.4	0.1

[a] using $\kappa_z = 4\times10^{-3}$ m^2.s^{-1}
[b] using $\kappa_z = 1\times10^{-2}$ m^2.s^{-1}

First, the freshwater budget is given by

$$\Phi_{FW,in} - \Phi_{FW,out} - A\kappa_z \frac{\partial}{\partial z}\left(\frac{S_{ref}-S}{S}\right) = R_{FW} \tag{2.9}$$

where $S_{ref} = 35.1$ g.kg^{-1} is the reference salinity chosen to match the salinity of the 150-350 m layer on the shelf-break upstream of the trough, and S is the in situ salinity. Second, the dissolved oxygen budget is

$$\Phi_{DO,in} - \Phi_{DO,out} - \rho_0 A\kappa_z \frac{\partial DO}{\partial z} = R_{DO} \tag{2.10}$$

where DO is the dissolved oxygen concentration.

In addition to attempting to close these budgets with the mean κ_z estimated from the 100-200 m, I calculate the terms using the vertical diffusivity needed as found by the Voet advection-diffusion model, $\kappa_z = 10^{-2}$ (see Section 2.3.5). All terms are shown in Table 2.3.

2.A.7 Trough budget results

While the mean vertical fluxes estimated here are all in the direction that helps to close the heat, freshwater, and oxygen budgets, the standard deviations from the mean vertical flux encompass zero for all estimates (Table 2.3). As such, it cannot be said with statistical significance that the vertical fluxes estimated here close the heat, freshwater, or oxygen budgets. Below, the heat, freshwater, and oxygen budgets are discussed in turn.

For the heat budget, the inflow and outflow balance to within 1%, with no vertical flux

needed to close the budget. Both the measured ("Thorpe") and the modeled ("Voet") vertical fluxes are an order of magnitude less then the residual, such that the vertical flux does not determine the heat balance to first order.

For the freshwater budget, there is greater flux out of the trough than in, such that a vertical freshwater flux is needed to close the budget. Using observations of vertical mixing, I estimate an upward freshwater flux of -0.7 ± 0.9 mSV, i.e. a downward flux of freshwater of 0.7 ± 0.9 mSV, helping to close the budget (residual of 0.2 mSv). However, when using the higher vertical diffusivity from the Voet model, too much freshwater is mixed down, resulting in a larger residual (1.1 mSv).

Lastly, the oxygen budget is also largely balanced by the horizontal circulation. The vertical oxygen flux estimated from both Thorpe scale analysis and the Voet advection-diffusion model help to close the budget. However, the larger vertical flux estimate based on the Voet model results in a larger residual ($R_{thorpe} = 0.03 \times 10^4$ mol.s^{-1}, $R_{voet} = 0.1 \times 10^4$ mol.s^{-1}).

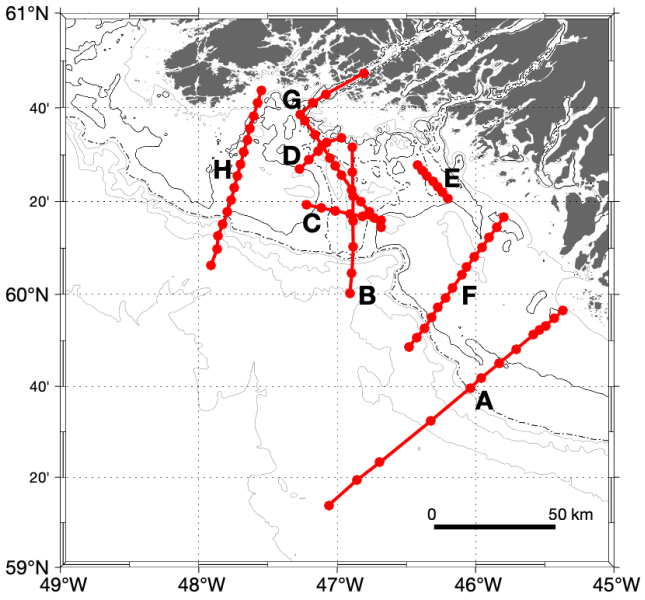

Figure 2.9. Narsaq Trough survey transect locations and labels. Filled red circles denote CTD station locations.

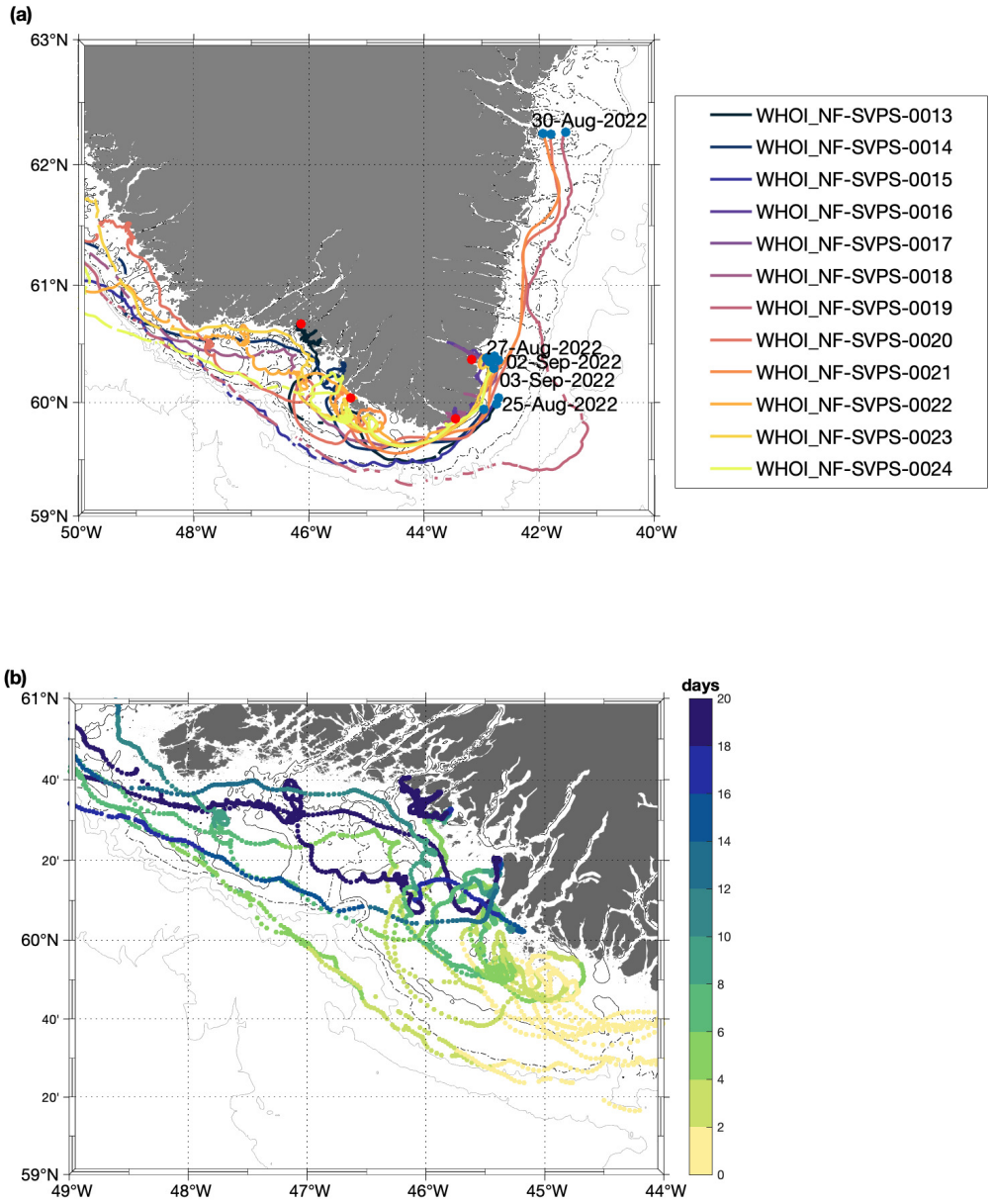

Figure 2.10. Drifter information. (a) Drifter trajectories coloured by drifter, with locations of deployments (blue dots) and groundings (red dots) overlain. Deployment dates are also marked. (b) Drifter trajectories coloured by time in days for drifters to travel over the trough. Time is counted from when each drifter first crosses the -44 °E meridian. For (a) and (b) isobaths marking the trough rim (black, solid), the depth of the sill (black, dashed), and -1000, -2000, -3000 m (grey) are shown.

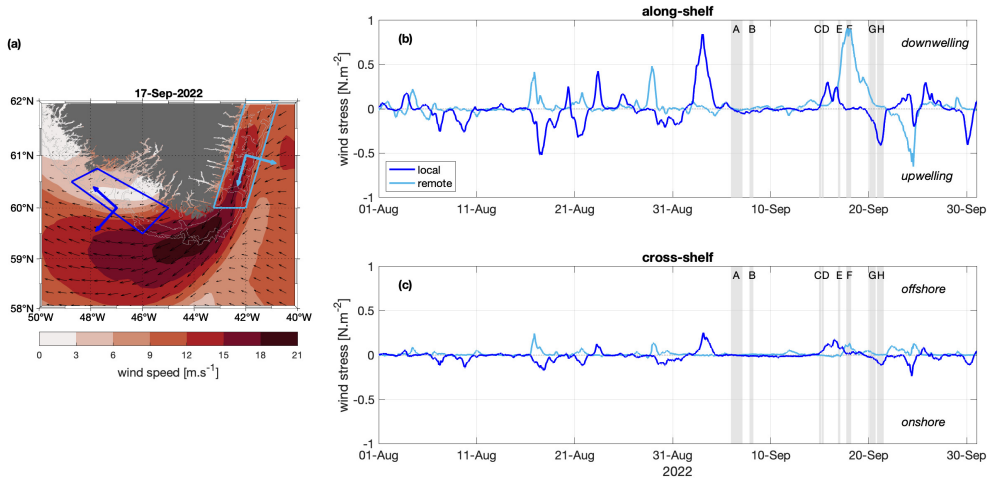

Figure 2.11. Local and remote wind stress in the month leading up to, and during, the survey. (a) Wind speed (contoured) and direction (black vectors) at a single time step in southern Greenland. Boxes indicate areas over which local (dark blue) and remote (light blue) wind stress averages were calculated. Coloured vectors originating from each box show the orientation of the positive along- and cross-shelf wind stress. (b) Along-shelf and (c) cross-shelf wind stress averages for the local (dark blue) and remote (light blue) regions. Grey shading indicates when survey transects were occupied. For (b) positive wind stress is downwelling-favourable; for (c) positive wind stress is offshore wind. Transects are labeled A-H as in Table 1 and Figure 2.9.

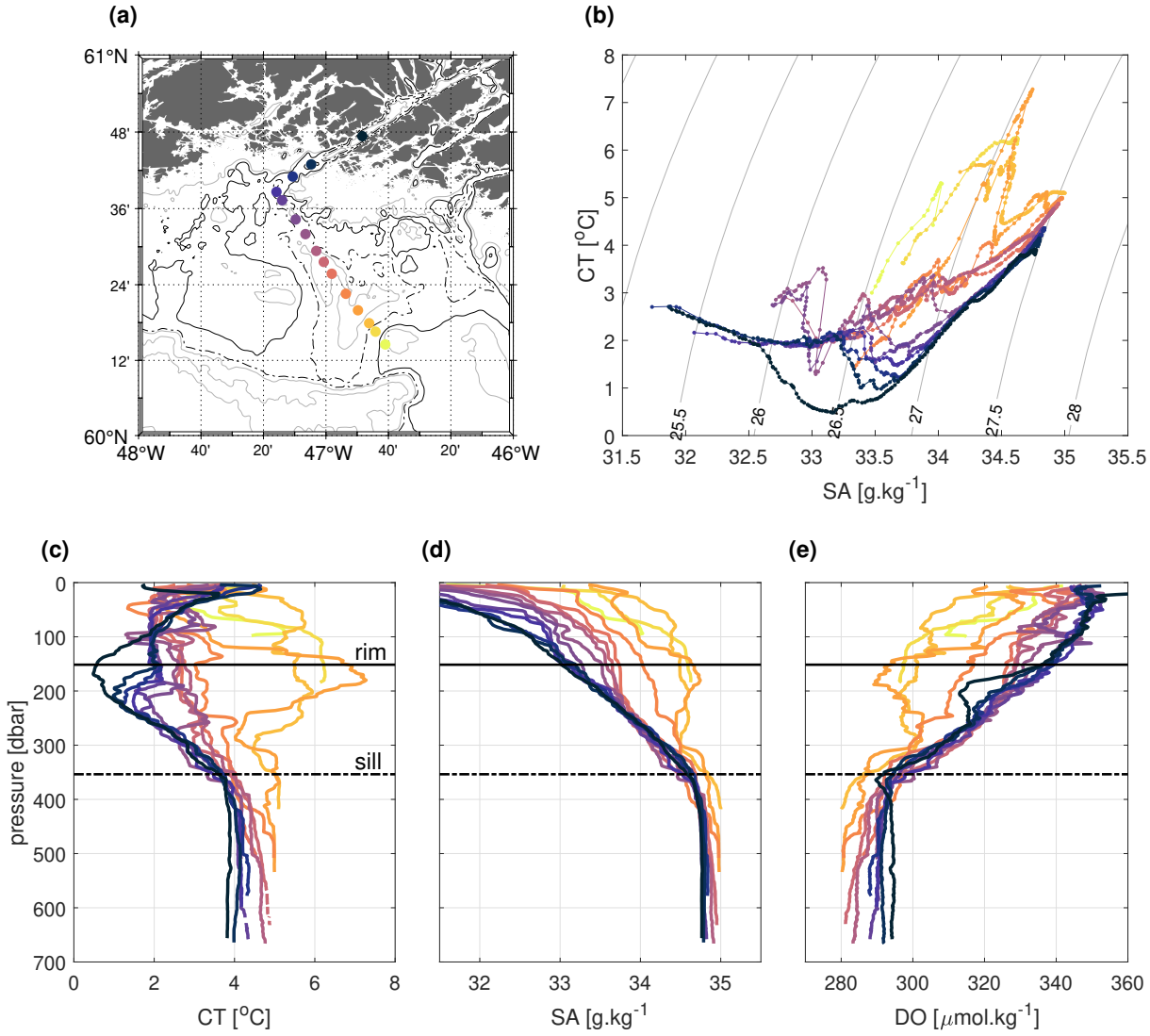

Figure 2.12. Evolution of water properties from the main trunk, through the northwest branch, and into the fjord. (a) Map of CTD stations, coloured by location. Isobaths marking the trough rim (black, solid), the depth of the sill at the mouth (black, dashed), and -100, -500, -1000, -2000 m (grey) are shown. (b) T-S diagram of profiles along the inner trough section. (c) Conservative temperature, (d) absolute salinity, and (e) dissolved oxygen profiles at stations along the transect. Pressures corresponding to the depth of the trough rim (black, solid) and sill at the trough mouth (black, dashed) are overlain. Colouring in (b-e) is by the station location, as in (a).

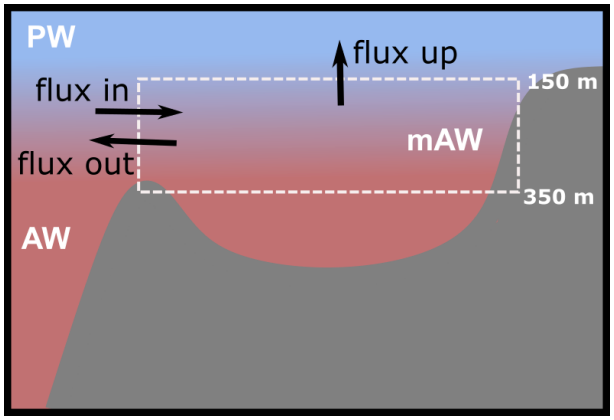

Figure 2.13. Schematic of box budget terms. The white box indicates the bounds of the box budget; black arrows indicate fluxes. "flux in" is Φ_{in}, "flux out" is Φ_{out}, and "flux up" is the vertical flux term based on the diffusivity estimates.

Chapter 3

Persistence of cross-shelf exchange at Narsaq Trough, Greenland, observed from voluntary observing ships

Abstract

Exchange of waters across the continental shelf-break in Greenland drives onshore transport of heat towards Greenland's coastal margins and the many outlet glaciers of the ice sheet, and offshore transport of freshwater into the convective basins in the subpolar North Atlantic. In Greenland, a handful of studies have shown instances of cross-shelf exchange being enhanced by troughs (deep grooves in the bathymetry that cut across the continental shelf from the coast to the shelf-break), but few observational campaigns have undertaken long-term studies in trough environments to assess time-mean conditions and drivers of temporal variability. Here we use 20 years of underway sea surface salinity and temperature observations and 8 years of ocean velocity profiles from cargo vessels transiting over Narsaq Trough, in southwest Greenland, to characterise the mean flow-field and water properties at the trough and investigate the temporal variability. A persistent cross-shelf exchange flow is observed both above and below the shelf at the trough, co-located with surface waters that are warmer and saltier than waters up- and down-stream, suggesting that the trough routinely advects Atlantic Water onto the continental shelf. Some instances of anomalously cold, fresh water over the trough are also observed, concurrent with offshore surface flow, suggesting the trough occasionally drives offshore transport of Polar Water. Troughs of a similar size and geometry around Greenland's continental shelf are thus likely important pathways for transporting heat towards the ice sheet and driving melt.

3.1 Introduction

At Greenland's continental shelf-break, coastal Polar Water (PW) abuts the Atlantic Water (AW) offshore. PW is cold, fresh, and oxygen-rich whereas AW is warm, salty, and oxygen-poor. As such, cross-shelf exchange can result in the transport of heat onshore, driving melting of land-ice with implications for sea level rise, and offshore transport of freshwater and oxygen, affecting open ocean stratification, deep convection, and subsurface oxygen reservoirs.

As summarised in Chapter 2, the troughs that cut across the continental shelves in Antarctica and Greenland help facilitate cross-shelf exchange, through bathymetry-flow interactions and by simply providing a deeper pathway for AW to access adjacent fjords underneath the lighter PW (Moffat & Meredith, 2018; Couto et al., 2017; Snow et al., 2023; St-Laurent et al., 2013).

Consistent with these studies, a summertime survey of Narsaq Trough, a large, branched trough in southwest Greenland, revealed a cyclonic circulation within the trough, below the shelf-depth (Chapter 2). This subsurface cyclonic circulation is associated with an exchange flow, transporting waters onshore on the upstream wall of the trough and offshore on the downstream wall of the trough. While the velocity structure of the exchange flow was symmetric about the axis of the trough, the water properties were not (Figure 2.6). Inflowing waters were warm, salty, and low in oxygen, characteristic of AW; whereas outflowing waters were cooler, fresher, and oxygen-enriched relative to the inflow. Within the trough subsurface water properties reflected mixing of the overlying PW and the inflowing AW, consistent with high levels of estimated vertical dissipation there (Figure 2.5). The conclusion drawn from the survey was that the bathymetry steers subsurface AW into the trough, where it is mixed with overlying PW and exported back off the continental shelf as modified AW. The trough, therefore, appears to support cross-shelf exchange and transformation of properties below the shelf-depth. During the survey the observed flow above the shelf was decoupled from the subsurface exchange flow, with offshore flow of PW over the entire width of the trough (Figure 2.6).

However, the ship-based survey only provides a snapshot in time of the flow-field, water mass distribution, and dynamics at Narsaq Trough, with no ability to assess the mean conditions or any temporal variability. Variability in the conditions at Narsaq Trough is expected as cross-shelf exchange at other troughs has been shown to vary on seasonal and shorter time-scales (Snow et al., 2021; Darelius, Dundas, Janout, & Tippenhauer, 2023; Ryan, Hattermann, Darelius, & Schröder, 2017; Sutherland & Cenedese, 2009). Specifically, at Sermilik Trough, in southeast Greenland, wind-reversals that drive reversals in the along-shelf flow result in onshore transport of AW, both at the surface over the trough and subsurface within the trough (Snow et al., 2023).

At Filchner Trough, in Antarctica, high winds enhance the ambient circulation on the shelf, increasing the onshore transport of the bathymetrically-steered flow into the trough (Dundas, Daae, & Darelius, 2024). Further, bathymetric steering of flow depends on flow speed, the width of the jet, and whether the jet is in contact with the bathymetry (Allen & Hickey, 2010). As the along-shelf currents at Narsaq Trough are known to be highly sensitive to local and remote wind-forcing, affecting the strength, width, and location of the current cores (Foukal & Pickart, 2023), it is hypothesized that winds play an important role in driving variability in cross-shelf exchange at Narsaq Trough too. Here we seek to understand whether the observed circulation in the trough and associated cross-shelf exchange is a persistent feature of the flow-field, analyse the surface-subsurface connectivity, and determine the driving forces of any temporal variability.

We use underway data from voluntary observing ships (cargo vessels outfitted with oceanographic sensors, also known as vessels of opportunity) transiting over Narsaq Trough, complemented by remote sensing from satellites, to monitor the water properties and flow-field at the trough over time. These datasets provide a unique opportunity to address the question of whether there is persistent cross-shelf exchange at Narsaq Trough. First, we describe the mean sea surface salinity and temperature over the trough and mean surface and subsurface flow-field. Second, we place results from a hydrographic survey in 2022 into the context of the mean conditions. Third, we assess the variability in the flow and water property fields. Fourth, we investigate whether wind forcing drives the temporal variability.

3.2 Data

3.2.1 NASA MUR GHRSST

The time-mean sea surface temperature (SST) over southern Greenland is computed from daily maps of SST from NASA's Group for High Resolution Sea Surface Temperature (GHRSST) Multiscale Ultrahigh Resolution (MUR), version 4, level 4 product. The SST product is created by gridding satellite SST observations onto a 0.01° grid using wavelets as basis functions in an

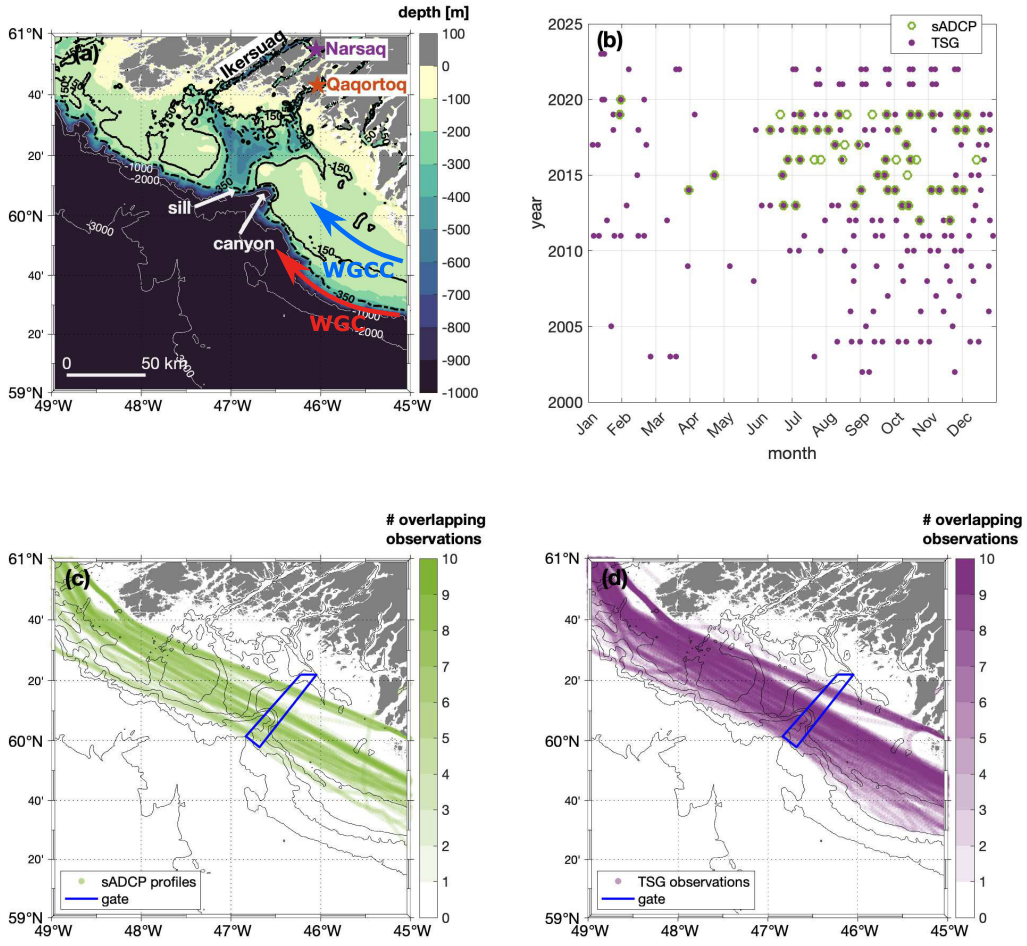

Figure 3.1. Maps of study region and data coverage. (a) Narsaq Trough bathymetry, showing location of sill at the mouth of the trough and the deep, steep canyon just upstream of the trough. The position and direction of the West Greenland Current (WGC, red arrow) and West Greenland Coastal Current (WGCC, blue arrow) are indicated, in addition to the locations of the towns of Narsaq and Qaqortoq and Ikersuaq fjord. The 150 m (black solid line), 350 m (black dashed line) and 1000, 2000, and 3000 m (white lines) isobaths are marked. (b) Temporal distribution of shipboard acoustic Doppler current profiler (sADCP, green) and thermosalinograph (TSG, purple) observations by year and fractional month. Spatial distribution of (c) sADCP observations over the 2012-2020 period and (d) TSG observations over the 2002-2023 period; darker colours indicate more overlapping observations. The gate through which a transit must pass to be included (bold blue box) and the 150, 350, 1000, 2000, and 3000 m isobaths (black lines) are shown.

optimal interpolation approach. The product is based upon nighttime skin (10-20 μm below the air-sea interface) and subskin (1-1.5 mm below the air-sea interface) SST observations from several instruments (GHRSST Science Team (2010), 2011). Here, we focus on the southern tip of Greenland (59 to 62 °N, -50 to -40 °E), from 2010-2023. Only grid cells that are flagged as "open ocean" (mask = 1) are used, all other points are not considered here. See JPL MUR MEaSUREs Project (2015) and Chin, Vazquez-Cuervo, and Armstrong (2017) for more details and data access.

3.2.2 SSS and SST from voluntary observing ships

For the 2002-2023 period, underway observations of sea surface salinity (SSS) and sea surface temperature (SST) were made from the *Nuka Arctica* (2002-2020) and *Tukuma Arctica* (2020-2023, replacing the *Nuka Arctica*). These are both cargo vessels operated by Royal Arctic Line of Denmark that service ports in Greenland, Iceland, and Denmark, regularly transiting over Narsaq Trough. The SST and SSS measurements were made using a thermosalinograph (TSG) from a sea water intake in the bow at approximately 2 m depth (Olsen, Brown, Chierici, Johannessen, & Neill, 2008). A measurement is reported every 1 or 5 minutes. These SSS and SST data were collected, validated, archived, and made freely available by the French Sea Surface Salinity Observation Service (`https://www.legos.omp.eu/sss/`) (Delcroix et al., 2002; Alory et al., 2015).

Here, only SSS observations that are flagged as "good" or "probably good" are used. SST observations are not quality controlled independently as it is expected that the temperature sensor will drift less, however, for consistency, SST observations are only used when SSS observations are.

The location of the ship-track past Narsaq Trough varies from one transit to the next, ranging from far offshore, to on the continental shelf, to occasionally entering the adjacent fjords. Only transits that pass directly over the trough are used here, identified as follows: First, observations are separated into individual transits between -49 and -45 °E. Second, any transits

when the vessel is too far inshore (e.g. entering the adjacent fjords) are removed to maintain a consistent cross-shelf location along a given transit. Third, any transits when the vessel is too far offshore (likely due to the presence of sea ice on the shelf), are removed. To be included, transits must pass through the gate defined by 60.3663°N, -46.2246°E; 60.0253°N, -46.8338°E; 59.9641°N, -46.6815°E; 60.3663°N, -46.0470°E (Figure 3.1d). Further, for individual transits, observations offshore of the 350 m isobath upstream of -46.5 °E are removed. Finally, any transits with gaps in the observations of more than 30 minutes are removed to ensure sufficient data coverage to characterise the environmental conditions. This leaves a total of 198 transits with TSG data over Narsaq Trough. Note that temporal coverage of the 198 transits has a seasonal bias, with notably more TSG observations in June-December each year than in January-May (Figure 3.1b, purple).

3.2.3 Ocean velocity from a voluntary observing ship

The ocean velocity data come from a Teledyne RDI 75 kHz shipboard acoustic Doppler current profiler (sADCP) operated on the *Nuka Arctica* from late 2012 to 2020 (Rossby, Reverdin, Chafik, & Søiland, 2017; Chafik, Rossby, & Schrum, 2014; Knutsen et al., 2005). Ocean velocities measurements were made while the ship was underway. The sADCP was run in the narrow band mode with 16 m vertical bins, starting at a bin-center-depth of 31 m. We note that for two transits the returns are averaged in to 6 m bins, starting at 21 m, however, the analyses presented here are depth-means over multiple bins such that this discrepancy does not affect the results. The Teledyne RDI software VmDas was used for data acquisition. The data were post-processed using the University of Hawaii's CODAS software (CODAS software is available from the University of Hawaii Currents Group, SOEST: `http://currents.soest.hawaii.edu`). The raw acoustic pings in ship-coordinates were averaged over a 3-minute (2012-October 2018) or 5-minute (November 2018-2020) interval, corrected for transducer misalignment and rotated into earth coordinates. The sADCP routinely achieves a profiling range of 600 m and can reach 800 m in good weather conditions (Rossby et al., 2017), sufficient to reach the bottom of the

trough. These data were provided by Henrik Søiland (*pers. comm.*).

Further processing of the sADCP data is then completed for this study, as follows: First, ship-motion (calculated using ship speed and heading from the Thales ADU-5 GPS-based compasses) is removed: $u_{ocean} = u_{measured} + u_{ship}$ and $v_{ocean} = v_{measured} + v_{ship}$. Second, the quality control flags are applied to each bin, following the University of Hawaii Data Acquisition System conventions, only keeping bins when $pflag = 0$. Even after applying the quality control flags, velocity bins near bathymetry often appeared to be unrealistically large, with unphysical shear. As such, additional quality control is achieved by removing data below 100 m when the ocean speed is greater than 1 m.s^{-1} ($\sqrt{u_{ocean}^2 + v_{ocean}^2} > 1$). The 100 m threshold is chosen as the flow is surface-intensified, such that velocities of greater than 1 m.s^{-1} are realistic above 100 m, but are not expected below 100 m. A more rigorous approach would be to remove bins that exceed a given shear threshold. Simply removing data from bins within some distance of the bottom does not successfully remove the erroneous data, possibly due to the steep bathymetry.

Similar to in Section 3.2.2, the underway ocean velocity measurements are separated into individual transits over Narsaq Trough, between -49 and -45 °E, and only transits passing through the upstream gate are used (Figure 3.2b). Additionally, any transits that enter the fjords directly adjacent to the trough are excluded. Finally, transits with good bins in fewer than 1/4 of the velocity profiles between -49 and -45 °E are also excluded. This leaves a total of 56 sADCP transects over Narsaq Trough. Note that the temporal coverage sADCP observations has the same seasonal bias as the TSG observations, with notably more sADCP observations in June-December each year than in January-May (Figure 3.1b, green).

3.2.4 2022 hydrographic survey of Narsaq trough

As described in Chapter 2, a hydrographic survey of Narsaq Trough was conducted from September 7-21, 2022, as part of the AR69-03 cruise to turnaround a mooring array in southern Greenland. Here we use the underway SSS and SST measured by an SBE-45 MicroTSG thermosalinograph from a sea water intake located in the forward transducer well on the port

side, 5 meters below the waterline. These underway data are reported at 1-minute intervals.

3.2.5 Wind stress

The surface wind stress used here is from the Global Ocean Hourly Reprocessed Sea Surface Wind and Stress from Scatterometer and Model dataset (Copernicus Marine Service, 2024). This is a gridded reanalysis dataset of 10 meter winds and pre-calculated and corrected wind stress at hourly time-steps. The product is only used for the 2008-2023 period, when the grid-cell resolution is 1/8° (prior to 2008, the resolution is 1/4°).

3.3 Methods

This study focuses on the region bounded by 59 °N, -49 °E and 61 °N, -45 °E. This region allows for the identification of potential trough anomalies relative to upstream and downstream conditions along each ship track. The water column is divided into two main layers: above-shelf (0-100 m) and below-shelf (150-350 m, between the rim of the trough and the sill at the mouth of the trough; see Section 2.1.1). The upper layer is chosen to not be contiguous with the lower layer (i.e. 0-100 m instead of 0-150 m) as the flow is often surface intensified. Further, near-bottom velocity bins are often bad, such that there are few data in the 100-150 m range upstream and downstream of the trough.

Note that temporal means are indicated $\overline{y(x,t)}$ and spatial means are indicated $\langle y(x,t)\rangle$. Temporal means are means over multiple transits, whereas spatial means are means over the length of, or a portion of, a single transit. Further, for vector quantities such as ocean velocity and wind stress the subscripts denote the direction/component. For example, u_{cross} is the ocean velocity in the cross-shelf direction. Whereas for scalar quantities, such as SSS and SST, subscripts denote regions over which the scalar has been averaged. For example, $\left\langle \mathrm{SSSa}_{trough} \right\rangle$ is the mean sea surface salinity anomaly directly over the trough, for a given transit.

3.3.1 Characterising the water properties

The underway SSS and SST observations from the *Nuka Arctica* and *Tukuma Arctica* are used to characterise the spatial and temporal variability of water properties over Narsaq Trough. First, for every transit over the trough the underway (1- or 5-minute) SSS and SST observations are averaged into 0.1°E longitude bins ($\sim$ 5.5 km) between -49 to -45 °E such that there is a uniform distribution of data for each transit. Second, the large-scale temporal variability between transits is removed by calculating the SSS anomaly and SST anomaly for each transit:

$$\mathrm{SSSa} = \mathrm{SSS} - \langle \mathrm{SSS} \rangle \ , \tag{3.1}$$

$$\mathrm{SSTa} = \mathrm{SST} - \langle \mathrm{SST} \rangle \ , \tag{3.2}$$

where $\langle \mathrm{SSS} \rangle$ and $\langle \mathrm{SST} \rangle$ are the along-transit means (-49 to -45 °E) for each transit. This is necessary as there is considerable seasonal and shorter-timescale variability in the $\langle \mathrm{SSS} \rangle$ and $\langle \mathrm{SST} \rangle$ from one transit (standard deviation of $\pm$0.8 psu and $\pm$1.9 °C), making it difficult to compare the spatial/along-track variability from one transit to another. Taking the anomaly from the along-transit mean collapses the baseline SSS and SST variability between transits onto a common reference level, isolating the remaining spatial variability. Third, 2-dimensional temporal means of the SSSa and SSTa field over the trough are computed by gridding all the TSG observations into 0.1 °N by 0.2 °E ($\sim 11 \times 11$ km) grid cells and taking the mean over all data in each grid-cell (Figures 3.2b and 3.2c). Finally, the 1-dimensional time-mean SSSa and SSTa, $\overline{\mathrm{SSSa}}$ and $\overline{\mathrm{SSTa}}$, from -49 to -45 °E is calculated by taking the mean of the 0.1 °E binned along-transit SSSa and SSTa values over all transits (Figure 3.4, blue and orange).

To assess the temporal variability of water properties, transits are categorised as either having a negative, weak/no, or positive salinity anomaly over the trough as follows: First, the spatial-mean SSSa directly over the trough (-47.3 to -46.6 °E) is calculated for each transit, $\left\langle \mathrm{SSSa}_{trough} \right\rangle$. Second, the distribution of the magnitude of $\left\langle \mathrm{SSSa}_{trough} \right\rangle$ is estimated by sorting

$\langle \mathrm{SSSa}_{trough} \rangle$ into 0.1 psu bins (Figure 3.6a). Finally, each transit is categorised as either having a negative $\left(\langle \mathrm{SSSa}_{trough} \rangle < -0.15 \text{ psu}\right)$, weak/no $\left(-0.15 < \langle \mathrm{SSSa}_{trough} \rangle < -0.15 \text{ psu}\right)$, or positive $\left(\langle \mathrm{SSSa}_{trough} \rangle > 0.15 \text{ psu}\right)$ salinity anomaly over the trough (Figure 3.6a, shading). Note that SSS is used in preference to SST to categorise anomalous water properties as SST is sensitive to air temperature, particularly in the summer (Snow et al., 2021).

3.3.2 Characterising the flow-field

The sADCP observations from the *Nuka Arctica* are used to study the flow-field in the vicinity of Narsaq Trough. First, the velocities are rotated from Earth coordinates (East and North) into a cross-shelf (positive onshore) and along-shelf (positive towards the northwest, with the mean flow) coordinate system using an angle of rotation of $\theta_{rot} = 70^{\circ}$ counter-clockwise from East. Second, the depth-averaged velocity at each profile is calculated for two layers: above-shelf (0-100 m) and below-shelf (150-350 m; between the trough rim and the sill at the mouth of the trough). Third, the 2-dimensional mean flow-field for the above-shelf and below-shelf layers is computed by gridding all the sADCP observations into 0.1 °N by 0.2 °E grid cells ($\sim 11 \times 11$ km) as follows: For each transit and each layer, the mean u_{cross} and v_{cross} is calculated for each grid cell. Then, for each grid-cell, the time-mean $\overline{u_{cross}}$ and $\overline{v_{cross}}$ across all transits is calculated for each layer (Figures 3.3c and 3.3d). Finally, the 1-dimensional, all-transit composite of the flow past the trough (-49 to -45 °E) is calculated by taking the mean over all observations in 0.1 °E longitude bins ($\sim$ 5.5 km) for each depth layer (Figure 3.5, purple).

To assess the cross-shelf extent of the exchange flow, sADCP observations are sorted into transits over the mouth of the trough and transits over the trunk of the trough. "Mouth" transits are classified as those that are offshore of the 1000 m isobath at the canyon on the upstream edge of the trough (i.e. 60.15 °N, -46.6 °E, see Figure 3.1a for canyon location). "Trunk" transits are those that are inshore of the 1000 m isobath at the canyon. Composites for each region are created by first bin-averaging the velocities over 0.1 °E longitude bins ($\sim$ 5.5 km) for each transit and each depth layer and then taking the mean over all the transits in a given region (Figure 3.5).

3.3.3 Comparing the flow-field during different salinity anomalies

Forty six *Nuka Arctica* transits over the trough have both good TSG and good sADCP data: 13 transits when a positive salinity anomaly is observed over the trough, 31 transits when a weak/no salinity anomaly is observed, and 2 transits when a negative salinity anomaly is observed, as categorised in Section 3.3.1. The mean flow-field is calculated for transits when positive and weak/no salinity anomalies are observed over the trough as follows: First, for each transit, the cross-shelf velocity profiles are averaged in 0.1 °E longitude bins ($\sim$ 5.5 km) between -49 and -45 °E. Second, the layer-average (0-100 m or 150-350 m) is computed for each binned profile. Lastly, for each longitude bin and depth-layer, the mean and standard error of the mean is calculated over the transits with positive anomalies and transits with weak/no anomalies (Figure 3.8).

As only two transits when negative salinity anomalies are identified have usable co-located velocity profiles it was not reasonable to assume that a mean of these two transits would be representative of the true time-mean flow-field for these cases. Instead of calculating the mean flow-field over the negative salinity anomaly transits, the surface flow-field for each of the two transits is shown (Figure 3.9).

3.3.4 Wind forcing

The effects of surface wind-forcing on the cross-shelf exchange of water properties is assessed by comparing the wind stress over the trough during transits with positive, weak/no, and negative salinity anomalies. First, as is done or the ocean velocities, the wind stress is rotated from Earth coordinates (East and North) into a cross-shelf (positive onshore), τ_{cross}, and along-shelf (positive towards the northwest), τ_{along}, components. The same angle of rotation, $\theta_{rot} = 70°$ counter-clockwise from East, that is used for the ocean velocities is used for the winds (Figure 3.10b, grey arrows). Second, a spatial mean of the gridded wind stress fields over the trough is calculated, $\langle \tau_{cross} \rangle$ and $\langle \tau_{along} \rangle$, taking the mean over the area bounded by

60.25 °N, -45.95 °E; 60.62 °N, -47.36 °E; 60.32 °N, -48.07 °E; and 59.97 °N, -46.58 °E (Figure 3.10b). Third, the time-series of the wind stress in the 100 hours preceding and following each trough-crossing is isolated. The timing of the trough-crossing for each transit (i.e. $t = 0$ hours), is defined as when the ship crosses the -47 °E meridian in the TSG dataset. Fourth, composite time-series of the wind stress over transits with positive, negative, and weak/no salinity anomalies (as defined in Section 3.3.1) are created by taking the mean over all time-series for transits within each salinity anomaly category, $\overline{\tau_{cross}}$ and $\overline{\tau_{along}}$ (Figure 3.10b and 3.10c). Note that the wind stress product only covers the 2008-2023 period, whereas the TSG data covers the 2002-2023 period, as such there are fewer transits with concurrent wind stress time-series in each salinity anomaly category than in the full TSG dataset but the distribution is similar (Figure 3.10a versus Figure 3.6a).

3.4 Results

Below we synthesize the observed physical properties within and around the trough. First, we describe the mean conditions of the sea surface water properties and the flow-field. Second, we use the mean conditions to contextualise the observations from the 2022 hydrographic survey results. Third, we analyse the temporal variability in the sea surface water properties over the trough, assessing the effects of the flow-field on the strength of the salinity anomalies. Fourth, we describe how the wind forcing varies during different SSS conditions.

3.4.1 Mean conditions at Narsaq Trough

Surface water properties over the trough are typically warmer and saltier than waters upstream and downstream of the trough (Figure 3.2). In the time-mean over the 2010-2023 period, satellite-derived SST isotherms bend in towards the coast at the trough (Figure 3.2a), indicative of Atlantic Water (AW) crossing the shelf-break near the trough. However, the algorithm used to produce the GHRSST MUR product results in smoothing of the temperature field at times, limiting analysis of the mesoscale features on a time-step by time-step basis. Instead, hereafter

we focus on in situ observations from voluntary observing ships transiting over the trough.

Over the 2002-2023 period, in situ observations show recurring salty and warm anomalies over the trough, relative to the along-track SSS and SST means, SSSa and SSTa respectively (Figure 3.2b and 3.2c, see Eq. (3.1) and Eq. (3.2) for definitions). The time-mean SSSa over all transits, $\overline{\text{SSSa}}$, peaks over the trough, with a maximum of 0.33 psu (Figure 3.4, blue). The time-mean SSTa, $\overline{\text{SSTa}}$, also peaks over the trough, with a maximum of 0.32 °C (Figure 3.4, orange). Both $\overline{\text{SSSa}}$ and $\overline{\text{SSTa}}$ are relatively symmetric over the trough, however, $\overline{\text{SSTa}}$ is colder upstream of the trough than downstream (Figure 3.4, orange).

In the flow-field, a persistent signal of cross-shelf exchange is observed at the trough (Figure 3.3). Above the shelf (0-100 m) the flow starts to veer on-shelf upstream of the trough and is deflected back off-shelf over the downstream wall of the trough (Figures 3.3a and 3.3c). Over the 2012-2020 period, the mean strength of the above-shelf exchange flow is 0.2 m.s^{-1} (Figure 3.4, purple). Below the shelf-depth (150-350 m, between the trough rim and the sill at the mouth of the trough) a weaker exchange flow exists, again with inflow on the upstream wall and outflow on the downstream wall (Figures 3.3b and 3.3d). These above- and below-shelf circulations are consistent with bathymetric steering of the along-shelf flow, which is otherwise dominated by the WGC and WGCC.

At the surface, the mean cross-shelf exchange flow, $\overline{u_{cross}}$, is co-located with the maximums in the mean along-shelf salinity and temperature anomalies, $\overline{\text{SSSa}}$ and $\overline{\text{SSTa}}$ (Figure 3.4). Notably, both the $\overline{\text{SSSa}}$ and $\overline{\text{SSTa}}$ maximums are aligned with the zero-crossing of the exchange flow (Figure 3.4, vertical black dashed lines). The co-location of the anomalously warm, salty water and the exchange flow is indicative of the exchange flow transporting AW onto the shelf over the trough.

3.4.2 Contextualising the 2022 survey observations

In 2022, during a hydrographic survey of Narsaq Trough, off-shelf flow above the shelf and a cross-shelf exchange flow below the shelf was observed in the trunk of the trough

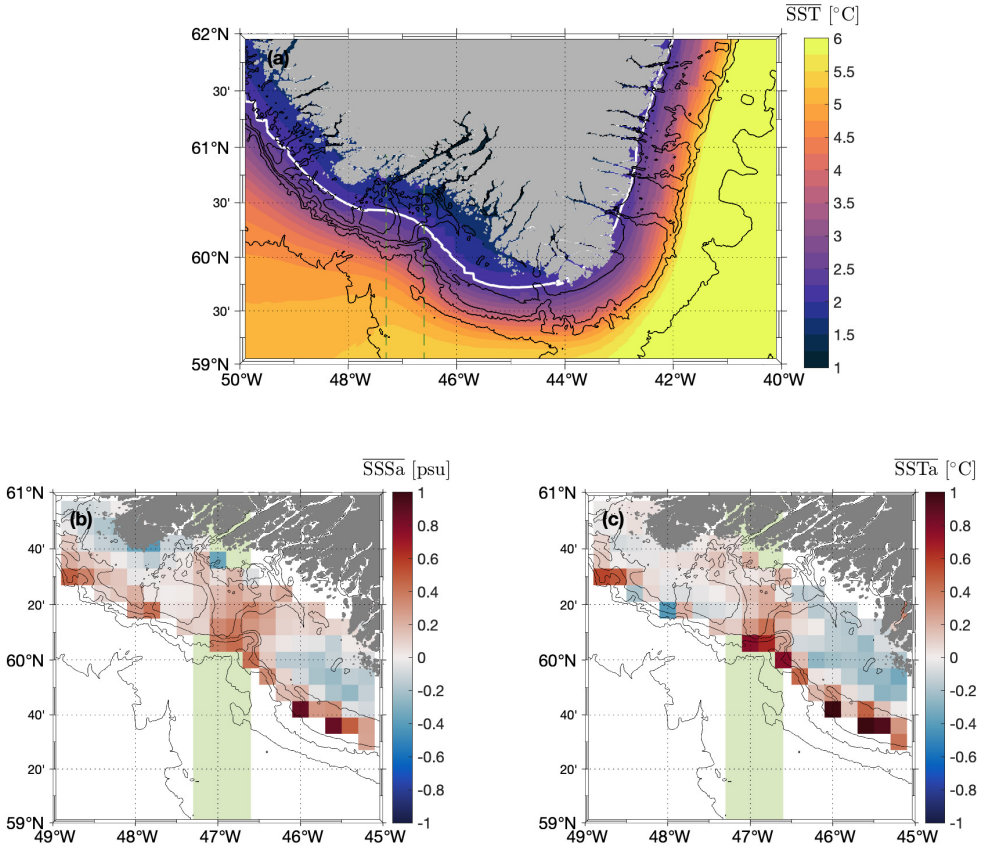

Figure 3.2. Time-mean sea surface water properties over Narsaq trough. (a) Mean SST from the GHRSST MUR product over 2010-2023, with the 2.25 °C isotherm accentuated (white line). Gridded mean (b) $\overline{\text{SSSa}}$ and (c) $\overline{\text{SSTa}}$ over 2002-2023 from the voluntary observing ship observations (see Section 3.3.1). In all panels the longitudinal extent of the trough is shown ((a) dashed green lines and (b-c) green swath) and the 150, 350, 1000, 2000, and 3000 m isobaths are shown (black lines).

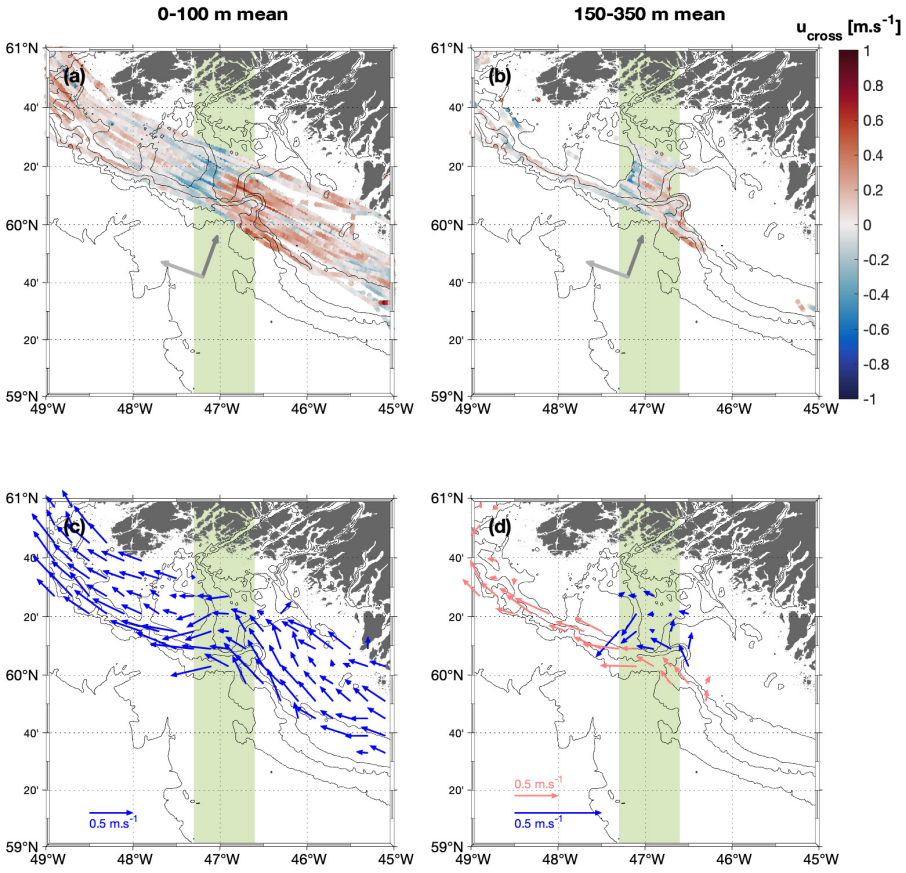

Figure 3.3. Flow-field over the trough over the 2012 to 2020 period. Depth-averaged cross-shelf velocity over the (a) above-shelf layer (0-100 m) and (b) below-shelf layer (150-350 m) along each transit past the trough. Gridded, time-mean flow-field over the (c) above-shelf layer and (d) below-shelf layer. In all panels the 150, 350, 1000, 2000, and 3000 m isobaths are overlain (black lines) and the longitudinal extent of the trough is highlighted (green swath). In (a-b) grey arrows indicate the coordinate system (dark grey arrow indicates positive cross-shelf direction). In (c-d) the scale of the quivers is shown; note that two scales are used in (d) to emphasize the cross-shelf exchange (blue arrows) which is dwarfed by the along-shelf flow (red arrows).

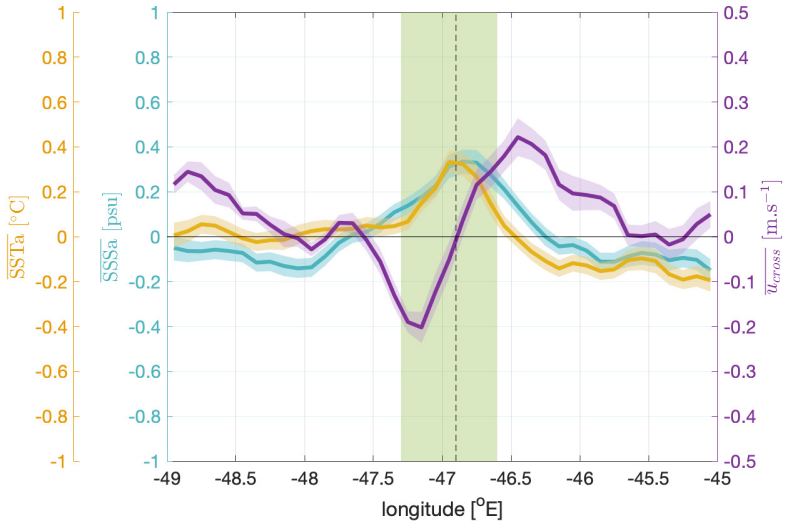

Figure 3.4. Comparison of along-shelf structure of the mean sea surface salinity anomaly, $\overline{\text{SSSa}}$ (blue), sea surface temperature anomaly, $\overline{\text{SSTa}}$ (orange), and cross-shelf velocity over the 0-100 m layer, $\overline{u_{cross}}$ (purple). For each variable the temporal mean across all transits (solid lines) and standard error of the mean (shading) are shown. The longitudinal extent of the trough (green swath) and the location of the flow reversal (vertical dashed black line) are also shown.

(Figure 2.6e). While the below-shelf circulation is consistent with the temporal-mean circulation presented here, the above-shelf flow is not (Figure 3.5b and 3.5c, purple and black). The absence of an exchange flow above the shelf in 2022 cannot be explained by the location of the survey transect relative to the trough mouth. The strength of the mean flow over the trunk is comparable to the strength over the mouth of the trough, indicating the exchange flow regularly penetrates the length of the trough (Figure 3.5b, pink and blue).

Although the above- and below-shelf observations from the voluntary observing ship transits indicate that the bathymetrically-steered exchange flow is a persistent, surface-intensified feature of the outer and inner trough, the 2022 hydrographic survey suggests that under some forcing the above-shelf flow can become de-coupled from the below-shelf flow. Due to the limited length of the cross-trunk transect in 2022, it is difficult to determine how the water properties over the trough differed from upstream and downstream at the time of occupation. However, surface waters over the trough were fresher and warmer than observations on the shelf upstream of the trough (-46 to -45.5 °E), 12 hours prior to the cross-trunk transect (not shown). Fresher

waters are indicative of offshore transport of inner-shelf waters, while the warmer temperature suggests some contribution of exported fjord waters which have been warmed by the sun.

3.4.3 Temporal variability at Narsaq Trough

As suggested by the temporal-mean over all transits, $\overline{\text{SSSa}}$, the majority of transits have a positive spatial-mean SSSa directly over the trough, $\langle \text{SSSa}_{trough} \rangle$, although $\langle \text{SSSa}_{trough} \rangle$ is negative at times (Figure 3.6a). The magnitude of $\langle \text{SSSa}_{trough} \rangle$ has a skewed distribution, peaking between 0.05 and 0.15 psu, with 53 % of transits having positive salinity anomalies, 40 % of transits having weak/no salinity anomalies, and 8 % of transits having negative salinity anomalies (see Section 3.3.1 for definitions of the salinity anomaly categories). As is the case for the all-transit means, the positive salinity anomalies co-occur with warm temperature anomalies over the trough (Figures 3.6b and 3.6c, red). On the other hand, negative salinity anomalies co-occur with cold temperature anomalies (Figures 3.6b and 3.6c, blue). Positive salinity anomalies over the trough were most commonly observed in late summer and fall (Figure 3.6d), whereas there are too few negative anomalies to discern seasonal variability (Figure 3.6e). We emphasize that, even for the positive anomaly cases, the observed temporal distribution is biased by the temporal distribution of the transits (Figure 3.1b), which involve few transits in spring, likely due to the presence of sea ice forcing the ships to take a more offshore path.

Upstream of Narsaq Trough, the continental shelf-break typically separates surface PW, fresher than 34 g.kg^{-1} and colder than 4 °C, from the saltier, warmer AW offshore of the 150 m isobath (Pacini et al., 2020; Foukal & Pickart, 2023). When negative salinity anomalies are observed, water properties over the trough are cold and fresh, resembling PW properties (Figure 3.7d). In contrast, water properties over the trough tend to be warmer and saltier when positive salinity anomalies are observed, although there is a wide spread in these properties, such that they do not closely match the expected AW properties (Figure 3.7b). Notably, the spread in the water properties when positive anomalies are present spans most of the T-S space covered by the entire dataset from the voluntary observing ships (Figure 3.7b, red versus grey). The

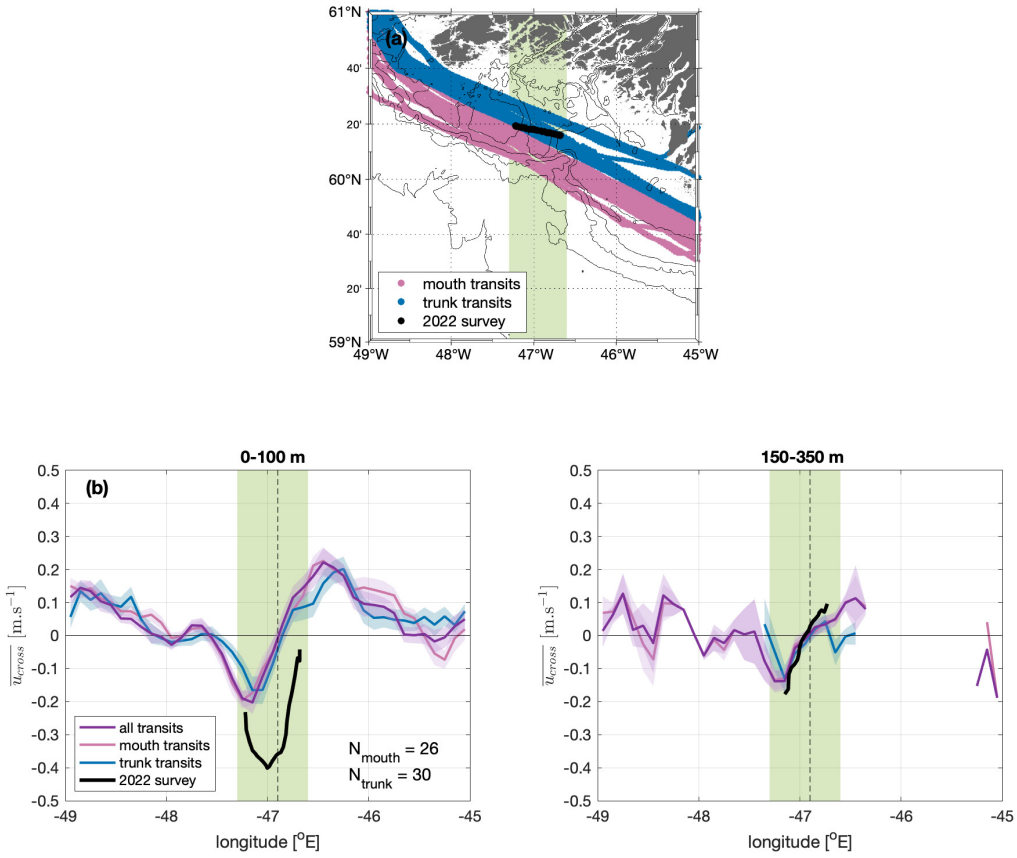

Figure 3.5. Cross-shelf velocity at the mouth and trunk of the trough. (a) Map showing location of transits over the mouth (pink) and trunk (blue) of the trough, and the 2022 hydrographic survey transit (black). Time-mean cross-shelf velocity for all transits (purple), mouth transits (pink), and trunk transits (blue) over the (b) above-shelf layer (0-100 m) and (c) below-shelf layer (150-350 m). In (b-c) bold lines show the mean over the selected transits and shading indicates the standard error of the mean (where there is more than one transit). In addition, the cross-shelf velocity from the single cross-trough transit during the 2022 survey is shown (black).

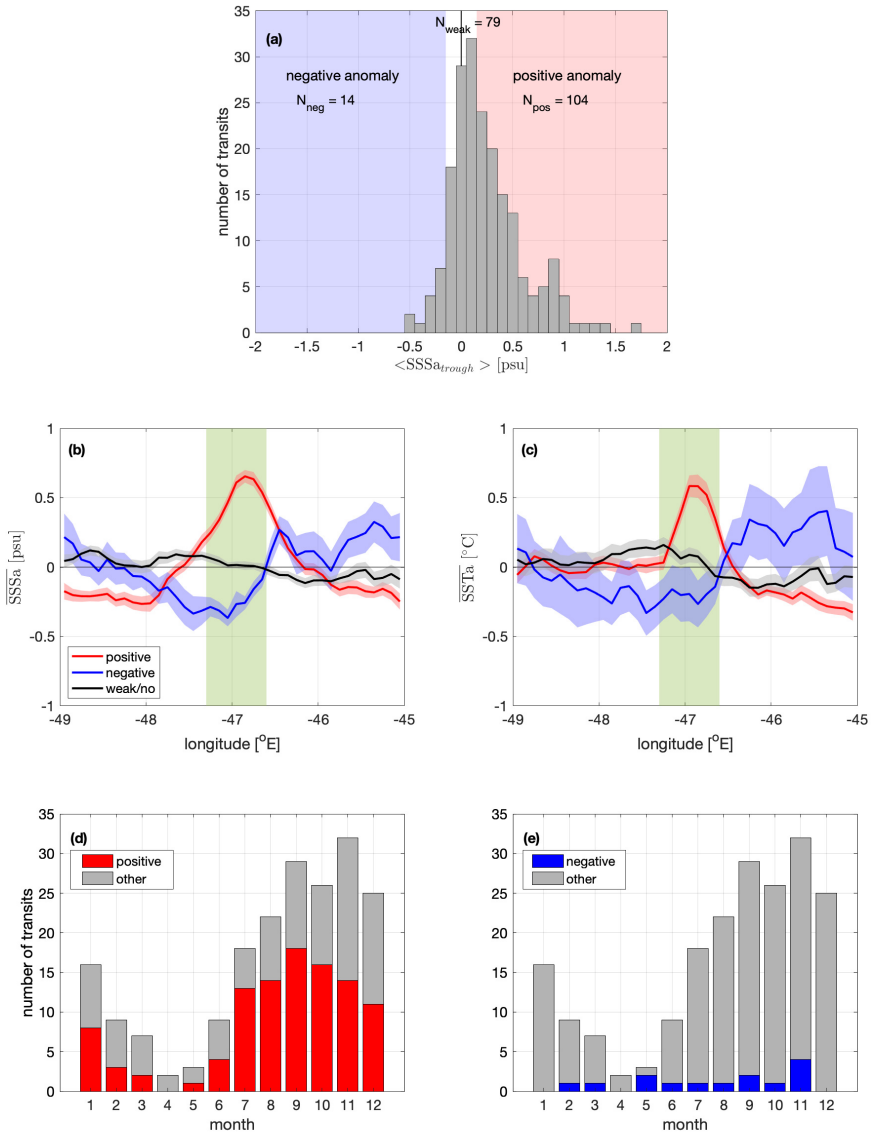

Figure 3.6. Variability in water properties over the trough. (a) Distribution of the magnitude of the mean SSSa between the trough bounds, $\langle \mathrm{SSSa}_{trough} \rangle$, showing portions classified as having negative salinity anomalies (blue shading), weak/no salinty anomalies (no shading), and positive salinity anomalies (red shading). N_{neg}, N_{weak}, and N_{pos} are the total number of transits classified as having negative, weak/no, and positive anomalies, respectively. Spatial structure of mean (b) SSSa and (d) SSTa over transits with positive anomalies (red), negative anomalies (blue), and weak/no anomalies (black); shading indicates the standard error of the mean. Seasonal distribution of transits with (d) positive salinity anomalies over the trough and (e) negative salinity anomalies over the trough, compared to the temporal distribution of all transits.

voluntary observing ships provide year-round observations, capturing sub-seasonal, seasonal and interannual variability which results in the large spread in T-S space (Figures 3.7b and 3.7d, grey). The spread in T-S space is much smaller in the reference observations from the hydrographic survey as those observations where only taken in September 2022 (Figure 3.7b and 3.7d, black and purple).

The magnitude of the salinity anomaly over the trough cannot easily be explained by differences in the cross-shelf flow. Above the shelf (0-100 m), a pronounced cross-shelf exchange flow exists even when weak/no salinity anomalies are observed (Figure 3.8a, black), which is not statistically different in strength from the mean exchange flow when positive salinity anomalies are observed (Figure 3.8a; i.e. the standard error of the means overlap). Similarly, below the shelf (150-350 m), the cross-shelf exchange flow is of comparable magnitude during positive and weak/no anomalies (Figure 3.8b). In addition, the along-shelf flow, both above and below the shelf, is not statistically significantly different during positive and weak/no salinity anomalies (Figure 3.8c and 3.8d). In other words, we find that for both positive and weak/no salinity anomaly cases the flow-field is characterised by a strong cross-shelf exchange flow at the surface and subsurface.

For the negative salinity anomaly cases, only two out of the 15 transits have good sADCP data such that it is not possible to determine a representative mean flow-field during these events. However, during both these transits, the surface flow (0-50 m) is on-shelf upstream of the trough and off-shelf over the trough (Figure 3.9). Off-shelf flow co-located with a negative salinity anomaly suggests off-shelf transport of PW. Note that a shallower depth-layer is used to illustrate the flow-field during these negative salinity anomaly cases as the cross-shelf flow is strongly surface-intensified on 7 July 2016. The surface off-shelf during these two events is similar to the off-shelf flow observed during the 2022 survey (Figure 2.6e). Additionally, observations during a transect 12 hours before the trunk transect suggest surface waters over the trough were fresher, but also warmer, than waters on the shelf upstream of the trough (not shown). In sum, these limited observations suggest that, under certain circumstances, the surface flow at the trough no

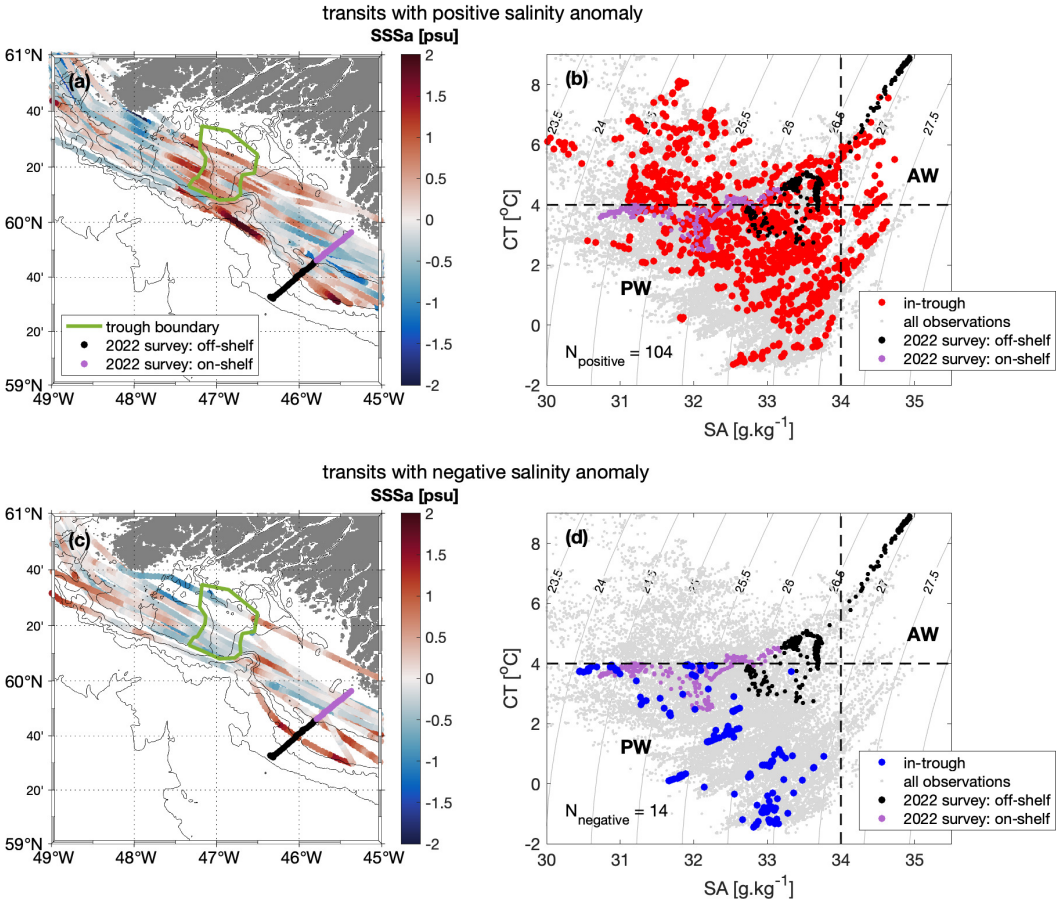

Figure 3.7. Water properties of (a-b) positive salinity anomalies and (c-d) negative salinity anomalies over the trough. SSSa along each transit for (a) positive anomaly cases and (c) negative anomaly cases. The 150, 350, 1000, 2000, and 3000 m isobaths are overlain (black lines). (b) T-S distribution for observations over the trough (inside green boundary in (a), approximately following the 150 m isobath) for positive anomaly cases (red). (d) T-S distribution for observations over the trough (inside green boundary in (c)) for negative anomaly cases (blue). In (b) and (d) the T-S distribution during all transits, over the entire region, is shown for reference (small grey dots). Underway SSS and SST from the hydrographic survey (September 2022), divided into on-shelf (bottom depth $<$ 150 m, purple) and off-shelf (bottom depth $>$ 150 m, black) are also shown to illustrate typical cross-shelf surface water property structure. Potential density isopycnals at 0.5 kg.m^{-3} increments (grey lines) are overlain in addition to rough boundaries for AW and PW (black dashed lines).

longer follows isobaths and instead flows off-shelf, likely exporting PW.

3.4.4 Wind forcing in relation to water properties

The mean local winds over the trough are upwelling-favourable during the transits of the voluntary observing ships (Figure 3.10); consistent with the local prevailing wind conditions (Moore & Renfrew, 2005). However, the wind stress over the trough, τ, is highly variable, with mean standard deviations of $\pm$ 0.2-0.3 N.m^{-2} for both τ_{along} and τ_{cross}. For transits with a positive salinity anomaly over the trough, the mean along-shelf wind stress, $\overline{\tau_{along}}$, is weakly upwelling-favourable preceding and during the transit over the trough (Figure 3.10c, red). Whereas for transits with a weak/no salinity anomaly over the trough $\overline{\tau_{along}}$ is more strongly upwelling-favourable preceding and during the transit (Figure 3.10c, black). Further, the mean cross-shelf wind stress, $\overline{\tau_{cross}}$, is weakly offshore preceding and during transits with a positive salinity anomaly, whereas for transits with weak/no salinity anomaly $\overline{\tau_{cross}}$ is near zero preceding the transits and then ramps up to be offshore during the transit (Figure 3.10d, red and black respectively). Finally, within the period that we have wind reanalysis, there are too few transits when negative salinity anomalies are observed to comment on the mean wind forcing for these cases (Figures 3.10c and 3.10d, blue).

3.5 Summary and discussion

Observations from voluntary observing ships transiting over Narsaq Trough show that a cross-shelf exchange flow is a persistent feature of the flow-field at the trough, both above and below the shelf. Further, mean sea surface temperature and salinity are elevated over the trough, relative to waters on the shelf upstream and downstream of the trough. The co-location of the warmer and saltier water over the trough with the exchange flow suggests that the trough is deflecting AW in the WGC on-shelf, crossing the front between the PW on the continental shelf and the AW off the continental shelf.

While a barotropic exchange flow and positive sea surface temperature and salinity

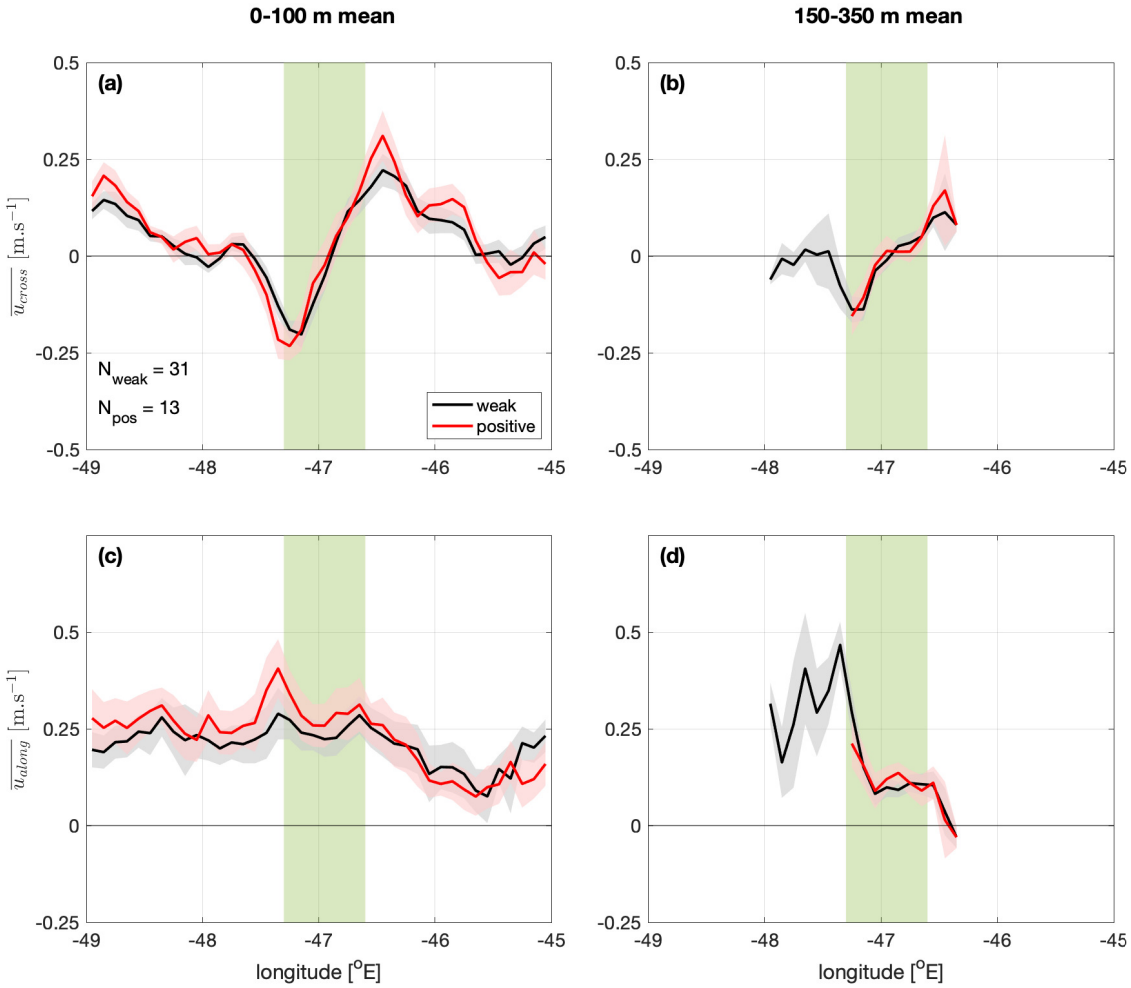

Figure 3.8. Mean, depth-averaged along-track velocities for transits with positive salinity anomalies (red) and weak/no salinity anomalies (black). Mean cross-shelf velocity over the (a) above-shelf layer (0-100 m) and (b) below-shelf layer (150-350 m). Mean along-shelf velocity over the (c) above-shelf layer and (d) below-shelf layer. In all panels the bold lines are the transit-means, shading indicates the standard error of the mean, and the longitudinal extent of the trough is highlighted (green swath). In (b) and (d) only data between -48 and -46 °E are shown as the observations are gappy outside of this region due to the bathymetry.

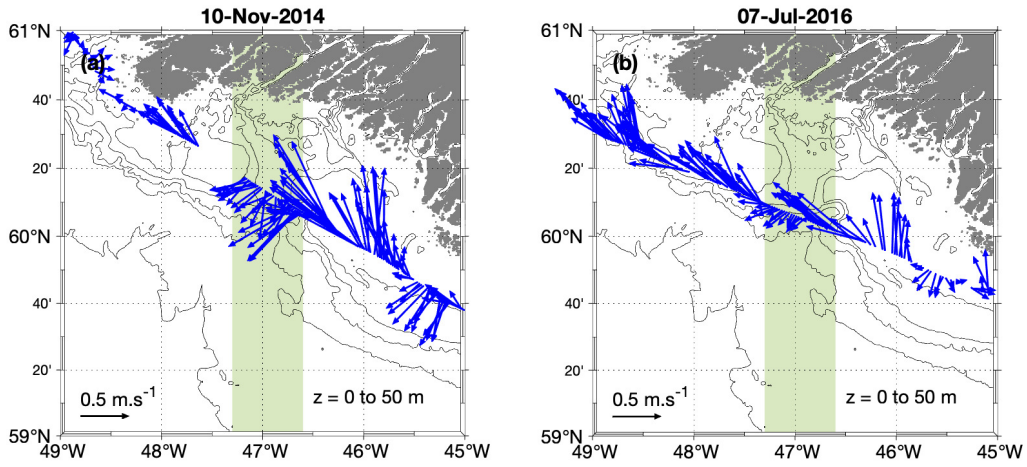

Figure 3.9. Two instances of the flow over the trough when a negative salinity anomaly was observed over the trough: (a) 10 November 2014 and (b) 7 July 2016. Velocities presented are depth-averaged over the 0-50 m layer (blue vectors); a scale vector is given for reference (black arrow). The 150, 350, 1000, 2000, 3000 m isobaths and the longitudinal extent of the trough (green swath) are shown.

anomalies are the norm over the trough, there are times when this regime breaks down. During 40 % of transits, sea surface salinity and temperature over the trough do not differ significantly from the upstream or downstream properties (Figure 3.6b and 3.6c, black), although a surface and subsurface cross-shelf exchange flow is present (Figure 3.8a and 3.8b). The absence of temperature and salinity anomalies over the trough in these cases suggests the exchange flow is not driving on-shelf transport of AW. We suggest that the lack of AW transport could be explained by stronger upwelling-favourable winds driving offshore Ekman transport and pushing the front between the AW and PW further offshore (Figure 3.10c, black). As such, the exchange flow at the trough no longer crosses the front and instead redirects flow within the domain of the PW. Under weaker upwelling-favourable winds, the AW front can relax back towards the shelf-break, allowing the exchange flow to transport AW onto the shelf, as appears to be the case for the positive salinity anomalies (Figure 3.10c, red).

Further, during 8 % of transits, fresher and colder waters are observed over the trough (Figure 3.6b and 3.6c, blue). While there are few co-located ocean velocity profiles for these

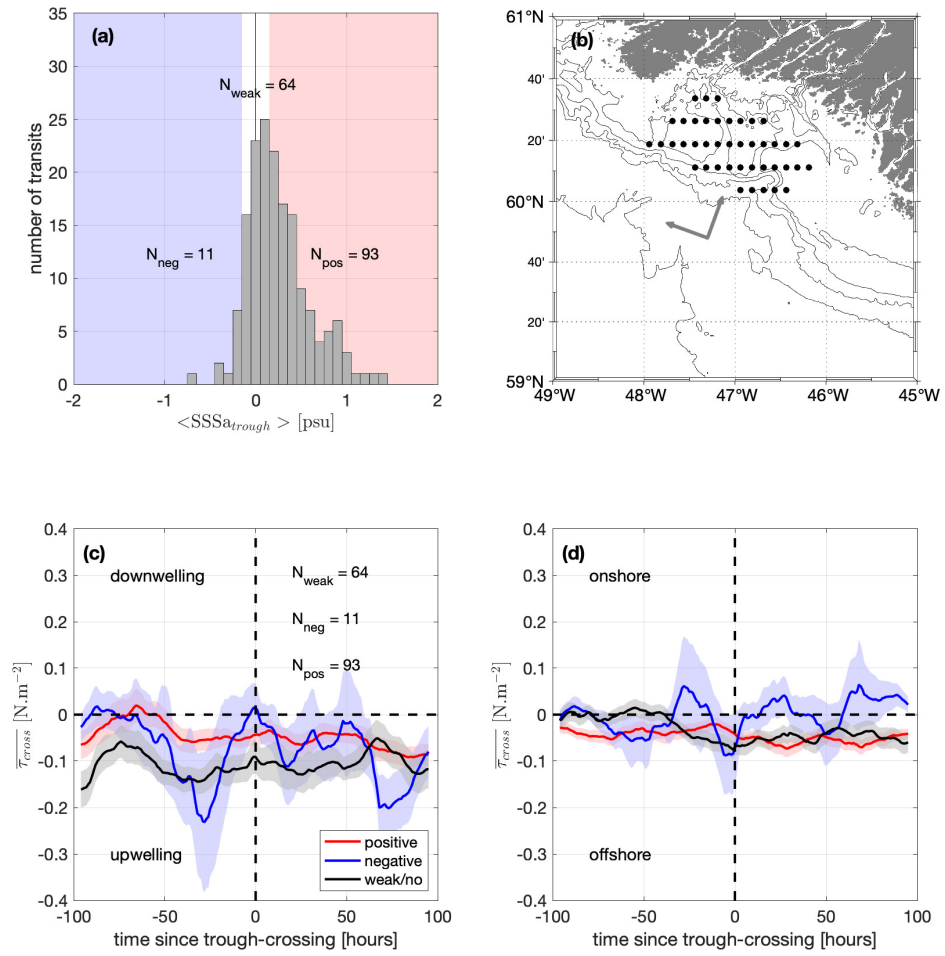

Figure 3.10. Mean wind-forcing over transits with positive, negative and weak/no salinity anomalies. (a) Distribution of the strength of the salinity anomaly over the trough for the 2008-2023 period (for which winds are available); categorised as either a negative anomaly (blue shading), a weak/no anomaly (no shading), or a positive anomaly (red shading). The number of transits in each category are shown (N_{neg}, N_{weak}, and N_{pos}). (b) Location of wind product grid-cells used in spatial average for the following panels. Time-series of mean (c) along-shelf and (d) cross-shelf wind stress over the trough for transits in each category; the standard error of the mean is also shown (shading). Colours in (c) and (d) indicate salinity anomaly category: positive (red), negative (blue), weak/no (black).

cases, the limited evidence suggests that these negative anomalies are the result of offshore transport of surface waters at the trough (Figure 3.9). There is a cross-shelf temperature and salinity gradient on the Greenland continental shelf, with the coldest, freshest waters closest to the coast (Pacini et al., 2020), as such, offshore transport of inner-shelf waters at the trough would result in the observed negative temperature and salinity anomaly in the along-shelf direction. In this study, anomalously cold, fresh water was observed over the trough following periods of strong upwelling-favourable wind forcing and during possible offshore wind events (Figures 3.10c and 3.10d, blue). However, the wind analysis is a composite of only 11 events and may not be representative of the true mean wind-forcing when negative salinity anomalies occur.

3.5.1 Cross-shelf transport of AW and PW

This study has shown that a persistent, surface-intensified exchange flow exists at Narsaq Trough, both above and below the shelf. However, as underway temperature and salinity measurements from voluntary observing ship are only made at the surface, we are left to make educated guesses about the water mass transport of the subsurface exchange flow. Below the shelf, cross-shelf exchange flow must transport AW into the trough, as this is the only water at this depth; consistent with observations during the 2022 survey (Figure 2.6). However, it appears that the de-coupled surface and subsurface flow observed during the 2022 survey (surface outflow, subsurface exchange flow; Figure 2.6e) is an infrequent (although not one-off) occurrence. As such, the high vertical dissipation occurring in the trough during the 2022 survey may have been higher than is typical, resulting from increased vertical shear due to the de-coupled surface and subsurface flow; consistent with Brearley et al. (2017). The mean amount of subsurface export of trough-modified AW may therefore be smaller than initially thought, but remains a quantity we cannot quantify.

The presence of the exchange flow at the surface suggests that modified AW may also be produced at the surface, in addition to in the subsurface (Chapter 2). The surface flow likely entrains PW while being steered around the trough, ultimately exporting a mixture of AW and

PW from the shelf on the downstream wall of the trough, as suggested by the slight upstream skew of $\overline{\mathrm{SSSa}}$ (Figures 3.4, blue and 3.6b, red). In addition, repeat transits have shown that, on occasion, the surface exchange flow can be disrupted and replaced by outflow of PW over the width of the trough, which is presumably exported off-shelf. Lastly, during the surface outflow event observed during the 2022 survey, warm, fresh waters were observed near the coast (not shown), consistent with the properties of surface waters in the adjacent fjords (Figure 2.7), suggesting that the trough may also enhance export of fjord waters (Snow et al., 2023; Sutherland & Cenedese, 2009; Cape, Straneo, Beaird, Bundy, & Charette, 2019).

The finding presented here that weaker upwelling winds support more transport of AW on-shelf differ from the findings of Snow et al. (2023). Snow et al. (2023) found that upwelling-favourable winds drive onshore transport of AW at troughs in southeast Greenland, both at the surface and in the subsurface. The onshore transport at the surface is explained by upwelling winds reversing the along-shelf flow and arresting coastal-trapped topographic lee waves generated by the trough (Snow et al., 2023; Zhang & Lentz, 2017). At Narsaq Trough, however, surface onshore transport of AW appears more prevalent under weak upwelling conditions than under strong upwelling conditions. Further, stronger winds in the direction of the along-shelf flow are known to enhance shelf circulation and increase transport of shelf-break waters into an adjacent trough (Dundas et al., 2024). Therefore, it follows that stronger winds opposing the along-shelf flow, as is the case for upwelling winds at Narsaq Trough, likely reduce the shelf circulation and weaken inflow of shelf-break waters. However, this dynamical argument is not supported by the some of the observations presented here, which show the exchange flow has a similar magnitude under stronger and weaker upwelling conditions (Figures 3.8a and 3.10c). A possible explanation for this discrepancy is that the strength and structure of the currents flowing past Narsaq Trough may be more sensitive to remote wind forcing over the southeast Greenland shelf than local forcing over the southwest Greenland shelf (Foukal & Pickart, 2023).

Finally, we speculate about the contribution of wind-forcing during presumed off-shelf

transport of PW, i.e. over the limited number of transits with negative salinity anomalies. For transits when a negative salinity anomaly is observed the along-shelf wind stress is upwelling-favourable and onshore 1 day (28 hours) before the transit, shifting to purely offshore wind stress at the time of the transit (Figure 3.10c and 3.10d, blue). This wind-forcing alone does not explain the fresher water over the trough as upwelling and offshore wind conditions drive offshore transport in the upper ocean, advecting low salinity surface waters towards the shelf-break both over the trough and up- and down-stream. However, a possible explanation is that the bathymetry of the trough sustains the wind-driven flow, allowing the off-shelf transport of PW to persist over the trough as the upwelling winds shift to offshore winds, such that there is greater off-shelf flow over the trough than elsewhere on the shelf. This is the inverse of the case described by Dundas et al. (2024), where wind-driven onshore flow in a trough lasts several days after wind-forcing has relaxed.

3.5.2 Possible future directions

This study opens several questions for future investigation:

1. Is there a signal of surface freshening in transits that pass Narsaq Trough just offshore of the shelf-break, indicative of offshore export of PW? The observations presented here suggest that the trough may drive export of PW offshore at the surface as a result of a bathymetrically-steered exchange flow. However, this study focused on observations on the continental shelf, excluding observations offshore of the shelf-break.

2. Can the mean heat and freshwater transport of the exchange flow at Narsaq Trough be estimated? While ocean velocity observations from the voluntary observing ships are full-depth, temperature and salinity observations are limited to the sea surface temperature. To quantify mean heat and freshwater transports associated with the exchange flow in the trough, this limitation needs to be circumvented.

3. Is the exchange flow, and associated cross-shelf transport of AW, also seen at the troughs on

the continental shelf downstream of Narsaq Trough? Narsaq Trough is the southern-most trough of seven troughs between Cape Farewell and Davis Strait (the northern boundary of the Labrador Sea). The *Nuka Arctica* and *Tukuma Arctica* transit over all of these, providing a unique opportunity to compare the degree to which each trough drives cross-shelf exchange and assess the cumulative impact of successive troughs on water mass properties.

4. How does the canyon on the upstream edge of the mouth of Narsaq Trough affect the cross-shelf exchange? The steep, deep canyon on the shelf-break just upstream of Narsaq Trough (Figure 3.1a) likely enhances cross-shelf exchange but may also have biased the magnitude of the salinity anomaly over the trough.

5. Does Narsaq Trough also drive cross-shelf exchange of carbon? From 2005 to 2020, the *Nuka Arctica* carried an underway pCO_2 sensor (Olsen et al., 2008), such that the water property analysis conducted here could be extended to carbon. Carbon dioxide is more soluble in cold, fresh water than warm, salty water, such that the PW on Greenland's continental shelf is an effective carbon sink (Rysgaard et al., 2012; Meire et al., 2015). If the carbon-rich PW is exported off the continental shelf into the convective basins of the subpolar North Atlantic, a process that may be enhanced by troughs, it can be sequestered at depth for hundreds of years.

3.6 Conclusion

Unique observations from two decades of repeat transits by voluntary observing ships have enabled a study of mean conditions and temporal variability of the flow-field and water properties at Narsaq Trough. Observations show a persistent, bathymetrically-steered exchange flow exists at the trough, both above and below the continental shelf. Above the shelf, onshore flow on the upstream wall of the trough transports AW on-shelf the majority of the time, possibly exporting entrained PW in the outflow in the downstream wall. However, it is also common for

an exchange flow to exist that does not transport AW onshore, possibly as a result of upwelling winds shifting the front between the AW and PW offshore such that the exchange flow no longer crosses it. In a minority of cases, the above-shelf flow at the trough becomes decoupled from the exchange flow below the shelf, with outflow of PW over the width of the trough, indicative of export of PW from the shelf. While temperature and salinity observations do not exist at depth, it can be assumed that AW is also transported into the trough below the shelf, although the degree of vertical mixing with any overlying PW may be less than previously thought due to reduced vertical shear when the surface and subsurface flow are coupled. These results suggest that troughs on the Greenland shelf enhance cross-shelf exchange, funneling warm water onshore with the potential to drive melt at marine-terminating glaciers. While the *Nuka Arctica* and *Tukuma Arctica* underway datasets have been used in the eastern subpolar North Atlantic, the datasets remain underutilised on Greenland's continental shelf, leaving ample opportunity for future studies of the cumulative effects of troughs on cross-shelf exchange and the role of troughs in driving export of carbon- and oxygen-rich PW to the open ocean.

3.7 Acknowledgments

I gratefully acknowledge the U.S. National Science Foundation: this work was supported by NSF OCE-1948482. I am deeply grateful to the French Sea Surface Salinity Observation Service for their work collecting and curating the underway SSS and SST datasets. Thank you to Gilles Reverdin and Philippe Téchiné for helping me find and use these data. Many, many thanks to Henrik Søiland for providing the underway sADCP data from the *Nuka Arctica*. Thank you to all the field teams (scientists, technicians and crew) that conducted the 2022 hydrographic survey of Narsaq Trough as part of the OSNAP AR69-03 cruise. Special thanks to Nicole Abib for compiling the underway SSS and SST data from the cruise.

This chapter is in preparation for publication as "Persistence of cross-shelf exchange at Narsaq Trough, Greenland, observed from voluntary observing ships" by M. Nelson, F. Straneo,

and S. Purkey. The dissertation author was the primary investigator and author of this paper.

Conclusion

The ocean in the subpolar North Atlantic plays a crucial role in regulating Earth's climate. However, the region is undergoing notable changes as we overheat our atmosphere: warming oceans and melting land-ice are increasing ocean stratification, potentially limiting the deep mixing and water mass transformation that drives large-scale ocean circulation and injects oxygen and carbon into the ocean interior, in addition to driving sea level rise. These changes threaten to destabilise the climate further. As such, investigating the dynamics that govern the subploar North Atlantic teaches us how it will respond to, and contribute to, the changing climate, enabling science-informed mitigation and adaptation strategies. To understand the whole, complex system of the subpolar North Atlantic, it is useful to break the system down into constituent parts of the ocean-atmosphere-ice system, as we have done here.

In Chapter 1 we focus on the large-scale open ocean, using the densification of the Irminger Sea in 2015 as an opportunity to study the dynamics of its subsequent restratification and recovery. The study leverages in situ observations of ocean temperature and salinity from repeat, ship-based hydrography and free-drifting profiling floats, as well as estimates of eddy kinetic energy from remote-sensing. We find that the recovery of the Irminger interior was two-stage: an initial slow buoyancy gain while the Irminger Current recovered, which set up the necessary conditions to drive a more rapid second-stage recovery of the interior through transport of buoyant water from the Irminger Current to the Irminger interior via baroclinic instabilities. The widespread nature of the strong atmospheric forcing in 2015 not only drove buoyancy loss over the Irminger interior, but also reduced buoyancy in the Irminger Current. In turn, the number of eddies shed from the Irminger Current into the interior, and the buoyancy content of said

eddies, was reduced, delaying the recovery of the interior. The slow recovery of the interior allowed for several subsequent years of deep convection, despite a return to normal atmospheric forcing after 2015. This work shows that convection and restratification in the Irminger Sea are sensitive to the conditions in the boundary current that circulates around the basin.

While this work focused on physical properties, the restratification dynamics may have implications for ocean biogeochemistry. Subsurface oxygen concentrations are much lower to the east of Reykjanes Ridge than to the west in the Irminger Sea (Fröb et al., 2016; de Jong & de Steur, 2016; Feucher et al., 2022). As such, advection of this oxygen-poor water into the interior by eddies may be a significant, but typically neglected, term in the oxygen budget for the Irminger interior. However, it is unclear whether the contribution of these eddies will increase or decrease ventilation in the Irminger interior. After the oxygen-poor water is advected into the interior, it is cooled during the winter, increasing oxygen solubility, likely resulting in the water becoming undersaturated in oxygen, such that it is able to take up considerable oxygen from the atmosphere. Interannual variability in the eddy transport from the Reykjanes Ridge may therefore introduce interannual variability in the deep oxygen content of the Irminger interior; a contribution which has yet to be studied.

In Chapter 2, we shift our focus to the Greenland continental shelf and use a 2-week hydrographic survey of Narsaq Trough to investigate how the trough modifies the local environment in terms of ocean circulation and water mass properties. We find that the surface flow is deflected around the back of the trough, with outflow over the trough, while a horizontal exchange flow is observed within the trough at depth. Subsurface waters within the trough are fresher, oxygen-enriched, and nutrient-depleted relative to waters at the same depth off the shelf, suggesting that inflowing Atlantic Water is mixed with overlying Polar Water. It is suspected that this modified Atlantic Water is then exported out of the trough, back to the shelf-break.

Chapter 3 builds on Chapter 2 by leveraging observations from two decades of repeat transits by cargo vessels outfitted with oceanographic sensors to investigate the mean and temporal variability in ocean conditions at Narsaq Trough. This time-series of observations

shows that cross-shelf exchange of Atlantic Water and Polar Water is a persistent feature of the trough, which typically drives a coupled exchange flow that reaches from the bathymetry of the trough to the surface. As such, the decoupled surface and subsurface flow at the trough, observed in Chapter 2, is understood to be an uncommon state of the flow-field at the trough. Moreover, the surface exchange flow transports Atlantic Water on-shelf the majority of the time, where it likely entrains Polar Water before being exported again on the downstream wall. However, it is also common for the trough to support an exchange flow that does not drive transport of Atlantic Water onto the continental shelf, which can be explained by the front between the Atlantic Water and Polar Water moving offshore, possibly as a result of local wind forcing. Finally, during a minority of cases, anomalously cold and fresh surface water is observed over the trough, concurrent with observations of surface outflow over the trough, indicative of export of Polar Water from the shelf to the shelf-break.

This research highlights the need to have high-quality bathymetry maps in order to accurately estimate cross-shelf exchange on the Greenland contiental shelf. This is not a given, and bathymetry products can vary considerably. We note that BedMachine bathymetry (Morlighem et al., 2017) was used here in preference to GEBCO bathymetry (GEBCO Compilation Group, 2023) as the GEBCO product had a seamount in the center of the trough that was not observed in shipboard multibeam surveys. As bathymetry plays a large role in steering flow and driving mixing it is important to have accurate representations of bathymetry, which likely requires more sea floor mapping and compilation of data from diverse research vessels.

Chapters 2 and 3 contribute to the growing body of evidence that troughs on the Greenland continental shelf drive onshore heat transport, as has been established for Antarctica (Moffat & Meredith, 2018; Couto et al., 2017; Morrison, Hogg, England, & Spence, 2020). However, more work needs to be done to understand the role of troughs in driving export of freshwater off of Greenland's continental shelf, as has been shown to occur when cold, fresh eddies are funneled offshore by trough circulation in Antarctica (Brearley et al., 2019). Further, Greenland's continental shelf is riddled with troughs, such that it would be informative to study the cumulative

effect of flow interacting with multiple troughs while circulating around the continent. As the troughs on Greenland's continental shelf vary widely in size and geometry, a first step in such a study would be to compare the dynamics at Narsaq Trough with other nearby troughs, which could be done using the voluntary observing ship dataset. A second step could be further investigating the biogeochemical implications in terms of carbon and oxygen export to the open ocean and nutrient import to the continental shelf. Chapter 3 suggests that AW is transported onto the shelf at the surface, in addition to the subsurface, likely facilitating mixing of nutrient-rich Atlantic Water with oxygen-rich Polar Water in the euphotic zone which may enhance primary productivity in trough environments.

While this thesis has focused on the exchange of waters across the continental shelf-break, the transport of trough waters into adjacent fjords needs greater attention. Large-scale global climate modeling efforts often use an off-shelf temperature profile to force melting of marine-terminating glaciers in Greenland's fjords, without resolving, or at best parameterising, modification of the temperature profile that occurs during advection to the glacier terminus (Slater et al., 2020). This may over-estimate temperatures of waters reaching the terminus due to mixing between Atlantic Water and the overlying Polar Water resulting from shear instabilities in troughs and turbulence when waters flow over sills at the mouths of the fjords (S. L. Howard et al., 2004; Venables et al., 2017). However, the coupling of the surface and subsurface flow shown in Chapter 3 suggests that the mixing and modification of water properties in the trough may not be as strong as suspected based on findings from Chapter 2. In addition to affecting ice-melt, mixing of Atlantic Water and Polar Water in troughs, prior to entering fjords, will set the nutrient and oxygen properties of the fjord waters, with implications for fjord ecosystems.

Finally, I emphasize the opportunity to leverage observations from voluntary observing ships to study oceanographic processes on the Greenland continental shelf. While Greenland has a couple of its own research vessels, there is more demand than supply for ship-time, such that doing fieldwork typically requires additional ships traveling from far afield - with the associated financial burden, greenhouse gas emissions, and parachute science implications. Voluntary

observing ships are already transiting the area, providing an essential delivery of goods to Greenland and a useful platform for unobtrusive science. Further, the vessels operate year-round in a remote region which is hard to get to and hard to navigate in the long winter months, collecting in situ observations that are nearly impossible to achieve with traditional science vessels. While remote-sensing is often touted as the solution to the need for frequent observations in hard-to-get places, satellites often fall short in coastal regions like Greenland's continental shelf where it is crucial to resolve small spatial scales and where cloud-cover and ice-cover are frequent. While satellite technology improves, while science funding in the United States is limited, and while we work to decolonise science, I encourage the community of scientists studying Greenland to make the most of the unique datasets provided by the voluntary observing ships.

In closing, I want to acknowledge that as a scientist studying the ocean's role in the global climate system I feel it is my responsibility to not only produce more science but to also advocate for action based on what our science is telling us. We know that the greenhouse gas pollution from human activity over the last 200 years is destablising our global climate, putting hundreds of millions of already vulnerable people at further risk of food insecurity from drought; of illness from waterborne-diseases following unprecedented rains and flooding; and of housing insecurity should their homes be lost to sea level rise or ruined by super-charged hurricanes or bombed by resource-driven war; ultimately driving climate-forced migration (Daoust & Selby, 2024). And yet earth scientists so often feel trapped by the need to remain objective, such that they do not feel it is their place to advocate for climate mitigation and adaptation (Dablander et al., 2024). However, we are the experts in how volatile the climate is becoming and how long it will take to turn the metaphorical ship that is the climate around.

I believe it is time for scientists to accept two things: First, it is objectively true that we need to take action to mitigate the climate crisis to protect the majority of the world's population, so calling for climate action does not make you a subjective scientist. Second, we are all already inherently biased as a result of diverse backgrounds, upbringings, and positions (which is why

we need a diverse group of scientists conducting research). During my PhD I have witnessed the science community beginning to understand these two tenets, but there is a long way to go and no time to lose. As scientists we can change how we do our own science to minimise climate impacts and also advocate for policy and procedural changes at our institutions as well as at the local, state, and federal government level (Dupont, Jacob, & Philippe, 2025). As the saying goes: "never doubt that a small group of committed people can change the world; in fact, it's the only thing that ever has". Let's be part of that small group, working to make the world more equitable and safe, but let's recongnise that doing so will take more than just churning out more science.

Bibliography

Allen, S., & Hickey, B. (2010). Dynamics of advection-driven upwelling over a shelf break submarine canyon. *Journal of Geophysical Research: Oceans*, *115*(C8). Retrieved 2023-05-09, from https://onlinelibrary.wiley.com/doi/abs/10.1029/2009JC005731 doi: 10.1029/2009JC005731

Alory, G., Delcroix, T., Téchiné, P., Diverrès, D., Varillon, D., Cravatte, S., ... Roubaud, F. (2015, November). The French contribution to the voluntary observing ships network of sea surface salinity. *Deep Sea Research Part I: Oceanographic Research Papers*, *105*, 1–18. Retrieved 2025-04-02, from https://www.sciencedirect.com/science/article/pii/S0967063715001417 doi: 10.1016/j.dsr.2015.08.005

Amante, C., & Eakins, B. (2009). *ETOPO1 1 Arc-Minute Global Relief Model: Procedures, Data Sources and Analysis.* National Geophysical Data Center, NOAA. doi: doi:10.7289/V5C8276M

Arndt, J. E., Jokat, W., Dorschel, B., Myklebust, R., Dowdeswell, J. A., & Evans, J. (2015). A new bathymetry of the Northeast Greenland continental shelf: Constraints on glacial and other processes. *Geochemistry, Geophysics, Geosystems*, *16*(10), 3733–3753. Retrieved 2024-06-19, from https://onlinelibrary.wiley.com/doi/abs/10.1002/2015GC005931 (_eprint: https://onlinelibrary.wiley.com/doi/pdf/10.1002/2015GC005931) doi: 10.1002/2015GC005931

Atlas, E., Hager, S., Gordon, L., & Park, P. K. (1971). *A Practical Manual for Use of the Technicon (Trade Name) Autoanalyzer (Trade Name) in Seawater Nutrient Analyses; Revised.* (Tech. Rep. No. AD0730482). Oregon State University. Retrieved 2024-06-15, from https://apps.dtic.mil/sti/citations/AD0730482

AVISO+Altimetry. (2021). *SSALTO/DUACS User Handbook: Eddy Kinetic Energy (EKE) monthly mean products.* CNES. Retrieved from https://www.aviso.altimetry.fr/fileadmin/documents/data/tools/monthly_mean_eke_hdbk.pdf (SALP-MU-P-EA-23506-CLS)

Bakker, P., Schmittner, A., Lenaerts, J. T. M., Abe-Ouchi, A., Bi, D., van den Broeke, M. R., ... Yin, J. (2016). Fate of the Atlantic Meridional Overturning Circulation: Strong decline under continued warming and Greenland melting. *Geophysical Research Letters*, *43*(23), 12,252–12,260. Retrieved 2024-06-19, from https://onlinelibrary.wiley.com/doi/abs/10.1002/2016GL070457 (_eprint: https://onlinelibrary.wiley.com/doi/pdf/10.1002/2016GL070457) doi: 10.1002/2016GL070457

Bamber, J., van den Broeke, M., Ettema, J., Lenaerts, J., & Rignot, E. (2012).

Recent large increases in freshwater fluxes from Greenland into the North Atlantic. *Geophysical Research Letters*, *39*(19). Retrieved 2025-05-13, from https://onlinelibrary.wiley.com/doi/abs/10.1029/2012GL052552 (_eprint: https://onlinelibrary.wiley.com/doi/pdf/10.1029/2012GL052552) doi: 10.1029/2012GL052552

Bamber, J. L., Westaway, R. M., Marzeion, B., & Wouters, B. (2018, June). The land ice contribution to sea level during the satellite era. *Environmental Research Letters*, *13*(6), 063008. Retrieved 2025-05-13, from https://dx.doi.org/10.1088/1748-9326/aac2f0 (Publisher: IOP Publishing) doi: 10.1088/1748-9326/aac2f0

Beaird, N. L., Straneo, F., Le Bras, I., Pickart, R., & Jenkins, W. J. (2023). Glacial Meltwater in the Current System of Southern Greenland. *Journal of Geophysical Research: Oceans*, *128*(12), e2023JC019658. Retrieved 2023-12-12, from https://onlinelibrary.wiley.com/doi/abs/10.1029/2023JC019658 (_eprint: https://onlinelibrary.wiley.com/doi/pdf/10.1029/2023JC019658) doi: 10.1029/2023JC019658

Beardsley, R. C., Limeburner, R., & Brechner Owens, W. (2004). Drifter measurements of surface currents near Marguerite Bay on the western Antarctic Peninsula shelf during austral summer and fall, 2001 and 2002. *Deep Sea Research Part II: Topical Studies in Oceanography*, *51*(17), 1947–1964. Retrieved 2024-06-19, from https://www.sciencedirect.com/science/article/pii/S0967064504001183 doi: 10.1016/j.dsr2.2004.07.031

Bendtsen, J., Rysgaard, S., Carlson, D. F., Meire, L., & Sejr, M. K. (2021). Vertical Mixing in Stratified Fjords Near Tidewater Outlet Glaciers Along Northwest Greenland. *Journal of Geophysical Research: Oceans*, *126*(8), e2020JC016898. Retrieved 2025-04-08, from https://onlinelibrary.wiley.com/doi/abs/10.1029/2020JC016898 (_eprint: https://onlinelibrary.wiley.com/doi/pdf/10.1029/2020JC016898) doi: 10.1029/2020JC016898

Biló, T. C., Straneo, F., Holte, J., & Le Bras, I. a.-A. (2022). Arrival of New Great Salinity Anomaly Weakens Convection in the Irminger Sea. *Geophysical Research Letters*, *49*(11), e2022GL098857. Retrieved 2023-03-10, from https://onlinelibrary.wiley.com/doi/abs/10.1029/2022GL098857 (_eprint: https://onlinelibrary.wiley.com/doi/pdf/10.1029/2022GL098857) doi: 10.1029/2022GL098857

Brearley, J. A., Meredith, M. P., Naveira Garabato, A. C., Venables, H. J., & Inall, M. E. (2017). Controls on turbulent mixing on the West Antarctic Peninsula shelf. *Deep Sea Research Part II: Topical Studies in Oceanography*, *139*, 18–30. Retrieved 2024-06-19, from https://www.sciencedirect.com/science/article/pii/S0967064517300437 doi: 10.1016/j.dsr2.2017.02.011

Brearley, J. A., Moffat, C., Venables, H. J., Meredith, M. P., & Dinniman, M. S. (2019). The Role of Eddies and Topography in the Export of Shelf Waters From the West Antarctic Peninsula Shelf. *Journal of Geophysical Research: Oceans*, *124*(11), 7718–7742. Retrieved 2025-02-18, from https://onlinelibrary.wiley.com/doi/abs/10.1029/2018JC014679 (_eprint: https://onlinelibrary.wiley.com/doi/pdf/10.1029/2018JC014679) doi: 10.1029/2018JC014679

Broecker, W. S. (1987). The biggest chill. *Natural History Magazine*, *97*, 74–82.

Broecker, W. S. (1991). THE GREAT OCEAN CONVEYOR. *Oceanography*, *4*(2), 79–89.

Böning, C. W., Behrens, E., Biastoch, A., Getzlaff, K., & Bamber, J. L. (2016, July). Emerging impact of Greenland meltwater on deepwater formation in the North Atlantic Ocean. *Nature Geoscience*, *9*(7), 523–527. Retrieved 2025-05-13, from https://www.nature.com/articles/ngeo2740 (Publisher: Nature Publishing Group) doi: 10.1038/ngeo2740

Cape, M. R., Straneo, F., Beaird, N., Bundy, R. M., & Charette, M. A. (2019, January). Nutrient release to oceans from buoyancy-driven upwelling at Greenland tidewater glaciers. *Nature Geoscience*, *12*(1), 34–39. Retrieved 2025-05-14, from https://www.nature.com/articles/s41561-018-0268-4 (Publisher: Nature Publishing Group) doi: 10.1038/s41561-018-0268-4

Castelao, R. M., Luo, H., Oliver, H., Rennermalm, A. K., Tedesco, M., Bracco, A., ... Medeiros, P. M. (2019). Controls on the Transport of Meltwater From the Southern Greenland Ice Sheet in the Labrador Sea. *Journal of Geophysical Research: Oceans*, *124*(6), 3551–3560. Retrieved 2024-07-02, from https://onlinelibrary.wiley.com/doi/abs/10.1029/2019JC015159 (_eprint: https://onlinelibrary.wiley.com/doi/pdf/10.1029/2019JC015159) doi: 10.1029/2019JC015159

Chafik, L., Holliday, N. P., Bacon, S., & Rossby, T. (2022). Irminger Sea Is the Center of Action for Subpolar AMOC Variability. *Geophysical Research Letters*, *49*(17), e2022GL099133. Retrieved 2022-12-14, from https://onlinelibrary.wiley.com/doi/abs/10.1029/2022GL099133 (_eprint: https://onlinelibrary.wiley.com/doi/pdf/10.1029/2022GL099133) doi: 10.1029/2022GL099133

Chafik, L., Rossby, T., & Schrum, C. (2014). On the spatial structure and temporal variability of poleward transport between Scotland and Greenland. *Journal of Geophysical Research: Oceans*, *119*(2), 824–841. Retrieved 2025-04-15, from https://onlinelibrary.wiley.com/doi/abs/10.1002/2013JC009287 (_eprint: https://onlinelibrary.wiley.com/doi/pdf/10.1002/2013JC009287) doi: 10.1002/2013JC009287

Chelton, D. B., Schlax, M. G., & Samelson, R. M. (2011, October). Global observations of nonlinear mesoscale eddies. *Progress in Oceanography*, *91*(2), 167–216. Retrieved 2023-04-04, from https://www.sciencedirect.com/science/article/pii/S0079661111000036 doi: 10.1016/j.pocean.2011.01.002

Chin, T. M., Vazquez-Cuervo, J., & Armstrong, E. M. (2017, October). A multi-scale high-resolution analysis of global sea surface temperature. *Remote Sensing of Environment*, *200*, 154–169. Retrieved 2025-03-26, from https://www.sciencedirect.com/science/article/pii/S0034425717303462 doi: 10.1016/j.rse.2017.07.029

Copernicus Marine Service. (2024). *Global Ocean Hourly Reprocessed Sea Surface Wind and Stress from Scatterometer and Model [Dataset]*. Copernicus Marine. Retrieved 2024-10-24, from https://data.marine.copernicus.eu/product/WIND_GLO_PHY_L4_MY_012_006/description doi: 10.48670/moi-00185

Couto, N., Martinson, D. G., Kohut, J., & Schofield, O. (2017). Distribution of Upper Circumpolar Deep Water on the warming continental shelf of the West Antarctic Peninsula. *Journal of Geophysical Research: Oceans*, *122*(7), 5306–5315. Re-

trieved 2024-06-17, from https://onlinelibrary.wiley.com/doi/abs/10.1002/2017JC012840 (_eprint: https://onlinelibrary.wiley.com/doi/pdf/10.1002/2017JC012840) doi: 10.1002/2017JC012840

Dablander, F., Sachisthal, M. S. M., Cologna, V., Strahm, N., Bosshard, A., Grüning, N.-M., ... Haslbeck, J. M. B. (2024, October). Climate change engagement of scientists. *Nature Climate Change*, *14*(10), 1033–1039. Retrieved 2025-05-19, from https://www.nature.com/articles/s41558-024-02091-2 (Publisher: Nature Publishing Group) doi: 10.1038/s41558-024-02091-2

Daoust, G., & Selby, J. (2024). Climate change and migration: A review and new framework for analysis. *WIREs Climate Change*, *15*(4), e886. Retrieved 2025-05-19, from https://onlinelibrary.wiley.com/doi/abs/10.1002/wcc.886 (_eprint: https://onlinelibrary.wiley.com/doi/pdf/10.1002/wcc.886) doi: 10.1002/wcc.886

Darelius, E., Dundas, V., Janout, M., & Tippenhauer, S. (2023, May). Sudden, local temperature increase above the continental slope in the southern Weddell Sea, Antarctica. *Ocean Science*, *19*(3), 671–683. Retrieved 2025-05-20, from https://os.copernicus.org/articles/19/671/2023/ (Publisher: Copernicus GmbH) doi: 10.5194/os-19-671-2023

de Jong, M. F., Bower, A. S., & Furey, H. H. (2016, June). Seasonal and Interannual Variations of Irminger Ring Formation and Boundary–Interior Heat Exchange in FLAME. *Journal of Physical Oceanography*, *46*(6), 1717–1734. Retrieved 2023-06-13, from https://journals.ametsoc.org/view/journals/phoc/46/6/jpo-d-15-0124.1.xml (Publisher: American Meteorological Society Section: Journal of Physical Oceanography) doi: 10.1175/JPO-D-15-0124.1

de Jong, M. F., & de Steur, L. (2016). Strong winter cooling over the Irminger Sea in winter 2014-2015, exceptional deep convection, and the emergence of anomalously low SST: IRMINGER SEA COOLING AND CONVECTION. *Geophysical Research Letters*, *43*(13), 7106–7113. Retrieved 2020-09-01, from http://doi.wiley.com/10.1002/2016GL069596 doi: 10.1002/2016GL069596

de Jong, M. F., de Steur, L., Fried, N., Bol, R., & Kritsotalakis, S. (2020). Year-Round Measurements of the Irminger Current: Variability of a Two-Core Current System Observed in 2014–2016. *Journal of Geophysical Research: Oceans*, *125*(10), e2020JC016193. Retrieved 2023-06-12, from https://onlinelibrary.wiley.com/doi/abs/10.1029/2020JC016193 (_eprint: https://onlinelibrary.wiley.com/doi/pdf/10.1029/2020JC016193) doi: 10.1029/2020JC016193

de Jong, M. F., Oltmanns, M., Karstensen, J., & de Steur, L. (2018, March). Deep Convection in the Irminger Sea Observed with a Dense Mooring Array. *Oceanography*, *31*(1), 50–59. Retrieved 2022-12-14, from https://tos.org/oceanography/article/deep-convection-in-the-irminger-sea-observed-with-a-dense-mooring-array doi: 10.5670/oceanog.2018.109

de Jong, M. F., van Aken, H. M., Våge, K., & Pickart, R. S. (2012, May). Convective mixing in the central Irminger Sea: 2002–2010. *Deep Sea Research Part I: Oceanographic Research Papers*, *63*, 36–51. Retrieved 2022-12-14, from https://dukespace.lib.duke.edu/dspace/handle/10161/9576 (Accepted: 2015-04-13T14:28:30Z Publisher: Elsevier BV) doi: 10.1016/j.dsr.2012.01.003

Delcroix, T., Alory, G., Téchiné, P., Diverrès, D., Varillon, D., Cravatte, S., ... Roubaud, F. (2002). *Sea Surface Salinity data from Voluntary Observing Ships Network. [dataset].* Odatis. doi: https://doi.org/10.6096/SSS-LEGOS#v22.0

D'Errico, J. (2006). *Surface Fitting using gridfit [Software].* Retrieved 2024-07-02, from https://www.mathworks.com/matlabcentral/fileexchange/8998-surface-fitting-using-gridfit

Dillon, T. M. (1982). Vertical overturns: A comparison of Thorpe and Ozmidov length scales. *Journal of Geophysical Research: Oceans*, *87*(C12), 9601–9613. Retrieved 2024-10-01, from https://onlinelibrary.wiley.com/doi/abs/10.1029/JC087iC12p09601 (_eprint: https://onlinelibrary.wiley.com/doi/pdf/10.1029/JC087iC12p09601) doi: 10.1029/JC087iC12p09601

Dukhovskoy, D. S., Myers, P. G., Platov, G., Timmermans, M.-L., Curry, B., Proshutinsky, A., ... Somavilla, R. (2016). Greenland freshwater pathways in the sub-Arctic Seas from model experiments with passive tracers. *Journal of Geophysical Research: Oceans*, *121*(1), 877–907. Retrieved 2023-05-24, from https://onlinelibrary.wiley.com/doi/abs/10.1002/2015JC011290 doi: 10.1002/2015JC011290

Dundas, V., Daae, K., & Darelius, E. (2024). Storm-Driven Warm Inflow Toward Ice Shelf Cavities—An Idealized Study of the Southern Weddell Sea Continental Shelf System. *Journal of Geophysical Research: Oceans*, *129*(9), e2023JC020749. Retrieved 2024-09-25, from https://onlinelibrary.wiley.com/doi/abs/10.1029/2023JC020749 (_eprint: https://onlinelibrary.wiley.com/doi/pdf/10.1029/2023JC020749) doi: 10.1029/2023JC020749

Dupont, L., Jacob, S., & Philippe, H. (2025, January). Scientist engagement and the knowledge–action gap. *Nature Ecology & Evolution*, *9*(1), 23–33. Retrieved 2025-05-19, from https://www.nature.com/articles/s41559-024-02535-0 (Publisher: Nature Publishing Group) doi: 10.1038/s41559-024-02535-0

Duyck, E., & De Jong, M. (2021). Circulation Over the South-East Greenland Shelf and Potential for Liquid Freshwater Export: A Drifter Study. *Geophysical Research Letters*, *48*(5), e2020JB020886. Retrieved 2023-05-19, from https://onlinelibrary.wiley.com/doi/abs/10.1029/2020GL091948 doi: 10.1029/2020GL091948

Duyck, E., Gelderloos, R., & de Jong, M. F. (2022). Wind-Driven Freshwater Export at Cape Farewell. *Journal of Geophysical Research: Oceans*, *127*(5), e2021JC018309. Retrieved 2023-03-27, from https://onlinelibrary.wiley.com/doi/abs/10.1029/2021JC018309 doi: 10.1029/2021JC018309

Edwards, B., Murphy, D., Janzen, C., & Larson, N. (2010, May). Calibration, Response, and Hysteresis in Deep-Sea Dissolved Oxygen Measurements. Retrieved 2024-08-02, from https://journals.ametsoc.org/view/journals/atot/27/5/2009jtecho693_1.xml (Section: Journal of Atmospheric and Oceanic Technology) doi: 10.1175/2009JTECHO693.1

Egbert, G. D., & Erofeeva, S. Y. (2002). Efficient Inverse Modeling of Barotropic Ocean Tides. Retrieved 2024-09-03, from https://journals.ametsoc.org/view/journals/atot/19/2/1520-0426_2002_019_0183_eimobo_2_0_co_2.xml (Section: Journal of Atmospheric and Oceanic Technology)

Evans, J., Ó Cofaigh, C., Dowdeswell, J. A., & Wadhams, P. (2009). Marine geophysical evidence

for former expansion and flow of the Greenland Ice Sheet across the north-east Greenland continental shelf. *Journal of Quaternary Science*, *24*(3), 279–293. Retrieved 2024-06-19, from https://onlinelibrary.wiley.com/doi/abs/10.1002/jqs.1231 (_eprint: https://onlinelibrary.wiley.com/doi/pdf/10.1002/jqs.1231) doi: 10.1002/jqs.1231

Fan, X., Send, U., Testor, P., Karstensen, J., & Lherminier, P. (2013, April). Observations of Irminger Sea Anticyclonic Eddies. *Journal of Physical Oceanography*, *43*(4), 805–823. Retrieved 2022-12-14, from https://journals.ametsoc.org/view/journals/phoc/43/4/jpo-d-11-0155.1.xml (Publisher: American Meteorological Society Section: Journal of Physical Oceanography) doi: 10.1175/JPO-D-11-0155.1

Fer, I. (2006, January). Scaling turbulent dissipation in an Arctic fjord. *Deep Sea Research Part II: Topical Studies in Oceanography*, *53*(1), 77–95. Retrieved 2025-03-05, from https://www.sciencedirect.com/science/article/pii/S0967064506000087 doi: 10.1016/j.dsr2.2006.01.003

Fer, I., Skogseth, R., & Haugan, P. M. (2004). Mixing of the Storfjorden overflow (Svalbard Archipelago) inferred from density overturns. *Journal of Geophysical Research: Oceans*, *109*(C1). Retrieved 2024-09-25, from https://onlinelibrary.wiley.com/doi/abs/10.1029/2003JC001968 (_eprint: https://onlinelibrary.wiley.com/doi/pdf/10.1029/2003JC001968) doi: 10.1029/2003JC001968

Feucher, C., Portela, E., Kolodziejczyk, N., & Thierry, V. (2022, November). Subpolar gyre decadal variability explains the recent oxygenation in the Irminger Sea. *Communications Earth & Environment*, *3*(1), 1–9. Retrieved 2023-02-14, from https://www.nature.com/articles/s43247-022-00570-y (Number: 1 Publisher: Nature Publishing Group) doi: 10.1038/s43247-022-00570-y

Firing, E., & Gordon, R. (1990). Deep ocean acoustic Doppler current profiling. In *Proceedings of the IEEE Fourth Working Conference on Current Measurement* (pp. 192–201). Retrieved 2024-09-03, from https://ieeexplore.ieee.org/document/110905 doi: 10.1109/CURM.1990.110905

Firing, E., & Hummon, J. M. (2010). Ship-mounted acoustic Doppler current profilers. In *The GO-SHIP Repeat Hydrography Manual: A Collection of Expert Reports and Guidelines* (p. 11). International CLIVAR Project Office,. Retrieved from https://www.go-ship.org/Manual/Firing_SADCP.pdf

Fogaren, K. E., & Palevsky, H. I. (2024). *Bottle-calibrated dissolved oxygen (DO) profiles from US Overturning in the Subpolar North Atlantic Program (OSNAP) cruises in 2020 and 2022 (AR45 and AR69-03) [Dataset].* Biological and Chemical Oceanography Data Management Office (BCO-DMO). Retrieved 2024-08-02, from https://www.bco-dmo.org/dataset/933743

Foukal, N. P., & Pickart, R. S. (2023). Moored Observations of the West Greenland Coastal Current along the Southwest Greenland Shelf. *Journal of Physical Oceanography*, *53*(11), 2619–2632. Retrieved 2024-04-11, from https://journals.ametsoc.org/view/journals/phoc/53/11/JPO-D-23-0104.1.xml (Publisher: American Meteorological Society Section: Journal of Physical Oceanography) doi: 10.1175/JPO-D-23-0104.1

Fox, A. D., Handmann, P., Schmidt, C., Fraser, N., Rühs, S., Sanchez-Franks, A., ... Yashayaev, I. (2022, October). Exceptional freshening and cooling in the eastern subpolar North

Atlantic caused by reduced Labrador Sea surface heat loss. *Ocean Science*, *18*(5), 1507–1533. Retrieved 2023-03-10, from https://os.copernicus.org/articles/18/1507/2022/ doi: 10.5194/os-18-1507-2022

Frajka-Williams, E., Bamber, J. L., & Våge, K. (2016). Greenland Melt and the Atlantic Meridional Overturning Circulation. *Oceanography*, *29*(4), 22–33. Retrieved 2025-05-13, from https://tos.org/oceanography/article/greenland-melt-and-the-atlantic-meridional-overturning-circulation doi: https://doi.org/10.5670/oceanog.2016.96

Frajka-Williams, E., Rhines, P. B., & Eriksen, C. C. (2014, January). Horizontal Stratification during Deep Convection in the Labrador Sea. *Journal of Physical Oceanography*, *44*(1), 220–228. Retrieved 2022-12-14, from https://journals.ametsoc.org/view/journals/phoc/44/1/jpo-d-13-069.1.xml (Publisher: American Meteorological Society Section: Journal of Physical Oceanography) doi: 10.1175/JPO-D-13-069.1

Freeland, H. J., & Denman, K. L. (1982). A topographically controlled upwelling center off southern Vancouver Island. *Journal of Marine Research*(40), 1069–1093.

Fried, N. (2024). *Hidden below the surface: On the pathways, interaction and transport variability of the Irminger Current* (Doctoral thesis 2 (Research NOT UU / Graduation UU), Utrecht University). (ISBN: 9789062666997 Pages: E17433420241218) doi: 10.33540/2587

Fried, N., & Jong, M. F. d. (2022, March). The Role of the Irminger Current in the Irminger Sea Northward Transport Variability. *Journal of Geophysical Research: Oceans*, *127*(3), e2021JC018188. Retrieved 2023-01-27, from https://agupubs.onlinelibrary.wiley.com/doi/10.1029/2021JC018188 (Publisher: John Wiley & Sons, Ltd) doi: 10.1029/2021JC018188

Fröb, F., Olsen, A., Våge, K., Moore, G. W. K., Yashayaev, I., Jeansson, E., & Rajasakaren, B. (2016, October). Irminger Sea deep convection injects oxygen and anthropogenic carbon to the ocean interior. *Nature Communications*, *7*(1), 1–8. Retrieved 2020-07-15, from https://www.nature.com/articles/ncomms13244 doi: 10.1038/ncomms13244

Fu, Y., Lozier, M. S., Majumder, S., & Petit, T. (2024). Water Mass Transformation and Its Relationship With the Overturning Circulation in the Eastern Subpolar North Atlantic. *Journal of Geophysical Research: Oceans*, *129*(12), e2024JC021222. Retrieved 2024-12-19, from https://onlinelibrary.wiley.com/doi/abs/10.1029/2024JC021222 (_eprint: https://onlinelibrary.wiley.com/doi/pdf/10.1029/2024JC021222) doi: 10.1029/2024JC021222

Galbraith, P. S., & Kelley, D. E. (1996). Identifying Overturns in CTD Profiles. Retrieved 2024-09-10, from https://journals.ametsoc.org/view/journals/atot/13/3/1520-0426_1996_013_0688_ioicp_2_0_co_2.xml (Section: Journal of Atmospheric and Oceanic Technology)

GEBCO Compilation Group. (2020). *GEBCO 2020 Grid [Dataset].* doi: doi:10.5285/a29c5465-b138-234d-e053-6c86abc040b9

GEBCO Compilation Group. (2023). *GEBCO 2023 Grid [Dataset]* [Dataset]. Retrieved from https://www.gebco.net/data_and_products/gridded_bathymetry_data/ doi: 10.5285/f98b053b-0cbc-6c23-e053-6c86abc0af7b

Gelderloos, R., Katsman, C. A., & Drijfhout, S. S. (2011, November). Assessing the

Roles of Three Eddy Types in Restratifying the Labrador Sea after Deep Convection. *Journal of Physical Oceanography*, *41*(11), 2102–2119. Retrieved 2023-03-10, from http://journals.ametsoc.org/doi/10.1175/JPO-D-11-054.1 doi: 10.1175/JPO-D-11-054.1

GHRSST Science Team (2010). (2011). *The Recommended GHRSST Data Specification (GDS) 2.0* (Tech. Rep. No. document revision 4). Retrieved from https://archive.podaac.earthdata.nasa.gov/podaac-ops-cumulus-docs/ghrsst/open/docs/GDS20r5.pdf

Gordon, L., Jennings, J., Ross, A., & Krest, J. (1993). A Suggested Protocol for Continuous Flow Automated Analysis of Seawater Nutrients (Phosphate, Nitrate, Nitrite and Silicic Acid) in the WOCE Hydrographic Program and the Joint Global Ocean Fluxes Study. *Methods Manual WHPO*, *91-1*.

Gou, R., Feucher, C., Pennelly, C., & Myers, P. G. (2021). Seasonal Cycle of the Coastal West Greenland Current System Between Cape Farewell and Cape Desolation From a Very High-Resolution Numerical Model. *Journal of Geophysical Research: Oceans*, *126*(5), e2020JC017017. Retrieved 2023-05-03, from https://onlinelibrary.wiley.com/doi/abs/10.1029/2020JC017017 doi: 10.1029/2020JC017017

Gruber, N., Clement, D., Carter, B. R., Feely, R. A., van Heuven, S., Hoppema, M., ... Wanninkhof, R. (2019, March). The oceanic sink for anthropogenic CO2 from 1994 to 2007. *Science*, *363*(6432), 1193–1199. Retrieved 2020-07-21, from https://www.sciencemag.org/lookup/doi/10.1126/science.aau5153 doi: 10.1126/science.aau5153

Harris, P. T., & Whiteway, T. (2011, July). Global distribution of large submarine canyons: Geomorphic differences between active and passive continental margins. *Marine Geology*, *285*(1), 69–86. Retrieved 2024-08-20, from https://www.sciencedirect.com/science/article/pii/S0025322711001253 doi: 10.1016/j.margeo.2011.05.008

Hautala, S. L., Reid, J. L., & Bray, N. (1996). The distribution and mixing of Pacific water masses in the Indonesian Seas. *Journal of Geophysical Research: Oceans*, *101*(C5), 12375–12389. Retrieved 2024-06-24, from https://onlinelibrary.wiley.com/doi/abs/10.1029/96JC00037 (_eprint: https://onlinelibrary.wiley.com/doi/pdf/10.1029/96JC00037) doi: 10.1029/96JC00037

Hendry, K. R., Briggs, N., Henson, S., Opher, J., Brearley, J. A., Meredith, M. P., ... Meire, L. (2021). Tracing Glacial Meltwater From the Greenland Ice Sheet to the Ocean Using Gliders. *Journal of Geophysical Research: Oceans*, *126*(8), e2021JC017274. Retrieved 2025-02-19, from https://onlinelibrary.wiley.com/doi/abs/10.1029/2021JC017274 (_eprint: https://onlinelibrary.wiley.com/doi/pdf/10.1029/2021JC017274) doi: 10.1029/2021JC017274

Hendry, K. R., Huvenne, V. A. I., Robinson, L. F., Annett, A., Badger, M., Jacobel, A. W., ... Woodward, E. M. S. (2019). The biogeochemical impact of glacial meltwater from Southwest Greenland. *Progress in Oceanography*, *176*, 102126. Retrieved 2023-05-03, from https://www.sciencedirect.com/science/article/pii/S0079661118302817 doi: 10.1016/j.pocean.2019.102126

Hopwood, M. J., Carroll, D., Browning, T. J., Meire, L., Mortensen, J., Krisch, S., & Achterberg, E. P. (2018). Non-linear response of summertime marine productivity to increased meltwater discharge around Greenland. *Nature Communications*, *9*(1), 3256. Retrieved

2024-09-04, from https://www.nature.com/articles/s41467-018-05488-8 (Publisher: Nature Publishing Group) doi: 10.1038/s41467-018-05488-8

Howard, L. (1961). Note on a Paper of Miles, John W. *JOURNAL OF FLUID MECHANICS*, *10*(4), 509–512. Retrieved 2024-07-02, from https://www.webofscience.com/api/gateway?GWVersion=2&SrcAuth=DOISource&SrcApp=WOS&KeyAID=10.1017%2FS0022112061000317&DestApp=DOI&SrcAppSID=USW2EC0DD6qfRFs3WxDw8lfWLWE7H&SrcJTitle=JOURNAL+OF+FLUID+MECHANICS&DestDOIRegistrantName=Cambridge+University+Press (Num Pages: 4 Place: New York Publisher: Cambridge Univ Press Web of Science ID: WOS:A1961WT93200003) doi: 10.1017/S0022112061000317

Howard, S. L., Hyatt, J., & Padman, L. (2004). Mixing in the pycnocline over the western Antarctic Peninsula shelf during Southern Ocean GLOBEC. *Deep Sea Research Part II: Topical Studies in Oceanography*, *51*(17), 1965–1979. Retrieved 2025-02-18, from https://www.sciencedirect.com/science/article/pii/S0967064504001195 doi: 10.1016/j.dsr2.2004.08.002

Howard, S. L., & Padman, L. (2021). *Gr1kmTM: Greenland 1 kilometer Tide Model, 2021 [Software].* Retrieved 2024-09-03, from https://arcticdata.io/catalog/view/doi:10.18739/A2251FM3S (Publisher: urn:node:ARCTIC)

Josey, S. A., de Jong, M. F., Oltmanns, M., Moore, G. K., & Weller, R. A. (2019). Extreme Variability in Irminger Sea Winter Heat Loss Revealed by Ocean Observatories Initiative Mooring and the ERA5 Reanalysis. *Geophysical Research Letters*, *46*(1), 293–302. Retrieved from https://agupubs.onlinelibrary.wiley.com/doi/abs/10.1029/2018GL080956 (_eprint: https://agupubs.onlinelibrary.wiley.com/doi/pdf/10.1029/2018GL080956) doi: https://doi.org/10.1029/2018GL080956

JPL MUR MEaSUREs Project. (2015). *GHRSST Level 4 MUR Global Foundation Sea Surface Temperature Analysis.* CA, USA: PO.DAAC.

Katsman, C. A., Drijfhout, S. S., Dijkstra, H. A., & Spall, M. A. (2018). Sinking of Dense North Atlantic Waters in a Global Ocean Model: Location and Controls. *Journal of Geophysical Research: Oceans*, *123*(5), 3563–3576. Retrieved 2023-06-12, from https://onlinelibrary.wiley.com/doi/abs/10.1029/2017JC013329 (_eprint: https://onlinelibrary.wiley.com/doi/pdf/10.1029/2017JC013329) doi: 10.1029/2017JC013329

Katsman, C. A., Spall, M. A., & Pickart, R. S. (2004, September). Boundary Current Eddies and Their Role in the Restratification of the Labrador Sea. *Journal of Physical Oceanography*, *34*(9), 1967–1983. Retrieved 2023-03-01, from https://journals.ametsoc.org/view/journals/phoc/34/9/1520-0485_2004_034_1967_bceatr_2.0.co_2.xml (Publisher: American Meteorological Society Section: Journal of Physical Oceanography) doi: 10.1175/1520-0485(2004)034⟨1967:BCEATR⟩2.0.CO;2

Keil, P., Mauritsen, T., Jungclaus, J., Hedemann, C., Olonscheck, D., & Ghosh, R. (2020, July). Multiple drivers of the North Atlantic warming hole. *Nature Climate Change*, *10*(7), 667–671. Retrieved 2023-05-21, from https://www.nature.com/articles/s41558-020-0819-8 (Number: 7 Publisher: Nature Publishing Group) doi: 10.1038/

s41558-020-0819-8

Klinck, J. M. (1996). Circulation near submarine canyons: A modeling study. *Journal of Geophysical Research: Oceans*, *101*(C1), 1211–1223. Retrieved 2024-07-01, from https://onlinelibrary.wiley.com/doi/abs/10.1029/95JC02901 (_eprint: https://onlinelibrary.wiley.com/doi/pdf/10.1029/95JC02901) doi: 10.1029/95JC02901

Klinck, J. M. (1998). Heat and salt changes on the continental shelf west of the Antarctic Peninsula between January 1993 and January 1994. *Journal of Geophysical Research: Oceans*, *103*(C4), 7617–7636. Retrieved 2024-06-19, from https://onlinelibrary.wiley.com/doi/abs/10.1029/98JC00369 (_eprint: https://onlinelibrary.wiley.com/doi/pdf/10.1029/98JC00369) doi: 10.1029/98JC00369

Knutsen, , Svendsen, H., Østerhus, S., Rossby, T., & Hansen, B. (2005). Direct measurements of the mean flow and eddy kinetic energy structure of the upper ocean circulation in the NE Atlantic. *Geophysical Research Letters*, *32*(14). Retrieved 2025-05-09, from https://onlinelibrary.wiley.com/doi/abs/10.1029/2005GL023615 (_eprint: https://onlinelibrary.wiley.com/doi/pdf/10.1029/2005GL023615) doi: 10.1029/2005GL023615

Krawczyk, D. W., Kryk, A., Juggins, S., Burmeister, A., Pearce, C., Seidenkrantz, M. S., ... Witkowski, A. (2021). Spatio-temporal changes in ocean conditions and primary production in Baffin Bay and the Labrador Sea. *Palaeogeography, Palaeoclimatology, Palaeoecology*, *563*, 110175. Retrieved 2024-03-15, from https://www.sciencedirect.com/science/article/pii/S0031018220306234 doi: 10.1016/j.palaeo.2020.110175

Landschützer, P., Gruber, N., Bakker, D. C. E., & Schuster, U. (2014, September). Recent variability of the global ocean carbon sink. *Global Biogeochemical Cycles*, *28*(9), 927–949. Retrieved 2020-07-21, from http://doi.wiley.com/10.1002/2014GB004853 doi: 10.1002/2014GB004853

Le Bras, I. A.-A., Callies, J., Straneo, F., Biló, T. C., Holte, J., & Johnson, H. L. (2022). Slantwise Convection in the Irminger Sea. *Journal of Geophysical Research: Oceans*, *127*(10), e2022JC019071. Retrieved 2022-12-14, from https://onlinelibrary.wiley.com/doi/abs/10.1029/2022JC019071 doi: 10.1029/2022JC019071

Le Bras, I. A.-A., Straneo, F., Holte, J., de Jong, M. F., & Holliday, N. P. (2020). Rapid Export of Waters Formed by Convection Near the Irminger Sea's Western Boundary. *Geophysical Research Letters*, *47*(3), e2019GL085989. Retrieved 2023-03-27, from https://onlinelibrary.wiley.com/doi/abs/10.1029/2019GL085989 doi: 10.1029/2019GL085989

Le Bras, I. A.-A., Straneo, F., Holte, J., & Holliday, N. P. (2018). Seasonality of Freshwater in the East Greenland Current System From 2014 to 2016. *Journal of Geophysical Research: Oceans*, *123*(12), 8828–8848. Retrieved 2024-07-29, from https://onlinelibrary.wiley.com/doi/abs/10.1029/2018JC014511 (_eprint: https://onlinelibrary.wiley.com/doi/pdf/10.1029/2018JC014511) doi: 10.1029/2018JC014511

Lin, P., Pickart, R. S., Torres, D. J., & Pacini, A. (2018). Evolution of the Freshwater Coastal Current at the Southern Tip of Greenland. *Journal of Physical Oceanography*, *48*(9), 2127–2140. Retrieved 2023-05-03, from https://journals.ametsoc.org/view/journals/phoc/48/9/jpo-d-18-0035.1.xml (Publisher: American Meteorological

Society Section: Journal of Physical Oceanography) doi: 10.1175/JPO-D-18-0035.1

Lozier, M. S. (2010, June). Deconstructing the Conveyor Belt. *Science*, *328*(5985), 1507–1511. Retrieved 2025-05-13, from https://www.science.org/doi/10.1126/science.1189250 (Publisher: American Association for the Advancement of Science) doi: 10.1126/science.1189250

Lozier, M. S., Li, F., Bacon, S., Bahr, F., Bower, A. S., Cunningham, S. A., ... Zhao, J. (2019, February). A sea change in our view of overturning in the subpolar North Atlantic. *Science*, *363*(6426), 516–521. Retrieved 2020-07-16, from https://www.sciencemag.org/lookup/doi/10.1126/science.aau6592 doi: 10.1126/science.aau6592

Luo, H., Castelao, R. M., Rennermalm, A. K., Tedesco, M., Bracco, A., Yager, P. L., & Mote, T. L. (2016). Oceanic transport of surface meltwater from the southern Greenland ice sheet. *Nature Geoscience*, *9*(7), 528–532. Retrieved 2024-07-02, from https://www.nature.com/articles/ngeo2708 (Publisher: Nature Publishing Group) doi: 10.1038/ngeo2708

MacKinnon, J. A., Simmons, H. L., Hargrove, J., Thomson, J., Peacock, T., Alford, M. H., ... Wood, K. R. (2021). A warm jet in a cold ocean. *Nature Communications*, *12*(1), 2418. Retrieved 2024-11-19, from https://www.nature.com/articles/s41467-021-22505-5 (Publisher: Nature Publishing Group) doi: 10.1038/s41467-021-22505-5

Martinson, D. G., & McKee, D. C. (2012). Transport of warm Upper Circumpolar Deep Water onto the western Antarctic Peninsula continental shelf. *Ocean Science*, *8*(4), 433–442. Retrieved 2024-06-19, from https://os.copernicus.org/articles/8/433/2012/ (Publisher: Copernicus GmbH) doi: 10.5194/os-8-433-2012

Mecking, J. V., Drijfhout, S. S., Hirschi, J. J.-M., & Blaker, A. T. (2019, November). Ocean and atmosphere influence on the 2015 European heatwave. *Environmental Research Letters*, *14*(11), 114035. Retrieved 2025-05-21, from https://dx.doi.org/10.1088/1748-9326/ab4d33 (Publisher: IOP Publishing) doi: 10.1088/1748-9326/ab4d33

Meire, L., Søgaard, D. H., Mortensen, J., Meysman, F. J. R., Soetaert, K., Arendt, K. E., ... Rysgaard, S. (2015, April). Glacial meltwater and primary production are drivers of strong CO_2 uptake in fjord and coastal waters adjacent to the Greenland Ice Sheet. *Biogeosciences*, *12*(8), 2347–2363. Retrieved 2023-04-13, from https://bg.copernicus.org/articles/12/2347/2015/ (Publisher: Copernicus GmbH) doi: 10.5194/bg-12-2347-2015

Miles, J. W. (1961). On the stability of heterogeneous shear flows. *Journal of Fluid Mechanics*, *10*(4), 496–508. Retrieved 2024-07-02, from https://www.cambridge.org/core/journals/journal-of-fluid-mechanics/article/on-the-stability-of-heterogeneous-shear-flows/A9FC1F74697EB29B680F55D571E17218 doi: 10.1017/S0022112061000305

Moffat, C., & Meredith, M. (2018). Shelf–ocean exchange and hydrography west of the Antarctic Peninsula: a review. *Philosophical Transactions of the Royal Society A: Mathematical, Physical and Engineering Sciences*, *376*(2122), 20170164. Retrieved 2024-06-17, from https://royalsocietypublishing.org/doi/full/10.1098/rsta.2017.0164 (Publisher: Royal Society) doi: 10.1098/rsta.2017.0164

Moffat, C., Owens, B., & Beardsley, R. C. (2009). On the characteristics of Circumpolar Deep Water intrusions to the west Antarctic Peninsula Continental

Shelf. *Journal of Geophysical Research: Oceans*, *114*(C5). Retrieved 2024-06-18, from https://onlinelibrary.wiley.com/doi/abs/10.1029/2008JC004955 (_eprint: https://onlinelibrary.wiley.com/doi/pdf/10.1029/2008JC004955) doi: 10.1029/2008JC004955

Moore, G. W. K., & Renfrew, I. A. (2005, September). Tip Jets and Barrier Winds: A QuikSCAT Climatology of High Wind Speed Events around Greenland. Retrieved 2025-02-28, from https://journals.ametsoc.org/view/journals/clim/18/18/jcli3455.1.xml (Section: Journal of Climate) doi: 10.1175/JCLI3455.1

Morlighem, M., Williams, C. N., Rignot, E., An, L., Arndt, J. E., Bamber, J. L., ... Zinglersen, K. B. (2017). BedMachine v3: Complete Bed Topography and Ocean Bathymetry Mapping of Greenland From Multibeam Echo Sounding Combined With Mass Conservation. *Geophysical Research Letters*, *44*(21), 11,051–11,061. Retrieved 2024-02-02, from https://onlinelibrary.wiley.com/doi/abs/10.1002/2017GL074954 (_eprint: https://onlinelibrary.wiley.com/doi/pdf/10.1002/2017GL074954) doi: 10.1002/2017GL074954

Morrison, A. K., Hogg, A. A. M., England, M. H., & Spence, P. (2020). Warm Circumpolar Deep Water transport toward Antarctica driven by local dense water export in canyons. *Science Advances*, *6*(18), 9. Retrieved 2025-05-13, from https://www.science.org/doi/10.1126/sciadv.aav2516 doi: 10.1126/sciadv.aav2516

Mortensen, J., Rysgaard, S., Bendtsen, J., Lennert, K., Kanzow, T., Lund, H., & Meire, L. (2020). Subglacial Discharge and Its Down-Fjord Transformation in West Greenland Fjords With an Ice Mélange. *Journal of Geophysical Research: Oceans*, *125*(9), e2020JC016301. Retrieved 2024-11-21, from https://onlinelibrary.wiley.com/doi/abs/10.1029/2020JC016301 (_eprint: https://onlinelibrary.wiley.com/doi/pdf/10.1029/2020JC016301) doi: 10.1029/2020JC016301

Nash, J. D., Alford, M. H., Kunze, E., Martini, K., & Kelly, S. (2007). Hotspots of deep ocean mixing on the Oregon continental slope. *Geophysical Research Letters*, *34*(1). Retrieved 2024-11-19, from https://onlinelibrary.wiley.com/doi/abs/10.1029/2006GL028170 (_eprint: https://onlinelibrary.wiley.com/doi/pdf/10.1029/2006GL028170) doi: 10.1029/2006GL028170

NOAA National Geophysical Data Center. (2009). *ETOPO1 1 Arc-Minute Global Relief Model [Dataset]*. NOAA National Centers for Environmental Information. Retrieved 2025-02-28, from https://www.ncei.noaa.gov/access/metadata/landing-page/bin/iso?id=gov.noaa.ngdc.mgg.dem:316 (Last Modified: 2020-05-21-06:00)

Nørgaard-Pedersen, N., & Mikkelsen, N. (2009). 8000 year marine record of climate variability and fjord dynamics from Southern Greenland. *Marine Geology*, *264*(3), 177–189. Retrieved 2024-11-21, from https://www.sciencedirect.com/science/article/pii/S0025322709001364 doi: 10.1016/j.margeo.2009.05.004

Olsen, A., Brown, K. R., Chierici, M., Johannessen, T., & Neill, C. (2008, April). Sea-surface CO2 fugacity in the subpolar North Atlantic. *Biogeosciences*, *5*(2), 535–547. Retrieved 2021-02-16, from https://bg.copernicus.org/articles/5/535/2008/ (Publisher: Copernicus GmbH) doi: https://doi.org/10.5194/bg-5-535-2008

Osborn, T. R. (1978). Measurements of energy dissipation adjacent to an island. *Journal of Geophysical Research: Oceans*, *83*(C6), 2939–2957. Retrieved 2024-11-19,

from https://onlinelibrary.wiley.com/doi/abs/10.1029/JC083iC06p02939 (_eprint: https://onlinelibrary.wiley.com/doi/pdf/10.1029/JC083iC06p02939) doi: 10.1029/JC083iC06p02939

Osborn, T. R. (1980). Estimates of the Local Rate of Vertical Diffusion from Dissipation Measurements. Retrieved 2024-10-03, from https://journals.ametsoc.org/view/journals/phoc/10/1/1520-0485_1980_010_0083_eotlro_2_0_co_2.xml (Section: Journal of Physical Oceanography)

Ozmidov, R. V. (1965). On the turbulent exchange in a stably stratified ocean. *Atmos. Oceanic Phys.*, *8*, 853–860. Retrieved 2024-10-01, from https://search-library.ucsd.edu

Pacini, A., Pickart, R. S., Bahr, F., Torres, D. J., Ramsey, A. L., Holte, J., ... Jong, M. F. d. (2020). Mean Conditions and Seasonality of the West Greenland Boundary Current System near Cape Farewell. *Journal of Physical Oceanography*, *50*(10), 2849–2871. Retrieved 2023-05-02, from https://journals.ametsoc.org/view/journals/phoc/50/10/jpoD200086.xml (Publisher: American Meteorological Society Section: Journal of Physical Oceanography) doi: 10.1175/JPO-D-20-0086.1

Pacini, A., Pickart, R. S., Bras, I. A. L., Straneo, F., Holliday, N. P., & Spall, M. A. (2021, July). Cyclonic Eddies in the West Greenland Boundary Current System. *Journal of Physical Oceanography*, *51*(7), 2087–2102. Retrieved 2023-05-11, from https://journals.ametsoc.org/view/journals/phoc/51/7/JPO-D-20-0255.1.xml (Publisher: American Meteorological Society Section: Journal of Physical Oceanography) doi: 10.1175/JPO-D-20-0255.1

Palevsky, H., & Nicholson, D. (2018, March). The North Atlantic Biological Pump: Insights from the Ocean Observatories Initiative Irminger Sea Array. *Oceanography*, *31*(1), 42–49. Retrieved 2020-07-21, from https://tos.org/oceanography/article/the-north-atlantic-biological-pump-insights-from-the-ocean-observatories-in doi: 10.5670/oceanog.2018.108

Palevsky, H., Yoder, M. F., Nicholson, D., & Fogaren, K. E. (2024). *Discrete sample measurements of dissolved oxygen, dissolved inorganic carbon, and total alkalinity from US Overturning in the Subpolar North Atlantic Program (OSNAP) cruises in 2020 and 2022 (AR45 and AR69-03) [Dataset].* Biological and Chemical Oceanography Data Management Office (BCO-DMO). Retrieved 2024-08-02, from https://www.bco-dmo.org/dataset/934025

Pedlosky, J. (1979). *Geophysical Fluid Dynamics* (2nd ed.). Springer-Verlag.

Petit, T., Lozier, M. S., Josey, S. A., & Cunningham, S. A. (2020, November). Atlantic Deep Water Formation Occurs Primarily in the Iceland Basin and Irminger Sea by Local Buoyancy Forcing. *Geophysical Research Letters*, *47*(22). Retrieved 2023-01-24, from https://onlinelibrary.wiley.com/doi/10.1029/2020GL091028 doi: 10.1029/2020GL091028

Petit, T., Mercier, H., & Thierry, V. (2019). New Insight Into the Formation and Evolution of the East Reykjanes Ridge Current and Irminger Current. *Journal of Geophysical Research: Oceans*, *124*(12), 9171–9189. Retrieved 2023-06-13, from https://onlinelibrary.wiley.com/doi/abs/10.1029/2019JC015546 (_eprint: https://onlinelibrary.wiley.com/doi/pdf/10.1029/2019JC015546) doi: 10.1029/2019JC015546

Pickart, R. S., Spall, M. A., Ribergaard, M. H., Moore, G. W. K., & Milliff, R. F. (2003, July). Deep convection in the Irminger Sea forced by the Greenland tip jet. *Nature*, *424*(6945), 152–156. doi: 10.1038/nature01729

Pérez, F. F., Mercier, H., Vázquez-Rodríguez, M., Lherminier, P., Velo, A., Pardo, P. C., ... Ríos, A. F. (2013, February). Atlantic Ocean CO2 uptake reduced by weakening of the meridional overturning circulation. *Nature Geoscience*, *6*(2), 146–152. Retrieved 2023-04-04, from https://www.nature.com/articles/ngeo1680 (Number: 2 Publisher: Nature Publishing Group) doi: 10.1038/ngeo1680

Rahmstorf, S., Box, J. E., Feulner, G., Mann, M. E., Robinson, A., Rutherford, S., & Schaffernicht, E. J. (2015). Exceptional twentieth-century slowdown in Atlantic Ocean overturning circulation. *Nature Climate Change*, *5*(5), 475–480. Retrieved 2024-06-19, from https://www.nature.com/articles/nclimate2554 (Publisher: Nature Publishing Group) doi: 10.1038/nclimate2554

Rhein, M., Steinfeldt, R., Kieke, D., Stendardo, I., & Yashayaev, I. (2017, August). Ventilation variability of Labrador Sea Water and its impact on oxygen and anthropogenic carbon: a review. *Philosophical Transactions of the Royal Society A: Mathematical, Physical and Engineering Sciences*, *375*(2102), 20160321. Retrieved 2023-04-04, from https://royalsocietypublishing.org/doi/full/10.1098/rsta.2016.0321 (Publisher: Royal Society) doi: 10.1098/rsta.2016.0321

Ribergaard, M. H. (2007). *Oceanographic Investigations off West Greenland 2006* (Tech. Rep. No. N5339). Northwest Atlantic Fisheries Organization. Retrieved 2024-11-21, from https://www.nafo.int/Portals/0/PDFs/sc/2007/scr07-001.pdf

Roemmich, D., & Gilson, J. (2009, August). The 2004–2008 mean and annual cycle of temperature, salinity, and steric height in the global ocean from the Argo Program. *Progress in Oceanography*, *82*(2), 81–100. Retrieved 2022-12-14, from https://www.sciencedirect.com/science/article/pii/S0079661109000160 doi: 10.1016/j.pocean.2009.03.004

Rossby, T., Reverdin, G., Chafik, L., & Søiland, H. (2017). A direct estimate of poleward volume, heat, and freshwater fluxes at 59.5°N between Greenland and Scotland. *Journal of Geophysical Research: Oceans*, *122*(7), 5870–5887. Retrieved 2025-04-03, from https://onlinelibrary.wiley.com/doi/abs/10.1002/2017JC012835 (_eprint: https://onlinelibrary.wiley.com/doi/pdf/10.1002/2017JC012835) doi: 10.1002/2017JC012835

Ryan, S., Hattermann, T., Darelius, E., & Schröder, M. (2017). Seasonal cycle of hydrography on the eastern shelf of the Filchner Trough, Weddell Sea, Antarctica. *Journal of Geophysical Research: Oceans*, *122*(8), 6437–6453. Retrieved 2025-05-20, from https://onlinelibrary.wiley.com/doi/abs/10.1002/2017JC012916 (_eprint: https://onlinelibrary.wiley.com/doi/pdf/10.1002/2017JC012916) doi: 10.1002/2017JC012916

Rysgaard, S., Mortensen, J., Juul-Pedersen, T., Sørensen, L. L., Lennert, K., Søgaard, D. H., ... Bendtsen, J. (2012, January). High air–sea CO2 uptake rates in nearshore and shelf areas of Southern Greenland: Temporal and spatial variability. *Marine Chemistry*, *128-129*, 26–33. Retrieved 2021-04-16, from https://www.sciencedirect.com/science/article/pii/S0304420311001277 doi: 10.1016/j.marchem.2011.11.002

Sabine, C. L. (2004). The Oceanic Sink for Anthropogenic CO2. *Science*, *305*(5682), 367–371. Retrieved 2020-07-16, from https://www.sciencemag.org/lookup/doi/10.1126/science.1097403 doi: 10.1126/science.1097403

Schiller-Weiss, I., Martin, T., & Schwarzkopf, F. U. (2024). Emerging Influence of Enhanced Greenland Melting on Boundary Currents and Deep Convection Regimes in the Labrador and Irminger Seas. *Geophysical Research Letters*, *51*(9), e2024GL109022. Retrieved 2024-05-14, from https://onlinelibrary.wiley.com/doi/abs/10.1029/2024GL109022 (_eprint: https://onlinelibrary.wiley.com/doi/pdf/10.1029/2024GL109022) doi: 10.1029/2024GL109022

Scott, R. M., Brearley, J. A., Naveira Garabato, A. C., Venables, H. J., & Meredith, M. P. (2021). Rates and Mechanisms of Turbulent Mixing in a Coastal Embayment of the West Antarctic Peninsula. *Journal of Geophysical Research: Oceans*, *126*(5), e2020JC016861. Retrieved 2025-05-14, from https://onlinelibrary.wiley.com/doi/abs/10.1029/2020JC016861 (_eprint: https://onlinelibrary.wiley.com/doi/pdf/10.1029/2020JC016861) doi: 10.1029/2020JC016861

Shepard, F. P. (1981). Submarine Canyons: Multiple Causes and Long-Time Persistence. *AAPG Bulletin*, *65*(6), 1062–1077. Retrieved 2024-08-20, from https://archives.datapages.com/data/bulletns/1980-81/data/pg/0065/0006/1050/1062.htm (Publisher: American Association of Petroleum Geologists)

Silvano, A., Holland, P. R., Naughten, K. A., Dragomir, O., Dutrieux, P., Jenkins, A., ... Naveira Garabato, A. C. (2022). Baroclinic Ocean Response to Climate Forcing Regulates Decadal Variability of Ice-Shelf Melting in the Amundsen Sea. *Geophysical Research Letters*, *49*(24), e2022GL100646. Retrieved 2024-04-22, from https://onlinelibrary.wiley.com/doi/abs/10.1029/2022GL100646 (_eprint: https://onlinelibrary.wiley.com/doi/pdf/10.1029/2022GL100646) doi: 10.1029/2022GL100646

Slater, D. A., Felikson, D., Straneo, F., Goelzer, H., Little, C. M., Morlighem, M., ... Nowicki, S. (2020, March). Twenty-first century ocean forcing of the Greenland ice sheet for modelling of sea level contribution. *The Cryosphere*, *14*(3), 985–1008. Retrieved 2025-05-19, from https://tc.copernicus.org/articles/14/985/2020/ (Publisher: Copernicus GmbH) doi: 10.5194/tc-14-985-2020

Slater, D. A., & Straneo, F. (2022). Submarine melting of glaciers in Greenland amplified by atmospheric warming. *Nature Geoscience*, *15*(10), 794–799. Retrieved 2024-04-26, from https://www.nature.com/articles/s41561-022-01035-9 (Publisher: Nature Publishing Group) doi: 10.1038/s41561-022-01035-9

Snow, T., Straneo, F., Holte, J., Grigsby, S., Abdalati, W., & Scambos, T. (2021). More than Skin Deep: Sea Surface Temperature as a Means of Inferring Atlantic Water Variability on the Southeast Greenland Continental Shelf Near Helheim Glacier. *Journal of Geophysical Research: Oceans*, *126*(4), e2020JC016509. Retrieved 2023-05-26, from https://onlinelibrary.wiley.com/doi/abs/10.1029/2020JC016509 doi: 10.1029/2020JC016509

Snow, T., Zhang, W., Schreiber, E., Siegfried, M., Abdalati, W., & Scambos, T. (2023). Alongshore Winds Force Warm Atlantic Water Toward Helheim Glacier in Southeast Greenland. *Journal of Geophysical Research: Oceans*, *128*(9), e2023JC019953. Re-

trieved 2024-06-15, from https://onlinelibrary.wiley.com/doi/abs/10.1029/2023JC019953 (_eprint: https://onlinelibrary.wiley.com/doi/pdf/10.1029/2023JC019953) doi: 10.1029/2023JC019953

Spall, M. A. (2004, May). Boundary Currents and Watermass Transformation in Marginal Seas. *Journal of Physical Oceanography*, *34*(5), 1197–1213. Retrieved 2022-12-14, from https://journals.ametsoc.org/view/journals/phoc/34/5/1520-0485_2004_034_1197_bcawti_2.0.co_2.xml (Publisher: American Meteorological Society Section: Journal of Physical Oceanography) doi: 10.1175/1520-0485(2004)034⟨1197:BCAWTI⟩2.0.CO;2

Spurgin, J. M., & Allen, S. E. (2014). Flow dynamics around downwelling submarine canyons. *Ocean Science*, *10*(5), 799–819. Retrieved 2024-10-17, from https://os.copernicus.org/articles/10/799/2014/ (Publisher: Copernicus GmbH) doi: 10.5194/os-10-799-2014

Sterl, M. F., & de Jong, M. F. (2022, December). Restratification Structure and Processes in the Irminger Sea. *Journal of Geophysical Research: Oceans*, *127*(12). Retrieved 2023-03-10, from https://onlinelibrary.wiley.com/doi/10.1029/2022JC019126 doi: 10.1029/2022JC019126

St-Laurent, P., Klinck, J. M., & Dinniman, M. S. (2013). On the Role of Coastal Troughs in the Circulation of Warm Circumpolar Deep Water on Antarctic Shelves. Retrieved 2024-06-19, from https://journals.ametsoc.org/view/journals/phoc/43/1/jpo-d-11-0237.1.xml (Section: Journal of Physical Oceanography) doi: 10.1175/JPO-D-11-0237.1

Straneo, F. (2006a, April). Heat and Freshwater Transport through the Central Labrador Sea. *Journal of Physical Oceanography*, *36*(4), 606–628. Retrieved 2021-04-29, from https://journals.ametsoc.org/view/journals/phoc/36/4/jpo2875.1.xml (Publisher: American Meteorological Society Section: Journal of Physical Oceanography) doi: 10.1175/JPO2875.1

Straneo, F. (2006b, September). On the Connection between Dense Water Formation, Overturning, and Poleward Heat Transport in a Convective Basin*. *Journal of Physical Oceanography*, *36*(9), 1822–1840. Retrieved 2020-10-15, from https://journals.ametsoc.org/jpo/article/36/9/1822/10606/On-the-Connection-between-Dense-Water-Formation doi: 10.1175/JPO2932.1

Straneo, F. (2022). *ADCP (Hawaii UHDAS) data as collected during the cruise AR69-03, Collaborative Research: Overturning in the Subpolar North Atlantic Program [Dataset]*. Rolling Deck to Repository (R2R). Retrieved 2024-10-09, from https://www.rvdata.us/search/fileset/153091 doi: https://doi.org/10.7284/153091

Straneo, F. (2023). *OSNAP 2022 Hydrographic Cruise: 33VB20220819 [Dataset]*. CCHDO: CLIVAR and Carbon Hydrographic Data Office. Retrieved 2024-12-12, from https://cchdo.ucsd.edu/cruise/33VB20220819 doi: 10.7942/C24H21

Straneo, F., & Heimbach, P. (2013). North Atlantic warming and the retreat of Greenland's outlet glaciers. *Nature*, *504*(7478), 36–43. Retrieved 2023-04-12, from https://www.nature.com/articles/nature12854 (Number: 7478 Publisher: Nature Publishing Group) doi: 10.1038/nature12854

Sutherland, D. A., & Cenedese, C. (2009). Laboratory Experiments on the Interaction of a Buoy-

ant Coastal Current with a Canyon: Application to the East Greenland Current. *Journal of Physical Oceanography*, *39*(5), 1258–1271. Retrieved 2023-05-11, from https://journals.ametsoc.org/view/journals/phoc/39/5/2008jpo4028.1.xml doi: 10.1175/2008JPO4028.1

Sutherland, D. A., Straneo, F., Stenson, G. B., Davidson, F. J., Hammill, M. O., & Rosing-Asvid, A. (2013). Atlantic water variability on the SE Greenland continental shelf and its relationship to SST and bathymetry. *Journal of Geophysical Research: Oceans*, *118*(2), 847–855. Retrieved 2024-06-19, from https://onlinelibrary.wiley.com/doi/abs/10.1029/2012JC008354 (_eprint: https://onlinelibrary.wiley.com/doi/pdf/10.1029/2012JC008354) doi: 10.1029/2012JC008354

Swingedouw, D., Houssais, M.-N., Herbaut, C., Blaizot, A.-C., Devilliers, M., & Deshayes, J. (2022). AMOC Recent and Future Trends: A Crucial Role for Oceanic Resolution and Greenland Melting? *Frontiers in Climate*, *4*. Retrieved 2024-06-19, from https://www.frontiersin.org/articles/10.3389/fclim.2022.838310 (Publisher: Frontiers) doi: 10.3389/fclim.2022.838310

Takahashi, T., Sutherland, S. C., Chipman, D. W., Goddard, J. G., Ho, C., Newberger, T., ... Munro, D. R. (2014, August). Climatological distributions of pH, pCO2, total CO2, alkalinity, and CaCO3 saturation in the global surface ocean, and temporal changes at selected locations. *Marine Chemistry*, *164*, 95–125. Retrieved 2020-12-15, from http://www.sciencedirect.com/science/article/pii/S0304420314001042 doi: 10.1016/j.marchem.2014.06.004

Takahashi, T., Sutherland, S. C., Wanninkhof, R., Sweeney, C., Feely, R. A., Chipman, D. W., ... de Baar, H. J. W. (2009, April). Climatological mean and decadal change in surface ocean pCO2, and net sea–air CO2 flux over the global oceans. *Deep Sea Research Part II: Topical Studies in Oceanography*, *56*(8), 554–577. Retrieved 2023-04-04, from https://www.sciencedirect.com/science/article/pii/S0967064508004311 doi: 10.1016/j.dsr2.2008.12.009

Tesdal, J.-E., Ducklow, H. W., Goes, J. I., & Yashayaev, I. (2022, August). Recent nutrient enrichment and high biological productivity in the Labrador Sea is tied to enhanced winter convection. *Progress in Oceanography*, *206*, 102848. Retrieved 2023-05-21, from https://www.sciencedirect.com/science/article/pii/S0079661122001069 doi: 10.1016/j.pocean.2022.102848

Thorpe, S. A. (1997). Turbulence and mixing in a Scottish Loch. *Philosophical Transactions of the Royal Society of London. Series A, Mathematical and Physical Sciences*, *286*(1334), 125–181. Retrieved 2024-09-30, from https://royalsocietypublishing.org/doi/10.1098/rsta.1977.0112 (Publisher: Royal Society) doi: 10.1098/rsta.1977.0112

Tjiputra, J. F., Goris, N., Lauvset, S. K., Heinze, C., Olsen, A., Schwinger, J., & Steinfeldt, R. (2018). Mechanisms and Early Detections of Multidecadal Oxygen Changes in the Interior Subpolar North Atlantic. *Geophysical Research Letters*, *45*(9), 4218–4229. Retrieved 2023-04-04, from https://onlinelibrary.wiley.com/doi/abs/10.1029/2018GL077096 (_eprint: https://onlinelibrary.wiley.com/doi/pdf/10.1029/2018GL077096) doi: 10.1029/2018GL077096

Trenberth, K. E., & Caron, J. M. (2001, August). Estimates of Meridional Atmosphere and Ocean

Heat Transports. Retrieved 2025-05-21, from https://journals.ametsoc.org/view/journals/clim/14/16/1520-0442_2001_014_3433_eomaao_2.0.co_2.xml (Section: Journal of Climate)

Uchida, H., Johnson, G. C., & McTaggart, K. E. (2010). CTD Oxygen Sensor Calibration Procedures. Retrieved 2024-08-02, from https://repository.oceanbestpractices.org/handle/11329/374 (Accepted: 2017-11-24T12:04:56Z) doi: 10.25607/OBP-1344

van Aken, H. M., de Jong, M. F., & Yashayaev, I. (2011, May). Decadal and multi-decadal variability of Labrador Sea Water in the north-western North Atlantic Ocean derived from tracer distributions: Heat budget, ventilation, and advection. *Deep Sea Research Part I: Oceanographic Research Papers*, *58*(5), 505–523. Retrieved 2023-06-23, from https://www.sciencedirect.com/science/article/pii/S0967063711000525 doi: 10.1016/j.dsr.2011.02.008

Vaughan, D., Comiso, J., Allison, I., Carrasco, J., Kaser, G., Kwok, R., ... Zhang, T. (2013). Observations: Cryosphere. In *Climate Change 2013: The Physical Science Basis. Contribution of Working Group I to the Fifth Assessment Report of the Intergovernmental Panel on Climate Change* (p. 66). Cambridge, United Kingdom and New York, NY, USA: Cambridge University Press. Retrieved 2025-05-21, from https://www.ipcc.ch/site/assets/uploads/2018/02/WG1AR5_Chapter04_FINAL.pdf

Venables, H. J., Meredith, M. P., & Brearley, J. A. (2017, May). Modification of deep waters in Marguerite Bay, western Antarctic Peninsula, caused by topographic overflows. *Deep Sea Research Part II: Topical Studies in Oceanography*, *139*, 9–17. Retrieved 2025-05-12, from https://www.sciencedirect.com/science/article/pii/S0967064516302843 doi: 10.1016/j.dsr2.2016.09.005

Vernet, M., Ellingsen, I., Marchese, C., Bélanger, S., Cape, M., Slagstad, D., & Matrai, P. A. (2021). Spatial variability in rates of net primary production (NPP) and onset of the spring bloom in Greenland shelf waters. *Progress in Oceanography*, *198*, 102655. Retrieved 2023-05-11, from https://www.sciencedirect.com/science/article/pii/S0079661121001403 doi: 10.1016/j.pocean.2021.102655

Visbeck, M., Marshall, J., & Jones, H. (1996, September). Dynamics of Isolated Convective Regions in the Ocean. *Journal of Physical Oceanography*, *26*(9), 1721–1734. Retrieved 2023-04-21, from https://journals.ametsoc.org/view/journals/phoc/26/9/1520-0485_1996_026_1721_doicri_2_0_co_2.xml (Publisher: American Meteorological Society Section: Journal of Physical Oceanography) doi: 10.1175/1520-0485(1996)026⟨1721:DOICRI⟩2.0.CO;2

Voet, G., Girton, J. B., Alford, M. H., Carter, G. S., Klymak, J. M., & Mickett, J. B. (2015). Pathways, Volume Transport, and Mixing of Abyssal Water in the Samoan Passage. Retrieved 2024-06-24, from https://journals.ametsoc.org/view/journals/phoc/45/2/jpo-d-14-0096.1.xml (Section: Journal of Physical Oceanography) doi: 10.1175/JPO-D-14-0096.1

Volkov, D. L. (2005, April). Interannual Variability of the Altimetry-Derived Eddy Field and Surface Circulation in the Extratropical North Atlantic Ocean in 1993–2001. *Journal of Physical Oceanography*, *35*(4), 405–426. Retrieved 2023-01-20, from https://journals.ametsoc.org/view/journals/phoc/35/4/jpo2683.1.xml (Publisher:

American Meteorological Society Section: Journal of Physical Oceanography) doi: 10.1175/JPO2683.1

Våge, K., Pickart, R. S., Sarafanov, A., Knutsen, , Mercier, H., Lherminier, P., ... Bacon, S. (2011, May). The Irminger Gyre: Circulation, convection, and interannual variability. *Deep Sea Research Part I: Oceanographic Research Papers*, *58*(5), 590–614. Retrieved 2020-07-21, from https://linkinghub.elsevier.com/retrieve/pii/S0967063711000562 doi: 10.1016/j.dsr.2011.03.001

Wood, M., Rignot, E., Fenty, I., An, L., Bjørk, A., van den Broeke, M., ... Zhang, H. (2021). Ocean forcing drives glacier retreat in Greenland. *Science Advances*, *7*(1), eaba7282. Retrieved 2024-06-19, from https://www.science.org/doi/10.1126/sciadv.aba7282 (Publisher: American Association for the Advancement of Science) doi: 10.1126/sciadv.aba7282

Wunsch, C. (1996). *The Ocean Circulation Inverse Problem*. Cambridge: Cambridge University Press. Retrieved 2023-03-10, from https://www.cambridge.org/core/books/ocean-circulation-inverse-problem/9CCD014E92B741C8FE3E295CB0F93B19 doi: 10.1017/CBO9780511629570

Yin, J., & Zhao, M. (2021, October). Influence of the Atlantic meridional overturning circulation on the U.S. extreme cold weather. *Communications Earth & Environment*, *2*(1), 1–10. Retrieved 2025-05-21, from https://www.nature.com/articles/s43247-021-00290-9 (Publisher: Nature Publishing Group) doi: 10.1038/s43247-021-00290-9

Zhang, W., & Lentz, S. J. (2017, December). Wind-Driven Circulation in a Shelf Valley. Part I: Mechanism of the Asymmetrical Response to Along-Shelf Winds in Opposite Directions. Retrieved 2025-03-28, from https://journals.ametsoc.org/view/journals/phoc/47/12/jpo-d-17-0083.1.xml (Section: Journal of Physical Oceanography) doi: 10.1175/JPO-D-17-0083.1

Zunino, P., Mercier, H., & Thierry, V. (2020, January). Why did deep convection persist over four consecutive winters (2015–2018) southeast of Cape Farewell? *Ocean Science*, *16*(1), 99–113. Retrieved 2023-04-05, from https://os.copernicus.org/articles/16/99/2020/ (Publisher: Copernicus GmbH) doi: 10.5194/os-16-99-2020